Master of Science Thesis
European Wind Energy Master - Rotor Design Track - Aerodynamics

Airfoil Design for Vertical Axis Wind Turbines

Including Correct Simulation of Flow Curvature

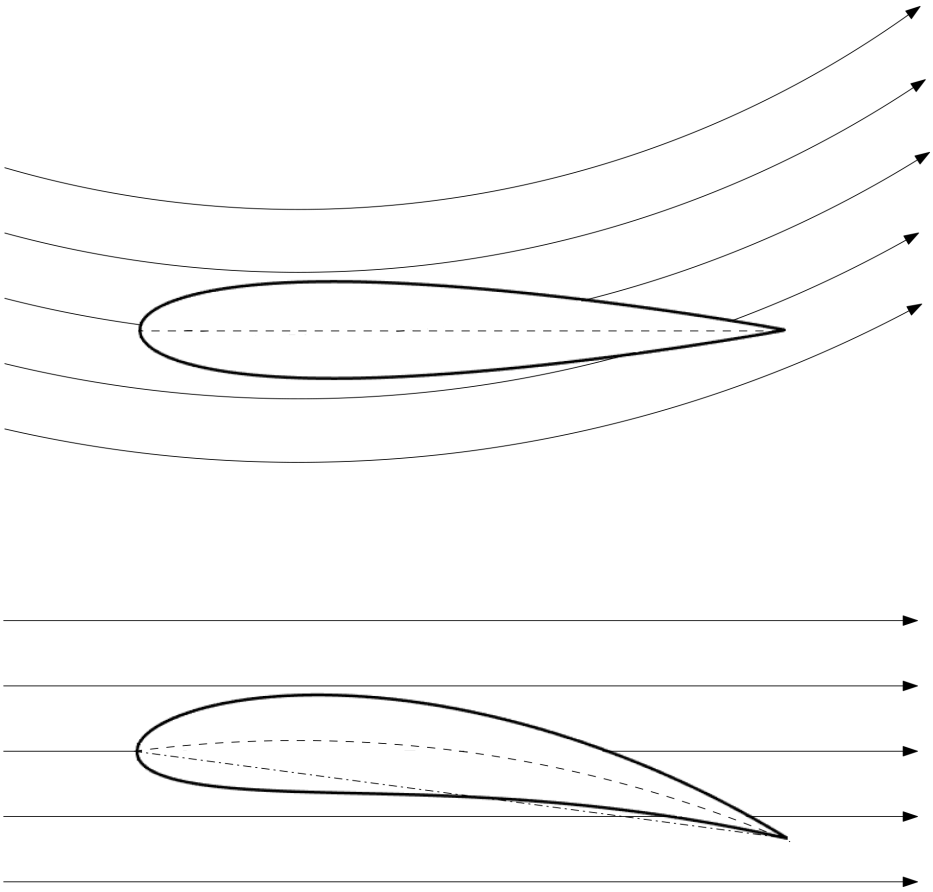

Sander van der Horst

October 21, 2015

The figure on the title page depicts a virtual airfoil transformation due to flow curvature. A NACA0015 airfoil in orbit of a VAWT with a very high chord-to-radius ratio of 0.5, mounted at its quarter chord position, encounters these curvilinear streamlines. For analysis purposes, an approximation in straight flow is obtained by a virtual airfoil transformation, resulting in added camber and angle of attack.

Airfoil Design for Vertical Axis Wind Turbines

Including Correct Simulation of Flow Curvature

Master of Science Thesis

For obtaining the degree of Master of Science in
Aerospace Engineering at Delft University of Technology and in
Engineering Wind Energy at Technical University of Denmark.

Sander van der Horst

October 21, 2015

European Wind Energy Master
DUWIND - Delft University of Technology
DTU Wind Energy - Technical University of Denmark

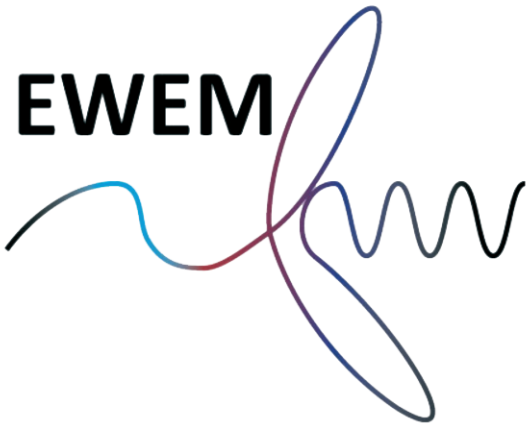
EWEM


TU Delft


DTU


European Commission
ERASMUS
MUNDUS

The undersigned hereby certify that they have read and recommend to the Delft University of Technology, Department of Wind Energy and Technical University of Denmark, Department of Wind Energy for acceptance a thesis entitled **"Airfoil Design for Vertical Axis Wind Turbines Including Correct Simulation of Flow Curvature"** by **Sander van der Horst** in partial fulfillment of the requirements for the degree of **Master of Science**.

Dated: October 21, 2015

Supervisor: _____
Dr.ir. C.J. Simão Ferreira of Delft University of Technology

Supervisor: _____
N. Ramos-García of Technical University of Denmark

Reader: _____
Ir. M.B. Zaaijer of Delft University of Technology

Reader: _____
J. Johansen of Endurance Wind Power

Reader: _____
Prof. J.N. Sørensen of Technical University of Denmark

Acknowledgements

First and foremost, I would like to express my gratitude to my supervisors, Carlos and Nestor. Without their help I would probably still be stuck calculating the wrong pressure distribution. Carlos, thank you for your patience and understanding, I can imagine it must have been challenging at times for you as well. And Nestor, thanks so much for assisting me while not even being in the same country. The Vidyo-calls were always helpful.

Also, I want to thank Jelmer with helping to implement the flow curvature models and analyse their results. Hopefully we can get our paper published!

Finally, I would like to thank Rody, for his explanation of and guidance through the complicated software called Optiflow.

Delft, The Netherlands
October 21, 2015

Sander van der Horst

Summary

In the past, the vertical axis wind turbine (VAWT) lost the competition to its horizontal axis counterpart, having (wrongfully) presumed disadvantages like increased fatigue and low efficiency. Little research and development into the VAWT led to a large gap between the maturity of technology of both turbine types. Now that due to modern techniques the VAWT experiences renewed interest, topics like airfoil design are reinvestigated.

One phenomenon particularly, plays an important role in VAWT aerodynamics: flow curvature. Due to the VAWT airfoil's rotation about an offset centre, there exists a chordwise angle of attack variation. Also, the added rotational velocities will alter the pressure distribution and boundary layer of the airfoil, leading to a change in force distribution and turbine efficiency.

This research sets out to chart these flow curvature effects and implement suggested models to cope with them. Furthermore, using a pitching airfoil model, an implementation in the airfoil analysis code XFOIL will provide the possibility to investigate inviscid and viscous flow curvature effects. What effect these have on airfoil design shall be found using an airfoil optimiser, generating optimal airfoils for various levels of flow curvature.

This thesis has applied six models authors suggested to investigate flow curvature. By applying transformations to virtual airfoils, leading to added camber and incidence angle, the researchers thought to mimic rotating VAWT airfoils in straight flow. Comparison with each other and a solution of a verified panel method showed that their approximation is reasonable within bounds. When the pitch rate and location is kept to practical values, also the difference between the methods is very little. Therefore the methods can be used interchangeably.

A pitching model has been devised, showing that the chord-to-radius ratio an be simulated by the pitch rate of a pitching airfoil. As the chord-to-radius ratio determines the amount of variation of angle of attack over the chord due to flow curvature, this model can be used to investigate flow curvature effects. The model has been applied in XFOIL and the results show a good comparison to the benchmark panel code. There still exists a discrepancy between the solutions, inherent to the difference calculation methods and dependent on the pitch location. The latter determines the arm to the surface and therefore the magnitude of rotational velocity, which increases the error with respect to the benchmark. Cambered airfoils and airfoils at a larger pitch setting showed less susceptibility to flow curvature.

The modified version of XFOIL is used in an optimisation campaign to investigate the impact of increasing chord-to-radius ratio. The method proved to be slightly unstable and therefore little data is obtained. Of the dataset the following trends can be obtained, using the least-squares method. With increasing chord-to-radius ratio, the camber tends to become more negative and shift forward. This is the optimiser trying to maintain optimal power, by choosing airfoils which will stall later to avoid power loss. Also, this results in thinner profiles with their maximum thickness more aft.

Finally, the optimal airfoils have been applied in a two-dimensional VAWT analysis model. This showed that there is very little power gain, and possible power loss when applying the pitch optimised airfoils.

Contents

Page

Page

List of Figures

Figure **Page**

Figure **Page**

Figure **Page**

List of Tables

Table **Page**

List of Algorithms

Nomenclature

Latin Symbols

Symbol	Description	Units
a	Streamfunction coefficient matrix	$[-]$
A	Bernstein coefficient	$[-]$
b	Streamfunction coefficient matrix	$[-]$
c	Chord	$[m]$
$\frac{c}{R}$	Chord-to-radius ratio	$[-]$
C	Class function	$[-]$
C_d	Drag coefficient	$[-]$
C_l	Lift coefficient	$[-]$
C_{l_α}	Lift slope	$[-]$
C_p	Pressure coefficient	$[-]$
F_D	Drag force	$[N]$
F_L	Lift force	$[N]$
F_T	Tangential force	$[N]$
Fr	Froude number	$[-]$
g	Gravity	$[\frac{m}{s^2}]$
i	Imaginary unit	$[-]$
i	Counter	$[-]$
K	Binomial coefficient	$[-]$
l	Length dimension	$[m]$
n	Order of Bernstein polynomial	$[-]$
N	Number of panels	$[-]$
q	Airfoil surface velocity	$[m/s]$
q_∞	Freestream velocity	$[m/s]$
R	VAWT radius	$[m]$
R'	Local VAWT radius	$[m]$
Re	Reynolds number	$[-]$

s	Coordinate along vortex and source sheets	$[-]$
S	Shape function	$[-]$
u	Horizontal velocity component	$[m/s]$
u_∞	Horizontal freestream velocity component	$[m/s]$
v	Vertical velocity component	$[m/s]$
v_∞	Vertical freestream velocity component	$[m/s]$
V	Flow velocity	$[m/s]$
V_b	Blade velocity	$[m/s]$
V_∞	Freestream velocity	$[m/s]$
V_{rel}	Relative blade velocity	$[m/s]$
x	Horizontal coordinate (abscissa)	$[-]$
x_p	Horizontal pitch location	$[-]$
y	Vertical coordinate (ordinate)	$[-]$
y_p	Vertical pitch location)	$[-]$
z_b	Blade position	$[m]$

Greek Symbols

Symbol	Description	Units
α	Angle of attack	$[rad]$
Γ	Circulation	$[1/s]$
γ	Vorticity	$[1/s]$
δ	Pitch angle	$[rad]$
ζ	Normalised y coordinate in CST	$[-]$
ζ_{TE}	Normalised trailing edge thickness in CST	$[-]$
θ	Angle between panel end point and evaluation point	$[rad]$
θ_b	Blade azimuthal angle	$[rad]$
λ	Tip speed ratio	$[-]$
ν	Kinematic viscosity	$[1/s]$
σ	Source	$[1/s]$
Φ	Velocity potential	$[1/s]$
ϕ	Flow angle	$[rad]$
Ψ	Streamfunction	$[1/s]$
ψ	Normalised x coordinate in CST	$[-]$
Ψ_0	Streamfunction constant	$[1/s]$
Ω	VAWT rotational velocity	$[rad/s]$

ω	Airfoil pitch rate	$[rad/s]$

Abbreviations

CFD	Computational Fluid Dynamics
CST	Class Shape Transform
HAWT	Horizontal Axis Wind Turbine
NACA	National Advisory Committee for Aeronautics
VAWT	Vertical Axis Wind Turbine

Chapter 1

Thesis Outline

This first chapter will provide on overview of the final report of this thesis research. It will start with an introduction into its main subject, placing it in perspective of current wind energy technology. With this background in mind, research goals are formulated afterwards. These have made sure this research has come to a good end. Lastly, the structure of this report is presented.

1.1 Introduction

Wind energy is in demand. Even now when the price of a barrel of oil has been historically low, countries all over the world are striving to implement more and more GigaWatt's of wind power. Several governments and international cooperations have set green energy targets to meet in the near future. Globally, it was expected to have reached an installed wind capacity of 260GW by the end of 2014, which is enough to provide some 4% of the global electricity demand, according to the World Wind Energy Association [1]. More recently, the European Wind Energy Association provided three scenarios for the future of wind energy in 2020. Based on their high scenario, an 85% increase in installed capacity to a 17% coverage of the total EU power demand is expected, says Moccia [2].

The latest global conflicts emphasise the need to reach that target, as a higher energy autonomy is desired. Governments and countries see the importance of a smaller dependency of imported oil and gas. This means that there is a turn towards locally produced energy [1]. Wind energy could provide this demand, being both regional and independent.

This shows the need for continuous research and development in wind power. Nowadays, a good state of the art is present, and large wind farms can easily be raised on land. Offshore sites prove a bit more challenging and costly, although not impossible. However, not all situations lend itself to the typical horizontal axis wind turbine (HAWT). Due to its high dependency on wind direction, high maintenance, and high centre of gravity, both mountainous locations and open-sea are problematic. This calls for alternatives such as the vertical axis wind turbine VAWT, according to Paquette and Barone [3] and Akimoto et al. [4].

This model can operate under every wind direction, is easily scalable, and has a low centre of gravity, so it can for instance be put on floaters anywhere on open water. Its stigma from the past, being inefficient and prone to fatigue, is lifted due to modern technologies. This means that it can finally catch up with the more mature technique of its horizontal axis counterpart. This makes the VAWT a good contender to participate in the coverage of the future power demand.

The current designs of VAWTs have little been changed since they were first patented [3, 4]. A common type is the Darrieus turbine, where aerodynamic forces on vertical 'wings' propel the rotor. Usually, symmetrical airfoils are used, as the blades need to be functional in both the upstream half of the rotation as the downstream (Sutherland et al. [5]).

However, it turns out that due to the operating conditions, this blade does not even act as a symmetric airfoil (Migliore and Wolfe [6], Zervos [7]). Namely, from the blade point of view, the flow is not straight, like in regular forward motion or for a HAWT blade, but is curved. This curvilinear flow will make the airfoil behave as it was a cambered one [6].

This 'flow curvature' has large ramifications for the turbine and its sub-components. Due to its rotation, the airfoil will obtain added surface velocities, resulting in a different pressure distribution and changed aerodynamic forces. This in turn affects the blade force distribution in either half of the rotation, usually with a decrease of turbine efficiency [6].

To obtain insight in chances for improvement, this research sets out to investigate these flow curvature effects. If this phenomenon can thoroughly be understood, positive changes can be made to airfoil design processes for future VAWTs [6]. After a scrutinization of relevant literature and summarising previous research, previously suggested flow curvature models will be implemented and tested. An existing panel method will provide solutions to compare to and this should prove whether existing models are already accurate enough.

Furthermore it is strived to model the curvature effects in an existing two-dimensional panel code. This code, XFOIL, is able to design an airfoil based on certain preferences, using its fast and proven algorithms. The benefit this system has over other, existing methods is that it is computationally cheap but still sufficiently accurate (Drela [8]). Also, it can not only produce inviscid, but viscous solutions as well. This is an advantage over other systems, for which viscous solving is normally expensive. This makes XFOIL very useful for airfoil design.

Also, the software is easily implemented in an airfoil optimiser algorithm. By varying the chord-to-radius ratio, the level of flow curvature can be adjusted, and its impact on airfoil design can be investigated.

This research could provide a sound base for the future development of the VAWT. With the enhanced XFOIL model, a closer approximation to reality is achieved, and the airfoil process can be made more accurate. Coupled with the airfoil optimiser, best performing airfoils can be sought for VAWT design cases including flow curvature. Improved airfoils can in turn aid the efficiency of the turbine, in the end helping to the cause of green energy and its proliferation.

Research Goals

Based on the statements above, the following main objective can be formulated:

"Investigate flow curvature effects and correctly implement these in the XFOIL code, as to optimise airfoil design for vertical axis wind turbines."

Along with the main objective, several intermediate research goals can be formulated. These will help guide the thesis work over its duration in order to successfully finish this thesis. Having achieved the following goals, it can be stated the main objective has been met as well.

- Compose previous information from literature on flow curvature and its effects.
- Implement and compare methods proposed by researchers in the past to model flow curvature.
- Develop a method to easily and accurately simulate flow curvature.
- Scrutinise the XFOIL source code and correctly implement flow curvature, keeping its original functionality intact.
- Verify the flow curvature models and XFOIL solutions using an existing unsteady panel code.
- Use an airfoil optimisation tool to investigate the impact of flow curvature on airfoil design.

Report Outline

Below an outline of the report is detailed, describing the main topics of each chapter.

Chapter 2: The Vertical Axis Wind Turbine This chapter will describe the current state of the art of the vertical axis wind turbine. A brief introduction to the turbine is provided, along with a comparison to the horizontal axis model. Also, a more detailed explanation of the working principle of the machine and the design of its airfoils is given.

Chapter 3: Flow Curvature The chapter will explain in depth the characteristics of flow curvature and the effects its has on the VAWT and its components.

Chapter 4: Methodology The methodology chapter will elaborate on the methods used to arrive at the results and tasks to be performed to finish this research. It will furthermore explain the expected outcomes and results of each task.

Chapter 5 U2DIVA Panel Code This chapter will verify the results of an existing potential flow panel method, so it can be used as a benchmark for future results.

Chapter 6: Flow Curvature Models Based on available literature, the methods which have been used in the past to cope with flow curvature will be scrutinised. They will be detailed and used to compute airfoil geometries and their pressure distribution. Afterwards, in a comparison it is ventured to investigate advantages or disadvantages of the methods.

Chapter 7: XFOIL This chapter will cover the XFOIL code and the modification of its algorithms. A detailed explanation of its working mechanism will be provided and a description of the source code. Afterwards, a model is developed to easily simulate flow curvature. This is subsequently implemented and a description of the modified code is presented. Its results will be compared to a benchmark in order to verify its accuracy.

Chapter 8: Airfoil Optimisation Using the newly modified XFOIL code, optimal airfoils are sought for a specific VAWT test case. By means of an existing airfoil optimising code, an optimal shape shall be found. This chapter will explain its working mechanisms and its results.

Chapter 9: Conclusions and Recommendations The final chapter will present the main conclusions and recommendations for future work.

Chapter 2

The Vertical Axis Wind Turbine

Ask anybody about wind energy and how it is harvested, and they will surely mention the typical horizontal wind axis turbine. However, this is not the only wind energy conversion system around. Already hundreds of years ago, systems with a vertical axis have been applied to aid man in various tasks. Over the course of centuries this model has been developed and fine-tuned into the turbines we see today, but not many know of. The reason for that is that research and development put their efforts into the horizontal axis version, mostly due to misconceptions about the VAWT and (past) advantages of the HAWT. Due to modern technology, the vertical axis wind turbine is no longer inferior and therefore enjoys renewed interest.

This chapters sets out to discuss the vertical axis wind turbine. First, a general introduction is started with a brief history of the VAWT. This explains when and how the modern turbines evolved, marking the most important developments. Afterwards a comparison is made between the vertical axis wind turbine and its horizontal axis counterpart. From this, the motivation for this research arises, as the VAWT shows promise, but still needs improvement.

Then, over the following sections, the introduction will become more detailed, as the working principle of the entire turbine and a blade cross-section are discussed. The former section discusses the foundations of power production of the turbine, and presents the necessary equations. The latter will explain in depth how the force production of a blade is realised, and will address some important aerodynamic phenomena.

2.1 Brief History of the VAWT

This section will provide a short overview of the most important developments of the vertical axis wind turbine. This also provides the opportunity to present the current concepts and their design reasoning.

2.1.1 Ancient Times

The vertical axis wind turbine is not a new concept. Actually the first turbines are thought to have been invented as early as the seventeenth century A.D, according to Hill [9]. One of the first documented vertical windmills originated from the Middle-East. A detailed drawing of such a mill is found in this reference, and is depicted in Figure 2.1. A rotor with either six or 12 blades covered with cloth, powered a millstone to produce flour. The wind was funnelled onto one half of the rotor, creating the drag force to turn it.

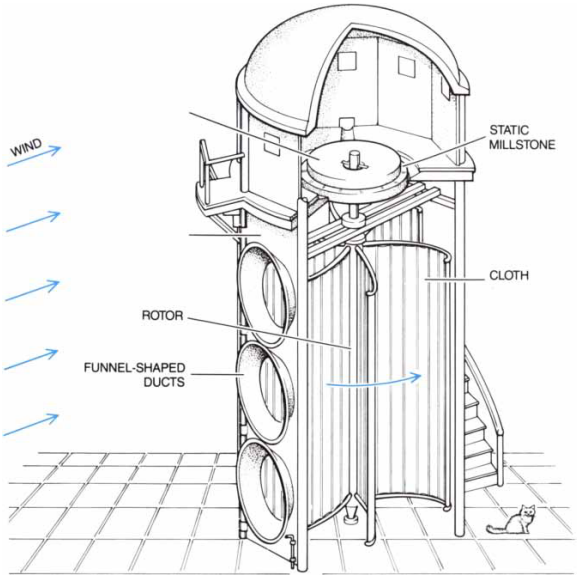

Figure 2.1: One of the first concepts of a vertical axis wind turbine, used for milling in the ancient Middle-East [9].

The vertical axis wind turbine would not yet be further developed, as the horizontal axis type became more popular in the late Middle-Ages in Europe and the rest of the world. This concept first started using the aerodynamic lift force on the blade to produce torque. It would have had to wait until the twentieth century, after the first oil crisis, for another developments on the VAWT, according to Shikha et al. [10] and Kirke [11]. This renewed interest led to the inventions of the most commonly found VAWTs today.

2.1.2 Modern Times

Like the Arabic version, the principle of drag driven force production is also applied in more modern concepts. The Savonius type turbine relies mostly on the difference between drag coefficient of either side of the rotor blades (Savonius [12]). Because of its low efficiency and large production costs, this concept is barely used today for large scale power production (Kirke [11]). However, it does find its use though in small-scale wind speed instruments (Islam et al. [13]).

A different principle of force production is applied on the Darrieus-type wind turbines. This concept, patented in 1931, relies on the aerodynamic lift production of its blades (Darrieus [14]). This provides for a more efficient torque and therefore power production. This is the type of VAWT is still widely investigated and applied, and will therefore be the focus of this thesis. A further description of its characteristics and working principles will be provided in subsequent sections.

For the latter concept two distinct shapes can be found. The first is an 'egg-beater' shape, where the blades are formed to have a troposkein shape. This shape, identical to a rope which is being swung around with both ends fixed, will reduce the bending stresses in the blade to a minimum ([14], Ashwill and Leonard [15]). The second variant is where the blades are parallel to the pivotal axis. These 'straight-bladed' Darrieus turbines work on exactly the same principles. A nice description and sketches of the three mentioned turbines are found in Islam et al. [13], which are shown in Figure 2.2.

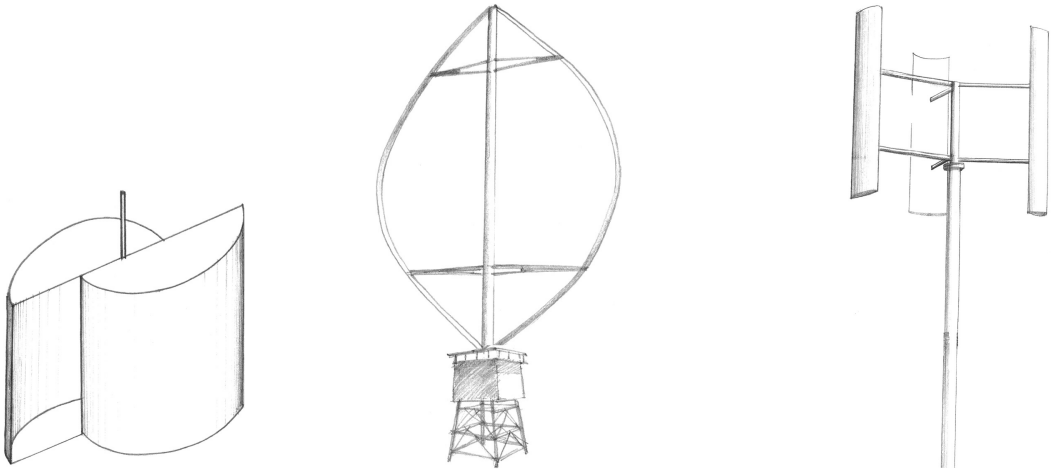

(a) Savonius type. (b) Troposkein-bladed Darrieus type. (c) Straight-bladed Darrieus type.

Figure 2.2: Sketches of the three mentioned modern VAWT types, as printed in [13].

The reason why there is such a large gap between the development of this technique is that "HAWTs emerged as the predominant technology for land-based wind" as mentioned by Paquette and Barone [3]. Back then, the rotor costs of the most applicable machine scales were lower than for a VAWT. Also, because of poor knowledge on fatigue loads on either concept, these rotors were fabricated of aluminium, which for a VAWT lead to premature failures. This, mistakenly lead to the assumption that all VAWTs were "inherently prone to fatigue", say Sutherland et al. [5]. Eventually, this meant that all the research and development was focussed on the HAWT, as mentioned by Akimoto et al. [4].

Due to recent ventures in offshore wind power, there is renewed interest in the VAWT. With new technology, the misconceptions of it being an inferior design is proven to be no longer true. Actually, it has some distinct advantages over its opponent, which will certainly prove it useful in the future. The following section will discuss the differences between the two designs in depth.

2.2 HAWT Versus VAWT

As mentioned in the Introduction, a trend is visible to produce energy more locally. In the ideal situation, this would go so far as to have an own wind turbine in your backward. Or, in tight, urban cities, on the rooftops of buildings. However, this poses some challenges, mainly because this terrain is so much different from the open spaces current wind farms are placed in. The turbines would need to cope with highly turbulent wind, in both magnitude as well as direction. And here, the vertical axis wind turbine seems to have the upper hand over the horizontal axis version (Benedict et al. [16] and Mertens et al. [17]).

In urban environments, the power density, the produced power per area, is an important characteristic of a wind turbine. Naturally, one would want to produced as much as possible on as little area. A HAWT does not seem to succeed in this aspect, as firstly an individual turbine sweeps a large circle with the radius equal to the blade length, and secondly, a farm with these turbines need significant distances between them, according to Kinzel et al. [18]. This leads to a low value for the power density.

With VAWTs however, the height of the turbine has a large influence on the power density, while the swept area can be kept equal. Also, these turbines can be placed much closer together, as the flow recovery distance could be less than half of that of a HAWT [18]. The result is that the power density of a VAWT can be three times more individually, or as much as 30 times more for a farm, compared with the HAWT [16]. Also, in an urban environment, the fact that a VAWT produces less noise due to its lower tip speed ratio (Kirke [11]), and that it produces more power in skewed flow (Mertens et al. [17], Simão Ferreira et al. [19]), make it superior to a HAWT.

Next to the power density, a modern VAWT has some distinct differences to its horizontal axis counterpart. A comparison between the most important characteristics of the two can be seen in Figure 2.3. More qualitative comparisons can be made between the two, as tabulated by Deglaire [20], and shown in Eriksson et al. [21]. Note that more generally, a VAWT is a cross-axis wind turbine, where its axis could even be oriented horizontally.

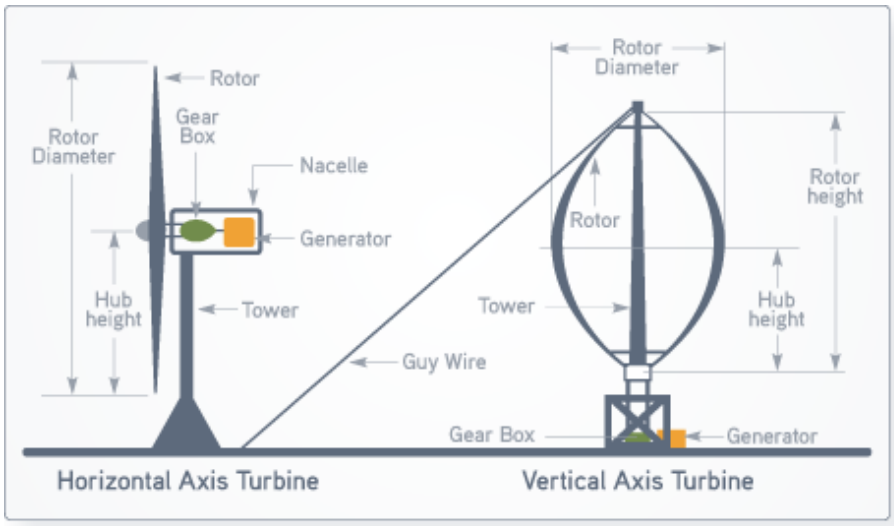

Figure 2.3: Definitions of a horizontal- and vertical axis wind turbine [1].

One of the key advantages the VAWT has, is that the heavy generator is placed near the surface, giving it a low centre of mass. This means that it is a perfect contender for offshore wind power, as it can be placed on tow-able floaters instead of on mono-piles in the seabed (Akimoto et al. [4]). A second big advantage, as mentioned, is that a VAWT can take wind from any direction, without yawing. Next to that there is no use for a complicated stall-mechanism, as the blades inherently offer this, this greatly reduces mechanical complexity (Eriksson et al. [21]). A structural advantage is that the blade can be made of a single airfoil shape, greatly reducing its complexity and fabrication effort, as mentioned by Sutherland et al. [5]. Also the blades and the turbine are better scalable, if structural requirements permit, than the HAWT, as that model will suffer from high gravitational loads [11].

[1] As found on `http://www.hillcountrywindpower.com/images/wind-basics-turbine.png`, visited on 08-05-2015.

Besides that the technology of the VAWT is underdeveloped and not as mature as of the HAWT, the vertical axis turbine does have some downsides which need further development. It is difficult to self-start, and may need a motor to do so [11]. Next to that, a VAWT is inherently prone to dynamic stall, say Simão Ferreira et al. [22]. This occurs when for low tip speed ratios the angle of attack of that blades increase above the stall angle of its airfoil. As a result, the blade stalls and its lift takes longer to recover due to shed leading edge vortices. Another disadvantage is that then the blades have to pass through this wake during the downstream half of the rotation [22]. This will result in diminished force production, and an asymmetrical force distribution, resulting in an increase in fatigue (Zervos [7]).

2.3 Motivation

The disadvantages of the vertical axis wind turbine mentioned in the previous section provide the motivation for this research. Namely, improved airfoil design could help alleviate some of them. Designing airfoil specifically for VAWTs could increase the efficiency and performance of the turbine. This thesis is focussed on exactly that, designing airfoils for VAWTs, and including an important aerodynamic phenomenon of the turbine; flow curvature.

If the airfoil profiles could be tailor-made for this type of turbine, its disability to self-start could be alleviated. Kirke [11] provides an extensive analysis on the developments of the VAWT and an investigation into the self-start. Beri and Yao [23] mention that cambered airfoils could help increase the torque at standstill, thus improving self-starting capabilities.

Another big disadvantage mentioned in the table is the issue of a short fatigue life. Application of better airfoils will result in a more desired load distribution of the blades, resulting in a decrease of fatigue loads on the rotor. Zervos [7] showed that cambering the airfoil will result in a more symmetrical force distribution over the rotation. Related to this is the issue of stall and the wake in the downstream part of the turbine. These phenomena have an accelerating effect on fatigue and must be avoided. The research of Migliore et al. [24] shows that by designing the airfoil shape specifically for a VAWT, this may be avoided. In the end, Migliore mentions, these changes will result in an increase in the efficiency of the turbine.

Next to these three topics, legion of other issues could be addressed with proper airfoil design specifically for a VAWT. This displays the merit this research has and the useful results it could produce. Hopefully, tailor-made airfoil could stimulate the research and development into the vertical axis wind turbine, helping it to catch up with the horizontal axis model.

2.4 Working Principle

As mentioned before, the Darrieus VAWT is the design under scrutinisation. This section will present the working principles of this turbine. Corresponding equations and variables will show how the aerodynamic forces on the blade result in power production. Afterwards, a detailed look at airfoil aerodynamics is taken as well. Important occurring phenomena are explained, which play a large role in the efficiency of the turbine.

2.4.1 Blade Aerodynamics

To obtain insight in the working principle of a vertical axis wind turbine, first its variables must be defined. Figure 2.4 shows how they are defined according to Goude [25], this reference also includes the equations below.

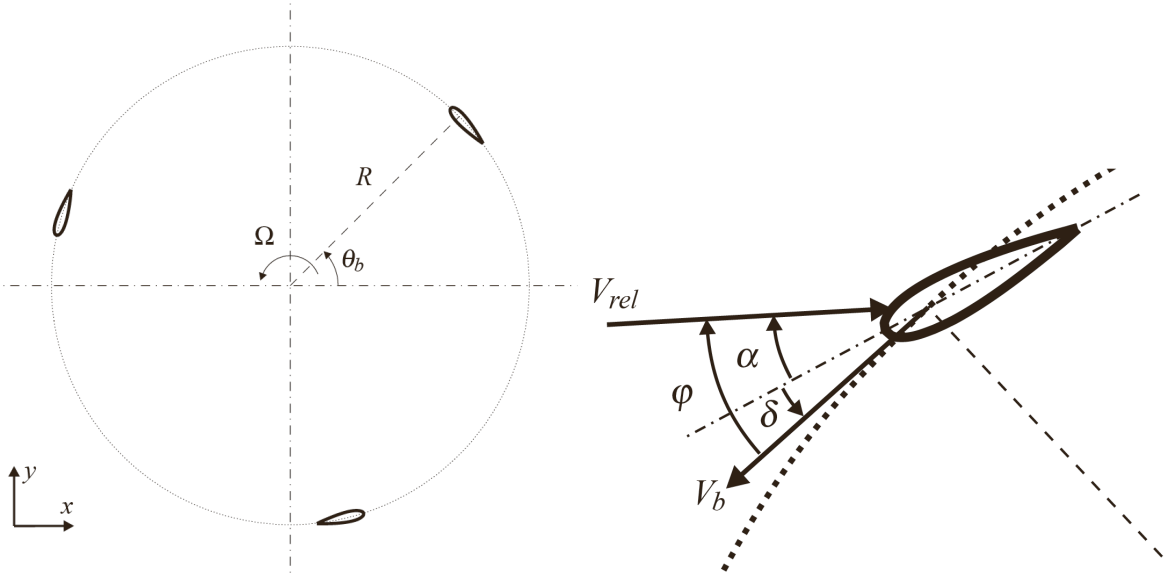

(a) Parameters concerning the complete turbine. (b) Parameters concerning a single blade.

Figure 2.4: Parameters concerning a vertical axis wind turbine [25].

The turbine operates on the basis of lift production. The blades, which are mounted away from a pivotal axis, evenly spread, undergo a rotational speed Ω in a flow velocity V. If the latter is written in complex form, the relative velocity can be found using Equation 2.3. Here the position of the blade is indicated in polar coordinates R and θ, as shown in Figure 2.4a.

$$z_b = Re^{i\theta_b} \tag{2.1}$$

$$V_b = i\dot{\theta}_b Re^{i\theta_b} \tag{2.2}$$

$$V_{rel} = V - i\Omega Re^{i\theta_b} \tag{2.3}$$

$$\phi = \tan^{-1}\frac{\cos\theta_b}{\frac{\Omega R}{V} + \sin\theta_b} \tag{2.4}$$

$$|V_{rel}| = V\sqrt{\left(\frac{\Omega R}{V} + \sin\theta_b\right)^2 + (\cos\theta_b)^2} \tag{2.5}$$

$$\alpha = \phi + \delta \tag{2.6}$$

$$F_T = F_L \sin\phi - F_D \cos\phi \tag{2.7}$$

$$\lambda = \frac{\Omega R}{V_\infty} \tag{2.8}$$

Based on the rotational and flow speed, and the blade location angle, the flow angle ϕ can be computed, assuming V is real. Using this angle and the pitch angle setting δ the angle of attack α can be found, as shown in Figure 2.4b. Together with the magnitude of the relative velocity, the lift force on the blade can be computed. Using the flow angle, this can in turn be converted to a blade normal and tangential force, according to Equation 2.7. The tangential force results in torque around the VAWT centre, leading to power production if it is sufficiently high.

A final note on definition; the upstroke of the turbine is considered the upwind half of the rotation. Consequently, the downstroke will be defined as the half of the rotation downwind.

2.4.2 Airfoil Aerodynamics

When a better look is taken at the flow around a cross-section of a blade, the airfoil profile, several phenomena and characteristics are important. These will be discussed below. Naturally, as it is the main topic of this report, the phenomena due to flow curvature will be discussed in more depth in following chapters.

Static and Dynamic Stall

As the tip speed ratio ratio decreases, the angle of attack increases. At lower ratios the angle of attack can become so high the airfoil enters stall. This has a destructing effect on the lift and an enhancing effect on the drag. Stall of an airfoil occurs when its angle of attack becomes so large, part of the flow can no longer neatly follow the contours of the airfoil, and detaches (Anderson [26]). This occurs in a highly turbulent manner, resulting in the loss of pressure, and therefore the loss of lift and a steep increase in drag. Behind the airfoil, a turbulent wake will be present, swept away with the fluid.

For a VAWT dynamic stall is problematic as well. This occurs as the angle of attack of the airfoil cyclically changes. When the stall angle is surpassed and then decreases afterwards, one would expect the same forces to be produced. However, due to the turbulent nature of the detached flow, this does not occur, and hysteresis effects are felt. For a VAWT blade this means that after stall, it takes longer for the airfoil to restore to a more laminar fluid state in parts of the rotation. A more detailed description can be found in Claessens [27].

Another downside of stall is that an airfoil in the second half of the rotation will be in the fluid disturbed by the first half of the rotation. If stall occurred there, this leaves a large wake, resulting in less stable flow for the airfoil there, leading to a decrease in force production. Typically for dynamic stall, a vortex at both the leading and the trailing edge is being shed into the wake (Fujisawa and Shibuya [28]), as shown in Figure 2.5. The lower the tip speed ratio, the more pronounced the effect.

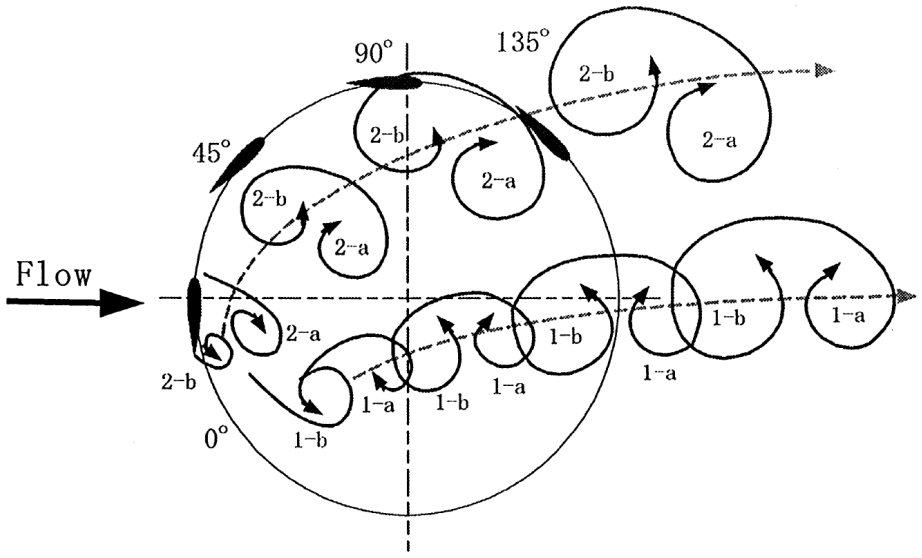

Figure 2.5: Vortex shedding in dynamic stall [28].

Reynolds Number and Laminar Separation Bubble

The dimensionless Reynolds number depicts the ratio of inertial over viscous forces, as shown in Equation 2.9. Here V is the flow velocity, l is a length dimension, and ν is the kinematic viscosity of the fluid. The magnitude, dependent on the velocity, indicates the flow regime, and dictates the aerodynamic phenomena. The behaviour of airfoils, like laminar to turbulent transition or stall, is highly dependent of the Reynold number. As a VAWT operates under various tip speed ratios, the number varies as well, resulting in highly changeable aerodynamics.

$$Re = \frac{Vl}{\nu} \tag{2.9}$$

Usually, it is considered VAWTs operate at fairly low Reynolds numbers compared to typical aeronautic applications, values in the 10^5 are to be expected (Deglaire [20], Islam [29]). A phenomenon which could occur over either surface of the airfoil is a laminar separation bubble. The laminar flow detaches due to an adverse pressure gradient, after which the detached flow eventually transitions and reattaches again. Hereafter laminar flow continues to follow the body. The formed bubble results in an increased drag and decreased lift coefficient.

An added phenomenon for a VAWT is a cyclic variation of the Reynolds number. Namely, due to the rotation there is a variation of the relative velocity of the airfoil. Migliore and Wolfe [30] have computed, for a specific case, the relative variation of the Reynolds number over a rotation, for various tip speed ratios. They related it to the nominal value of the number, as shown in Figure 2.6. As can be seen, assuming a nominal value in the first place is a stretch, and the fluctuations in Reynolds number will enhance the complexity of the flow and therefore calculations to approximate it.

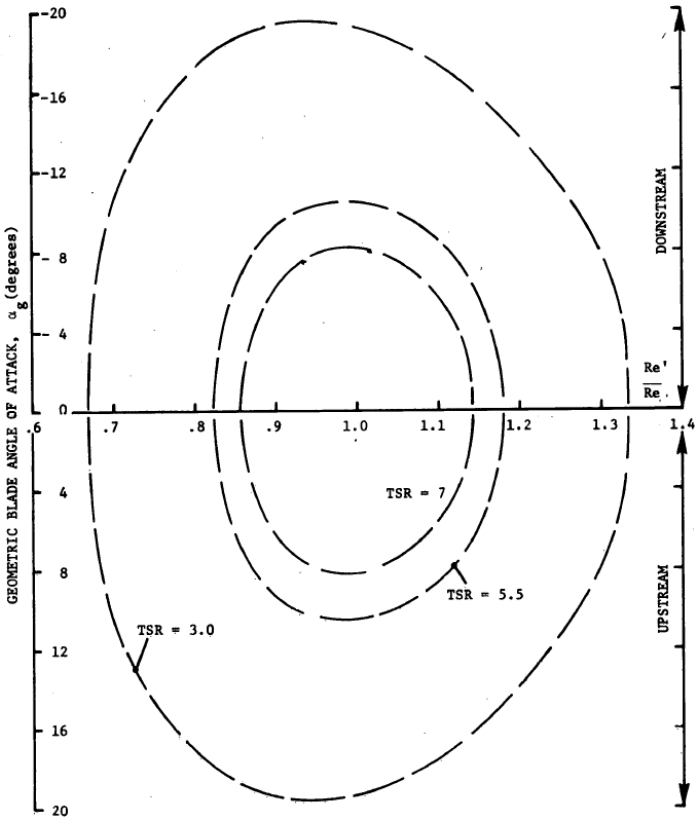

Figure 2.6: Reynolds number variation over one rotation for various tip speed ratios [30].

2.5 Airfoil Design for VAWTs

The above-mentioned behaviours of an airfoil impact VAWT design, and specifically its airfoil design. The shape and geometrics of the profile are dependent on these phenomena. Several references extensively investigate these questions and discuss desirable airfoil characteristics and geometrical considerations. Below a summary of those can be found. Before that, a brief overview of the current state of the art is given.

2.5.1 Past and Current Airfoils

As shown, the angle of attack varies cyclically, attaining both positive as negative values. It would make sense to use an airfoil which produces lift in both situations. And that is why symmetrical airfoils are originally used for the VAWT, mention Sheldahl and Klimas [31]. These airfoils are easily extruded or fabricated into straight or curved blades, without any twist, taper, or other sections, making them popular to use. Their thickness is ample to provide enough structural stiffness to the blades. Another advantage is that the aerodynamics of such profiles are extensively tested and documented, for instance like the NACA series. This made the NACA0012 and NACA0015 popular profiles for VAWT blades (Kirke [11]).

Although symmetrical airfoils are still being used, plenty research into cambered profiles has been performed in the past, according to Islam et al. [32, 33]. This has shown that these airfoils have promising effects. Especially the self-starting aspect of the turbine, which is currently problematic, might be solved with the use of cambered airfoils (Kirke [11], Beri and Yao [23]). Even when not only starting torque is considered, an optimal airfoil turns out to have a slight camber, as shown by Carrigan et al. [34]. Furthermore, Migliore [35] and Zervos [7] have shown that a more symmetrical, and thus more desirable, force distribution over the rotation can be obtained. They also show that an as high or higher efficiency compared to symmetrical profiles can be achieved.

2.5.2 Desirable Characteristics

Previous research has shown that cambered airfoils might prove useful in VAWT design. But several other aspects of an airfoil might also be desirable, as discussed by Klimas [36]. Below, the most important of them will be discussed.

- **Large stall angle and beneficial stall properties** Especially for low tip speed ratios the angle of attack the airfoil encounters can be very large. It is desirable that an airfoil stalls as late as possible to ensure that lift production remains. In addition, the drag accompanying stall has a negative influence on the torque, and should therefore be avoided as much as possible. Furthermore, once stall does occur, it should occur gradually and with as little lift decrease as possible. Trailing edge stall is preferable, as the separation location moves upstream gradually when increasing the angle of attack.
- **Large lift over drag ratio** This ensures that the lift production is as high as possible for the least amount of drag. Also in the lift over drag polar, the low drag bucket some airfoils have should be as wide as possible. This is an area of decreased drag, which should be used to an advantage.

- **Beneficial extremes for aerodynamic coefficients** The maximum lift coefficient of the airfoil should be as large as possible and the drag coefficient as low. Next to that it is desirable the airfoil should have a low drag coefficient when the lift is zero. This will make sure there is the least amount of counter-torque due to drag when the VAWT is starting up or operating at low tip speed ratios.
- **Roughness sensitivity** The airfoil should be as insensitive as possible to roughness on the surface. This could form by erosion of the surface due to weather circumstances or the impact of insects or dust. Usually, the aerodynamic performance degrades with increased roughness, but this decrease should be minimal.

2.5.3 Geometrical Considerations

The desirable characteristics mentioned above can be translated in to geometrical considerations. The parameters discussed below are the main variables in the design of an airfoil.

- **Thickness and location of its maximum** First of all, the thicker the blade, the stronger and stiffer the structure can be. And as mentioned by Islam et al. [32] thicker profiles can obtain higher performances, higher starting torques, and a wider low drag bucket. Also, Simão Ferreira and Geurts [37] confirm in their research in airfoil optimisation for VAWTs, that the profile thickness has "a beneficial effect" on the lift slope. They showed that thicker profiles are found during their optimisation of turbine power output. Furthermore, Qu et al. [38] explain that not only the maximum thickness, but also its location has a pronounced influence on the performance of the airfoil.
- **Camber** With an increase in camber comes an increase of lift and therefore torque. The mentioned references indicate that there is little change of performance for negative angles of attack, and an increase for positive ones. An increase in lift will result in an increase in torque, enhancing the VAWT's performance. Furthermore, [32] indicates that cambered airfoils are less sensitive to surface roughness.
- **Sharp trailing edge** Islam et al. [32] suggest that a sharp trailing edge could lead to a decrease in drag.

More exotic airfoil shapes are recently considered as well. As research and development in airfoil design for VAWT increases, more interest is given to shapes which passively or actively control the flow. One could think of a morphing airfoil to do so. Very little can be found on adaptive airfoils for VAWTs, but one research shows clear results of a flexible airfoil. Butbul et al. [39] have created a flexible blade which is able to morph passively under aerodynamic and centrifugal loads during operation. They show that for low wind speeds and low rotational velocities the morphed airfoil has an improved performance. However, as soon as the centrifugal loads become too high, the morphing of the airfoil becomes disadvantageous and the performance starts to diminish. The authors suggest that the morphing has beneficial effects on the self-starting characteristic of the turbine.

2.6 Chapter Conclusions

Each chapter shall be ended with a summary of its main findings. The most important conclusions are therefore listed below.

- This chapter starts of with the history of the vertical axis wind turbine, explaining the reason of its underdevelopment with respect to the horizontal axis version. This provided the motivation for this research as to decrease this gap by providing better airfoil design, which could alleviate some of the troubles the VAWT still suffers.
- The working principles of the VAWT and basic equations have been discussed. Furthermore, VAWT inherent aerodynamic phenomena have been explained, such as dynamic stall, the laminar separation bubble, and Reynolds number variation.
- These have led to a current state-of-the art for past and current airfoils for VAWT, which are primarily symmetric profiles as the NACA0012 and 0015.
- Lastly desirable characteristics of airfoils for VAWTs have been investigated. The profile should have amongst others beneficial stall properties, large lift over drag ratio, and a low sensitivity to roughness.
- Geometrical considerations should be the maximum thickness and its position, as this could enhance lift properties and provide structural stiffness to the blades. Furthermore, camber could alleviate the starting problems and will lead to less sensitivity to roughness.

Chapter 3

Flow Curvature

The just mentioned effects play an important role in the behaviour and performance of an airfoil. Another phenomenon is inherent to the aerodynamics of a VAWT; flow curvature. This effect arises due to a rotation around an offset centre, as on a vertical axis wind turbine. From the airfoil point of view, its motion is comprised of a translational movement and an added rotation. The added rotational velocities alter the behaviour of the airfoil, and this resonates in the performance of the VAWT. Therefore, during the development of a new turbine, flow curvature effects cannot be neglected in the airfoil design.

This chapter will present a discussion on the phenomenon flow curvature. Its origin will be discussed and afterwards the effect it has on increasingly larger sub-components shall be covered. This means that a discussion is presented on the repercussions it has on the airfoil, the blade, and the total wind turbine respectively.

3.1 Flow Curvature

One of the very first authors to mention flow curvature when regarding VAWT aerodynamics was Muraca et al. [40]. In their analysis on cross-axis wind turbines, they deduce that "Since the airfoil is travelling in a circular arc, the angle of attack varies along the length of the chord". Several subsequent authors mention somewhat similar phenomena, although an exact definition remains unclear. Therefore, before the concept is developed in further detail, a clear definition of the phenomenon 'flow curvature' is set for this report:

"Flow curvature is the phenomenon where, in the airfoil reference frame, curvilinear streamlines are encountered, resulting in a variation of angle of attack over the chord."

For a blade on a VAWT, this is the result of its own rotational velocity around an offset centre. Muraca calculated the influence this effect has on the lift production, and concluded, under their assumptions, that it is negligible. Although they mention that for increasing chord length it will become more important.

Muraca's conclusion is refuted by Migliore and Wolfe [6]. Their findings showed in fact that "the usual assumptions of constant blade velocity and angle of attack over the entire blade chord could introduce substantial error in blade aerodynamic analysis". Their results are visualised in Figure 3.1.

The report details the effects of flow curvature, and their results will be covered more extensively below. An interesting outcome is that experimental data using a symmetrical airfoil show that the minimum drag coefficient is not experienced at zero degrees of geometrical angle of attack. This leads to believe that a symmetrical airfoil in orbit does not behave as one due to flow curvature, as that is a typical characteristic of a cambered profile.

Not only via experiments a discrepancy between sectional data is investigated. Zervos and Roucous [41] proved using conformal mapping technique that the pressure distribution of an airfoil in pure translation is distinctively different from that airfoil translating with an added rotation. In essence, a VAWT blade in orbit performs exactly that motion, from the airfoil point of view, a translation and rotation. These results prove definitively that flow curvature will alter the aerodynamic performance of an airfoil section.

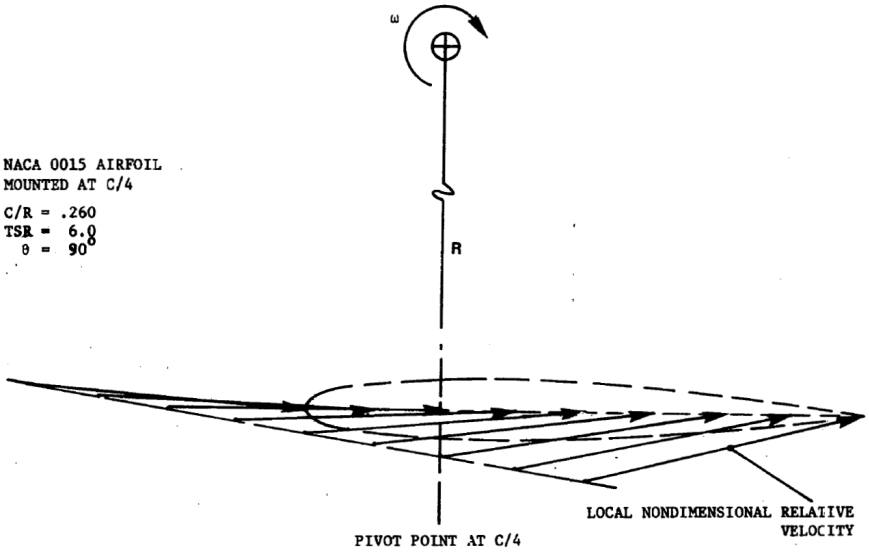

Figure 3.1: Variation of angle of attack over the chord [6].

3.2 Flow Curvature Effects

As mentioned, flow curvature markedly alters the flow around an airfoil, and therefore its aerodynamic behaviour. This influences not only the blade but on the entire turbine. Thus a thorough analysis of flow curvature effects will be provided below. This will be presented in three categories, each on an increasingly larger component of the turbine. Firstly, the changes concerning the airfoil are discussed, after which the influence on the VAWT blades is investigated. Thereafter, the entire turbine is taken into consideration.

3.2.1 Airfoil

Pressure distribution

In the airfoil coordinate system, a constant rotation around the VAWT centre, is equal to a translational motion and a constant rotational motion around its mounting location. This rotation causes added surface velocities, dependent on the distance of a point on the surface to the mounting position. As one can imagine, these altered velocities will change the pressure distribution, according to the Bernoulli equation. Zervos and Roucous [41] have demonstrated, using a conformal transformation, the pressure changes when a rotation is added.

Conformal mapping theory says a surface in one coordinate system can be related to one in another system. Through this transformation local angles will be preserved. The useful property of the transformation is that also potential flow can be related using these equations. In this manner, flow around a circle can be transformed to one around an airfoil shape. Zervos has applied this and computed the results for a NACA0012 airfoil in pure translational motion, and pure rotational motion. At an angle of attack of four degrees, a rotational velocity of 0.263 rad/s, and a radius of rotation of 5 chords, the pressure in Figure 3.2 was obtained. One can see that the added surface velocities due to rotation will translate to a change in pressure.

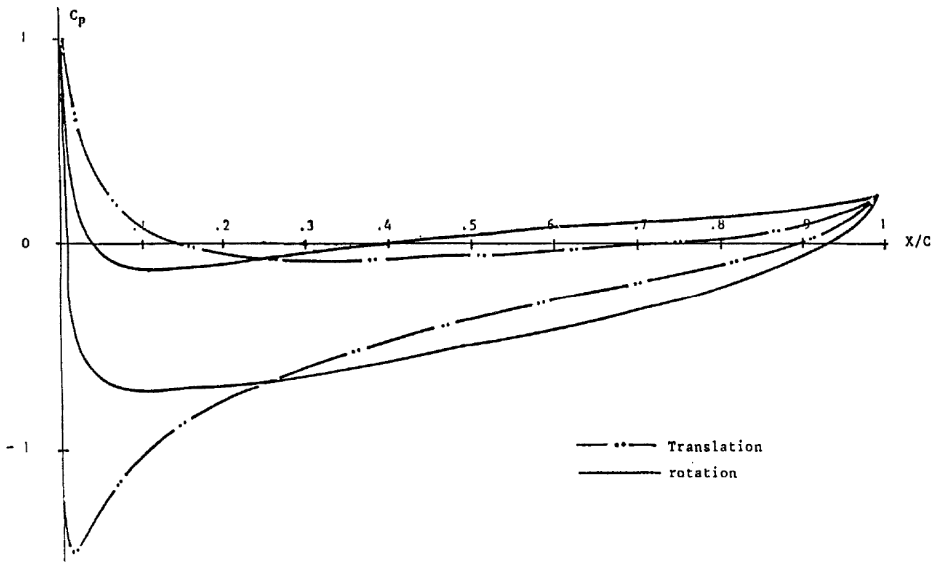

Figure 3.2: Pressure distributions for a NACA0012 profile at an angle of attack of four degrees, in pure translational and pure rotational motion [41].

The authors think that separation angles of attack will be different in both cases and therefore usual sectional data is not applicable. They mention that these should be regenerated for rotating airfoil, as a function of radius of rotation and Reynolds number.

Boundary Layer

Very little information on the boundary layer of a VAWT airfoil can be found in literature. Migliore et al. [24] mention some preliminary outcomes, which have not yet been realised. They argue that due to viscosity the fluid obtains its own rotational velocity, leading to centrifugal momentum and therefore forces. This "modifies the boundary-layer development on the blade surface and sweeps the fluid radially outwards from the trailing edge". By deriving the boundary layer equations from the incompressible Navier-Stokes equations they show that the normal pressure gradient through the boundary layer is at least one order of magnitude larger. As it is proportional to the square of the tip speed ratio ([24]), it quickly could lead to a high susceptibility to adverse pressure gradients and ultimately separation. As known, this has a destructing effect on the lift and an enhancing one on the drag.

They finally mention that as the angle of attack changes cyclically, in the upstroke separation might be delayed, while it can be accelerated during the downstroke. This is because of the fact that the suction side of the airfoil changes in the up- and downstroke. Therefore in the downstroke an added normal pressure gradient will enforce and already strong tendency to separate.

Centrifugal Effects

Migliore and Wolfe [30] suggest another approach to investigate the importance of centrifugal effects. By means of dimensional analysis they have investigated the relationship between viscous and external forces. The respective non-dimensional numbers are the Reynolds and Froude number. For the centrifugal force this can be calculated using Equation 3.1. The paper mentions that for external forces to be negligible to inertial forces, the Froude number must be much larger than one, which is met in the case of a VAWT. However, for the external forces to be negligible to the viscous forces, the condition of $\frac{Fr^2}{Re}$ being much larger than one must be satisfied. This requirement is not met, so therefore it can be concluded, centrifugal effects must be taken into account. However, up to now, no quantification of the effects has been performed.

$$Fr = \frac{V}{\sqrt{gl}} = \frac{\Omega R}{\sqrt{\Omega^2 Rc}} = \frac{1}{\sqrt{\frac{c}{R}}} \tag{3.1}$$

$$Re = \frac{Vl}{\nu} = \frac{\Omega Rc}{\nu} \tag{3.2}$$

Virtual Airfoil

The added rotational velocity of the airfoil will result in curved flow. To investigate the effects of flow curvature, several authors suggest a method to 'bend the curved streamlines straight', resulting in a similarly bend airfoil as well, as an illustration from [24] shows in Figure 3.3. Afterwards, analysis in rectilinear flow could result in desired sectional and pressure data. Through this transformation, a virtual airfoil is obtained with added camber and incidence angle. This approximation has been interpreted differently in various papers, demonstrating different airfoil transformations. Their methods will be discussed in chapter 6.

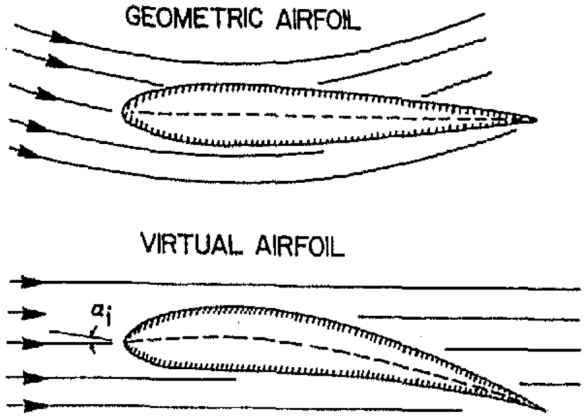

Figure 3.3: Virtual airfoil approximation [24].

Airfoil Sectional Data

Migliore et al. [24] hypothetically investigate the virtual airfoil characteristics, specifically its sectional data. The added camber will result in an upward shift of the lift curve, as it will produce more lift at the same angle of attack. The added incidence angle will result in a shift of the entire curve to the left. Note that these effects are opposite when the rotation is reversed, as is demonstrated by Zervos [7].

Also the drag polars demonstrate the existence of the virtual airfoil. By experimenting with a turbine in the absence of wind, the former authors could directly relate the drag of the blades to the counter-torque produced. Namely, the lift vector points towards the centre, so only the drag force produces a moment. By varying the rotational velocity, and the geometrical angle of attack of the blade, an effective drag coefficient could be measured. The results, shown in Figure 3.4, are important, as they show a minimum drag coefficient at an angle of attack different from zero, which was expected as they used a symmetrical profile. This indicates that the airfoils are acting as cambered ones. Note that these curves are obtained under quite a few assumptions, and are only indicative.

The experiments were performed with one of two blades, a smaller and a larger one. This difference translates into a different chord-to-radius ratio, indicated with $\frac{c}{R}$. One can imagine, that as the chord length increases, the variation of angle of attack over the chord increases. As a result, the angle between the chord and the rotational velocity varies, as this vector is always normal to the local distance vector to the VAWT centre. The leads to a variation of normal velocity over the chrod, and a change of magnitude of flow curvature and therefore its effects.

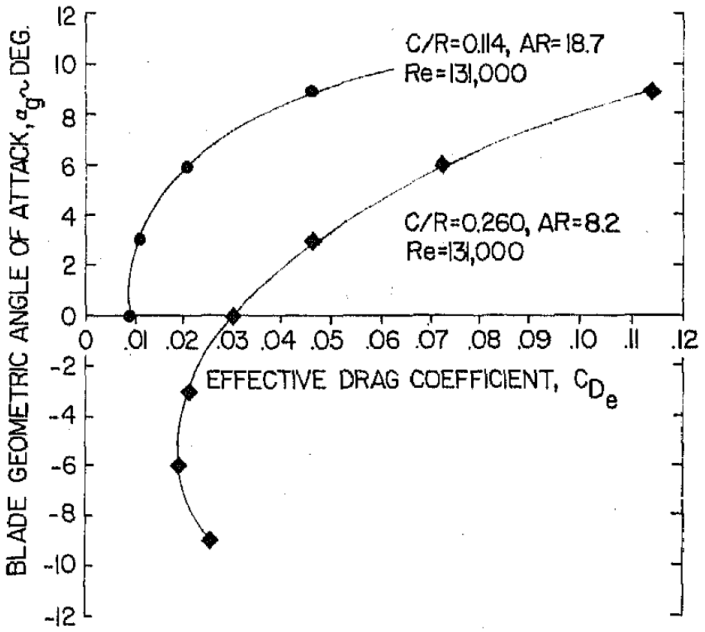

Figure 3.4: Effective drag coefficient measurements [24].

3.2.2 Blade

Tangential and Normal Forces

By applying their cascade model, similar to what is used in turbo-machinery analysis, Mandal and Burton [42] show that including flow curvature effects enhances the accuracy of the solutions. Figure 3.5 shows their computed results, comparing them with experimental data. The solid lines represents the model including the flow curvature effects, the dashed without, and the squares are the experimental results. The way they included flow curvature was by modifying the airfoil to a virtual one, based on the method by Hirsch and Mandal [43]. This method shall be investigated later in this report.

As can be seen, the results improve with inclusion of the virtual airfoil. Especially in the upstroke, that model is the most accurate. A similar result is obtained for the normal force component. Again an improvement is obtained with inclusion. It must be noted that next to flow curvature, a dynamic stall model is also added to enhance the results.

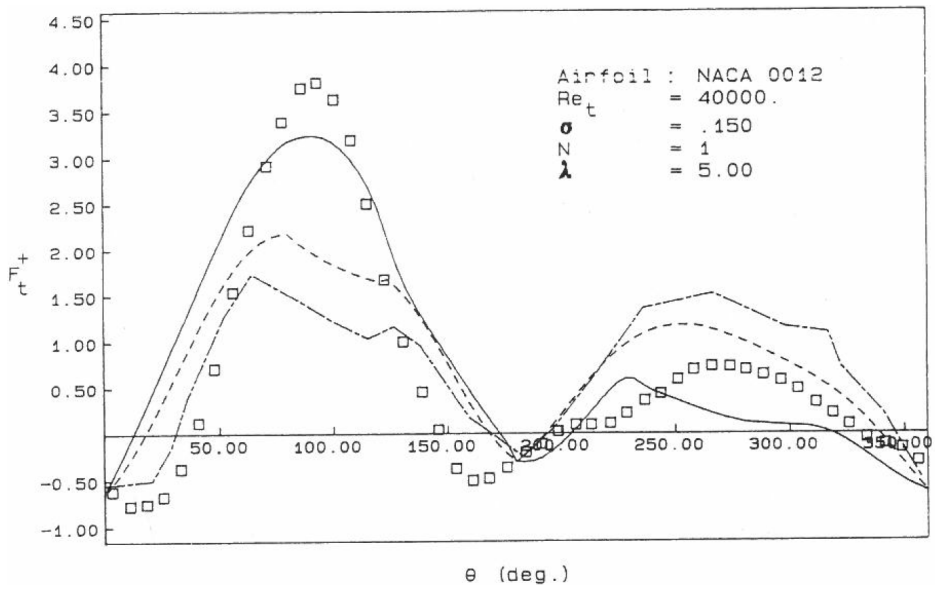

Figure 3.5: Tangential force computed using a model without (--) and with (-) flow curvature effects, compared to external experimental data and that author's model (-.) [42].

Also Zervos [7] shows results for the force components on the blade. Computed for a tip speed ratio of six and a chord-to-radius ratio of 0.15, the tangential and normal forces on blades with different profiles are shown in Figure 3.6. Due to flow curvature effects, a symmetrical airfoil will produce a very asymmetrical force distribution over one rotation. This is ascribed to a higher lift production in the upstroke, due to the change in lift coefficients, and a increased drag production in the downstroke.

The author mentions that compensating for the virtual camber and incidence could be a way to alleviate the loss of efficiency. Zervos computed that using a cambered profile, the force distribution became more as desired. This improvement can be seen in the figure when comparing the curves for the NACA0015 and the cambered GAW(1) airfoil. He furthermore proposed a custom airfoil, having the thickness of the NACA0015, but the mean camberline as described by the path of the blade. This ARC0015 profile performs even better, leading to a more symmetric distribution.

Torque

The shift of sectional data has important effects on the forces and moment production of the blades. If assumed that the virtual camber and incidence are constant, Figure 3.7 could be the variation of both the geometrical and virtual angle of attack. Qualitatively the indicated regions in the plot can be said to have reduced power production efficiency. Namely, due to added incidence in region one, the stall angle is surpassed, leading to counter-torque due to drag increase. In region two the signs of the lift coefficient and virtual angle of attack are opposite, leading to counter-torque. And finally, in region three, the absolute value of the virtual angle of attack is smaller, so there will be diminished power production.

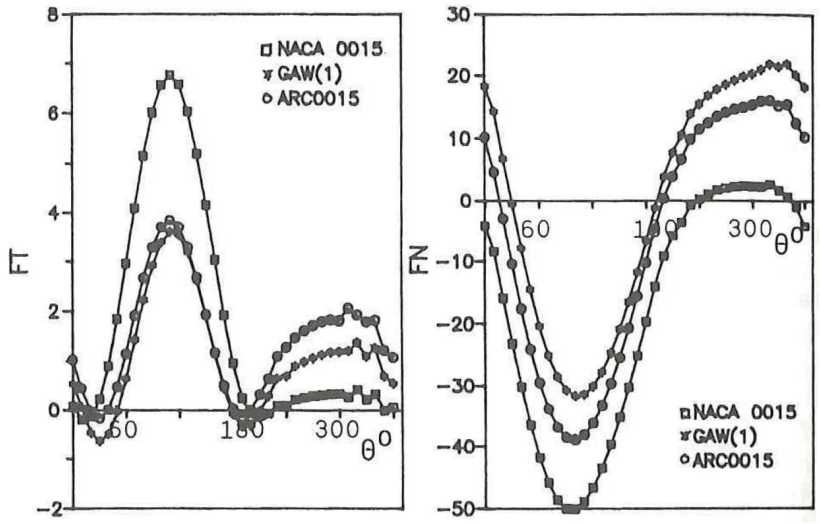

Figure 3.6: Tangential and normal force components computed for three different airfoils [7].

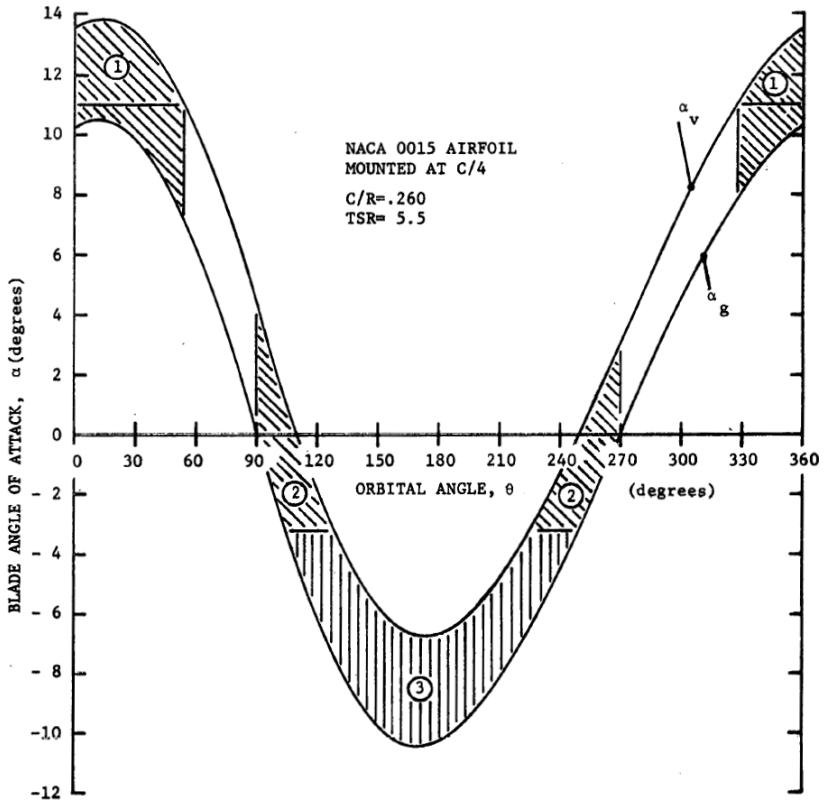

Figure 3.7: Variation of (virtual) angle of attack over one rotation [30].

3.2.3 Turbine

Instantaneous Power

As the flow curvature affects the force and torque production, power is affected as well. As mentioned, there are parts of the rotation which experience counter-torque even, which leads to a loss of power into the flow. Migliore and Wolfe [30] have quantified the effect on power by measuring the torque using an effective drag coefficient, and in turn calculating the power by integrating over the rotation. The results are shown in Figure 3.8, where the "measure of merit, proportional to the torque output and power coefficient" is shown for two blade configurations.

As can be seen, increasing the chord-to-radius ratio, thus increasing flow curvature effects, has a large effects on the power production. Compared to what was expected with the geometrical airfoil, the smaller $\frac{c}{R}$ blade has a slightly increased power production in the upstream half, and a reduced one in the downstream, resulting in a net power decrease. The large chord-to-radius ratio suffers larger effects, and endures stall in the upstroke and a largely decreased power production in the downstroke. One can even see that the power is negative, indicating it is lost to the fluid.

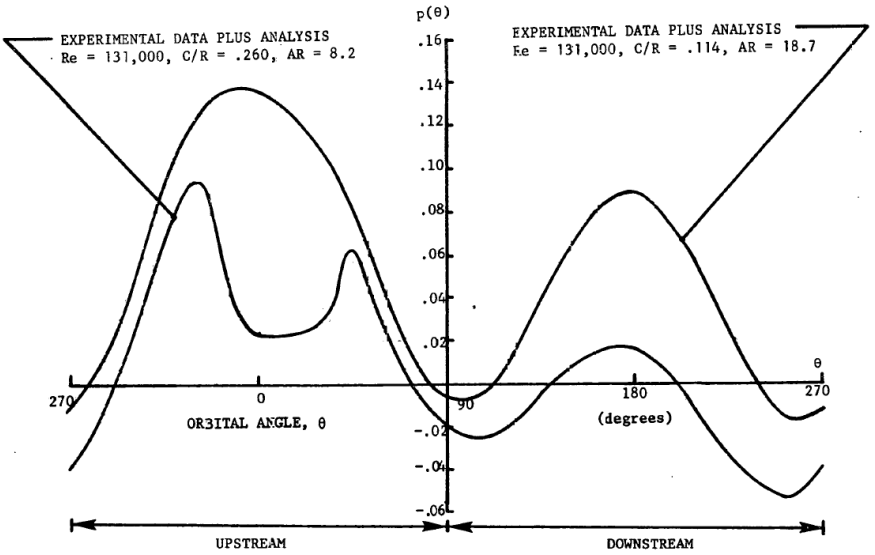

Figure 3.8: Experimental power curves for two chord-to-radius ratios [30].

Power Coefficient

Mandal and Islam [44] have numerically investigated the effects of flow curvature on the power. By applying a virtual airfoil transformation, to be explained in chapter 6, they have included flow curvature in their model. By comparing the results for both the model with modification and without with experimental data, they have concluded the effects cannot be ignored. Figure 3.9 shows the outcomes, where the most important lines are the dashed and dash-dot-dash line, respectively the model without and with flow curvature. The squares are experimental data, obtained from Migliore and Wolfe [30]. As can be seen, the accuracy of the results improve when flow curvature is taken into account.

The figure furthermore depicts the difference in flow curvature models, as the dotted line is Migliore's [30] and the dash-dot dot-dashed line is Muraca's [40]. This shows the need for a thorough analysis of available flow curvature models, and a comparison of their results.

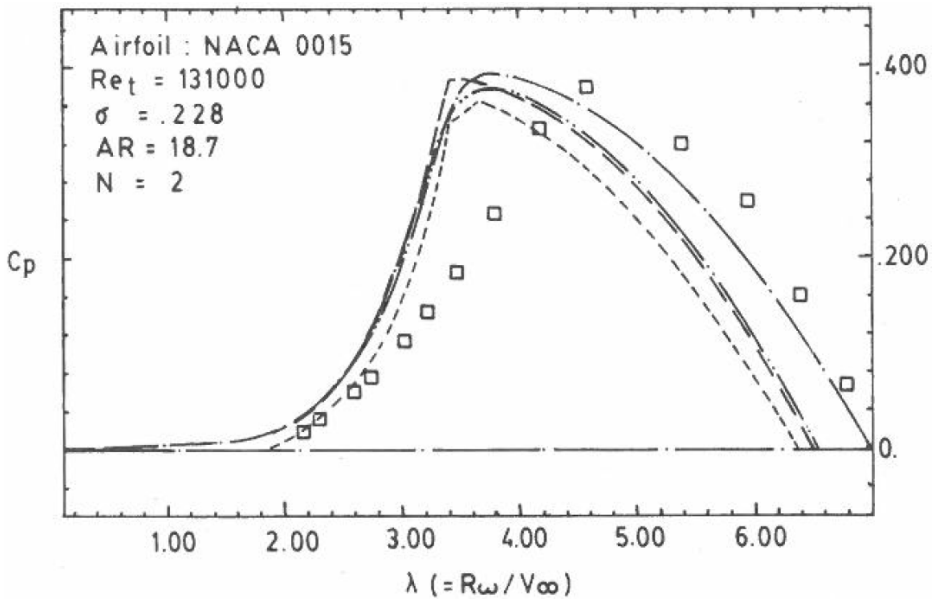

Figure 3.9: Power coefficient as a function of tip speed ratio for different models, compared with experimental results [44].

Computational Fluid Dynamics Results

Another research on the power afflicted by flow curvature is by Benedict et al. [16]. Their experiment showed that there is power extraction in the upstroke, and possibly power loss in the downstream half of the rotation. To verify this, a Computational Fluid Dynamics (CFD) model was constructed to investigate the outcomes. The paper shows results from analyses with varying pitch settings, tip speed ratios, and Reynolds numbers. An example of their results is shown in Figure 3.10, showing the pressure contours and streamlines around a turbine, and depicting the mean camberline of the virtual airfoils.

The figure shows that in the upstream half, the added camber and incidence increase the lift force and hence the tangential force (the force tangential to the rotation, and not to the airfoil). The low pressure on the suction side on the upper surface of the airfoil indicates this high lift force. During the downstroke, the fixed blade is operating with negative virtual camber, and a large angle of attack. This results in large flow separation, leading to a negative power production. Next to that, the researchers believe that "massive bluff-body type of separation in the rear half for the fixed-pitch case is even affecting the flow upstream in the frontal half". This is indicated by the expanding streamlines shown in the figure from through the centre of the turbine.

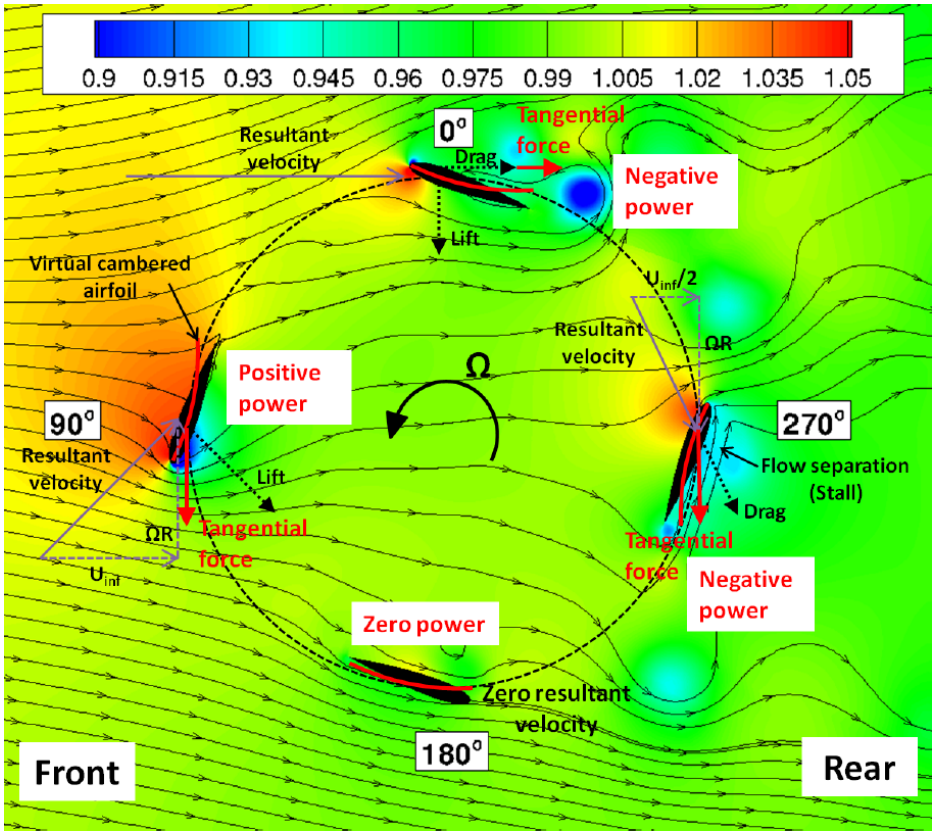

Figure 3.10: Pressure distribution and streamlines around a turbine with fixed pitch.

3.3 Chapter Conclusions

- Flow curvature arises as the airfoils of a VAWT undergo a rotation around its centre. This will lead to a variation of angle of attack over the chord, leading to various effects.
- The additional velocities due to the rotation will alter the pressure distribution and the centrifugal forces will affect the boundary layer as fluid will be swept outwards.
- The rotating airfoil can be approximated by a virtual one with added camber and angle of incidence. This virtual transformation will provide the ability to perform analysis in straight flow, for instance on airfoil sectional data. This showed that a symmetrical airfoil on a VAWT has a minimum drag coefficient at a non-zero angle of attack, indicating flow curvature adds (virtual) camber to the airfoil.
- On a blade level, flow curvature affects the normal and tangential force, leading to a more asymmetrical force distribution. Due to the added camber and incidence, more lift is generated in the upstroke, and more drag in the downstroke.
- This affects the torque and power output of the turbine leading to diminished power conversion from the flow.
- The shedding of the wake from the upwind half of the turbine is increased due to the larger lift force. And the increased wake in the downstream, due to a large amount of separation, propagates forward to affect the upstroke.

Chapter 4

Methodology

To ensure that correct and usable results are obtained, each analysis has to be thoughtfully constructed. This will prevent losing time on obtaining wrong results or waiting on unusable simulations. Therefore, will introduce the methods with which the desired results and outcomes are obtained. It will present a chronological order of actions taken over the duration of the thesis. This roadmap will provide a clear insight in the applied methodology. Furthermore, the expected results will be detailed per topic.

4.1 U2DIVA Code

When the XFOIL code is adapted, it must be ensured that it produces accurate results. Also, the implemented flow curvature models need to be checked and compared. Therefore it is necessary to verify the outcomes to methods which are already accepted to be correct. This shall be done with a comparison to a panel code created by Simão Ferreira [45] of the Wind Energy faculty of the Technical University of Delft, called U2DIVA.

This code is able to compute the desired airfoil characteristics in potential flow, so it can be compared with the inviscid XFOIL solution. To be certain this code produces accurate results, it shall be verified as well. For the steady solution, the conformal mapping technique of Benson [46] is used to produce an analytical solution. For the quasi-steady pitching solution, a comparison is made with documented results in the thesis of Ghodoosian [47]. After this verification, the panel code shall be used as the primary benchmark.

The results in this section will show how the pressure distribution of the U2DIVA code matches against a theoretical solution in steady flow. Also it will be shown how the pressure compares with tabulated data in the mentioned thesis.

4.2 Flow Curvature Models

It has been shown previously that an airfoil in VAWT rotation can be approximated by a virtual airfoil in straight flow. Now, several authors have demonstrated what the impact of flow curvature can be on the airfoil of a VAWT. Even though more references can be found depicting the results of their methods, only five also present the equations necessary to reproduce these. Therefore, a comparison will be presented between the following references: Migliore et al. [24], Hirsch and Mandal [48], Zervos [7], Gregory et al. [49], Akimoto et al. [50].

The airfoil to virtual airfoil transformation is interpreted by the authors in a slightly different manner. The usual approach is to alter the camber line of the airfoil, and include a virtual incidence angle. However, how the flow curvature effects are interpreted varies in the references. Therefore, it is set out to compare the available methods, based on the calculated airfoil geometries and pressure distribution they compute. Afterwards, their results will be compared with the verified solution of the U2DIVA code.

The results will serve two purposes, firstly to show the differences in calculation methods in literature, and secondly to show whether these simple transformations could replace more computational expensive methods. Namely, if the results compare well enough, simulations using XFOIL or other panel methods might be unnecessary.

Expected results are the different virtual airfoils. Inspection of these will show the differences between the methods and (dis-) advantages of them. Furthermore, their pressure distribution will show which method might perform better, and which show undesired behaviour. Lastly, an objective error measure is used in which situations one methods might be preferable to another.

4.3 XFOIL

The main purpose of this thesis is to include the flow curvature effects into the simulation software of XFOIL. This will provide the ability to compute airfoil characteristics for both inviscid and viscous flows. This will be achieved in the following manner. As will be shown, a VAWT blade in rotation is equivalent to that blade performing a rotation about its mounting location. Therefore, it suffices to model an airfoil undergoing an quasi-steady pitching motion.

The additional velocities this motion induces are included in the XFOIL algorithms. By altering the source code, a new operation can be included where the pitching rate and location are defined by the user. The result would be the surface velocity distribution, boundary layer characteristics, normalized force coefficients, etc., for simulations with and without viscosity. If this alteration is made high enough in the chain of equations of the algorithm, the viscous and inviscid solvers need not to be altered and the quasi-steady solution will be correctly calculated straight away.

The results will contain the modified XFOIL source code. This alteration will be made as such that all previous functionality is kept intact. The resulting pressure distribution will be verified with the U2DIVA panel code, as to confirm its accuracy. Furthermore an investigation into the variable parameters of the model is presented, indicating their influence on the accuracy of the solution.

4.4 Airfoil Optimisation

After it has been shown that the new XFOIL code produces acceptable results, it will be used in an airfoil optimiser. The Optiflow optimiser, developed by de Oliveira [51] for his master thesis at the Wind Energy faculty of Delft University of Technology, is able to obtain a number of optimal airfoils computed for a specific test case. They code uses a genetic algorithm to produce a large set of possible airfoils. These are fed into the optimiser, which is coupled with the altered version of XFOIL. The optimiser will determine which profiles would fit two objective functions best, developed by Simão Ferreira and Geurts [37]. The resulting airfoils would be the best option for the chosen test case.

The purpose of this optimisation is to compare airfoils obtained without and with flow curvature effects included. The effect of increasing the amount of flow curvature on the geometry of the optimised airfoils shall be investigated. Any distinguishable trends shall prove whether this has to be taken into account in the design of airfoils for vertical axis wind turbines. A power estimation for a two bladed VAWT will be presented as well, for a selection of the airfoils.

The results in this chapter will be comprised of a set of optimal airfoils for a number of test cases with varying pitching rate. Their geometrical parameters shall be plotted to investigate whether they follow a trend. And lastly, it shall be checked whether any of the virtual airfoil transformations could be applied instead of optimising for the airfoil.

Chapter 5

U2DIVA Panel Code

Few methods are available which can both accurately compute the performance of an unsteady airfoil and are computationally cheap. In order to show whether the flow curvature models or XFOIL implementation actually produce correct results, a quick and correct benchmark method is desired. For this thesis, this comes in the form of an existing panel method.

This very brief chapter will cover the U2DIVA panel code developed by Simão Ferreira [45]. This code is part of an inviscid two-dimensional turbine analysis method, developed to investigate the wake of a VAWT. The method will be used as a main benchmark for future results and shall therefore have to be discussed and verified. This is done in below.

5.1 Description

The original panel code is an inviscid, incompressible single wake, source and doublet panel method, based on the potential flow. It takes any airfoil shape, within reasonable bounds, and computes the pressure distribution and aerodynamic coefficients using a Dirichlet boundary condition. The Kutta condition is applied to make sure there is no pressure difference over the trailing edge.

To apply the software in this situation, the wake is neglected and has no influence on the solution. To obtain a quasi-steady, pitching solution, the rotation of the airfoil is taken into account by including the rotational velocities. This is implemented by including the resulting perceived velocity on the airfoil surface in the calculations beforehand. In this manner, it will be propagated through all the equations and should produce the correct solution.

5.2 Verification

To be sure the U2DIVA code produces accurate results, two verification analyses are proposed. Even though this has already been done before, for good measure the steady solution shall be verified again. Furthermore, as it is an addition to the method, the quasi-steady pitching solution shall be verified.

5.2.1 Steady Solution

The steady solution is verified using a conformal mapping technique described by Benson [46]. This method is able to find the analytical solution of a Joukowski airfoil in both steady and unsteady situations, based on the same principles as explained before for the method of Zervos and Roucous [41]. Sadly, after a lot of time put into developing the code, the equations for the unsteady solution do not work properly and can therefore not be used. However, the steady solution can still be of use here, and the results are shown in Figure 5.1.

A Joukowski airfoil with thickness parameter 0.25 and camber parameter 0.1 is compared with the panel code. As can be seen, the results compare very well. The largest error is at the trailing edge, where the airfoil profile becomes so thin, the panel code has difficulties computing. The panels at this cusped edge are so close together numerical errors occur. Any other discrepancies can be attributed to numerical errors, which diminish with increasing number of panels. The solutions have been verified for other Joukowski airfoils as well.

For further reference, the method and equations are presented in Appendix A.

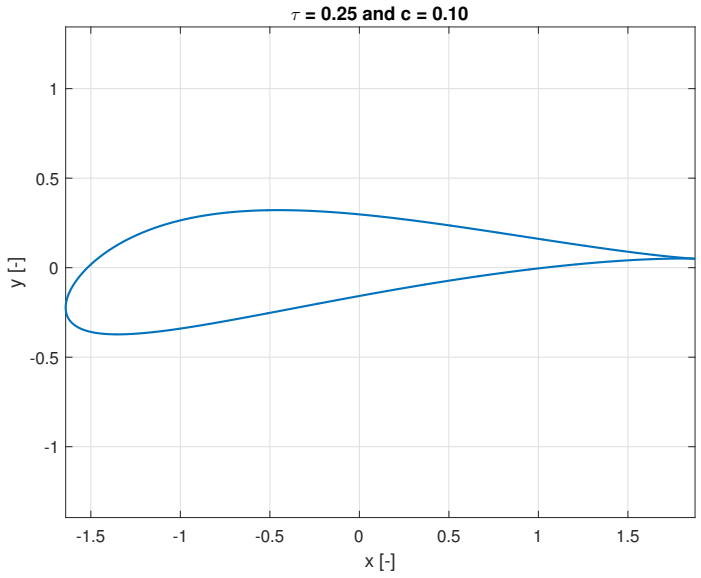

(a) Joukowski airfoil with thickness parameter 0.25 and camber parameter 0.1.

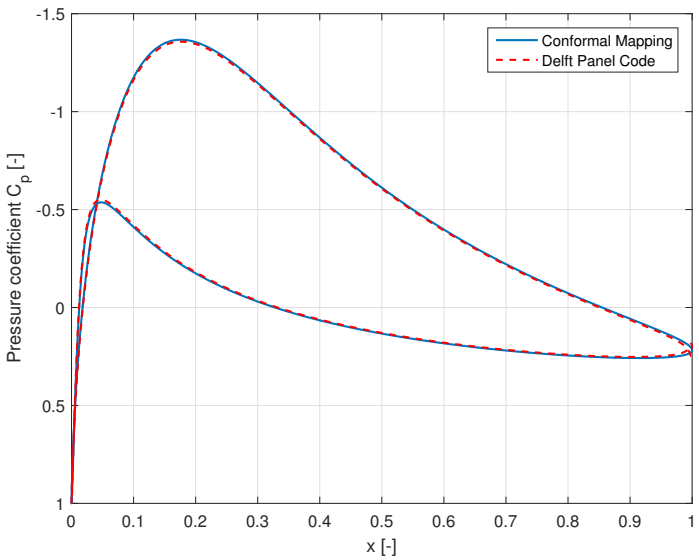

(b) Analytical pressure distribution and the panel code solution.

Figure 5.1: U2DIVA panel code verification with the Benson conformal mapping method.

5.2.2 Quasi-Steady Solution

As the analytical solution is not available in an unsteady case, different verification methods were sought. One was found in the work of Ghodoosian [47]. The method relies on transforming an airfoil to a pseudo-circle and integrating its surface variables to a full circle, of which a pressure distribution can be calculated using known equations. The equations for the method are far to complicated to implement in a short amount of time, but for a single test case tabulated data is provided in an appendix. For a NACA0015 profile with 6 degrees of angle of attack, a pitching rate of 0.07, and a pitching location on the chord at 38%, the results are shown in Figure 5.2. Again the panel code solution compares well.

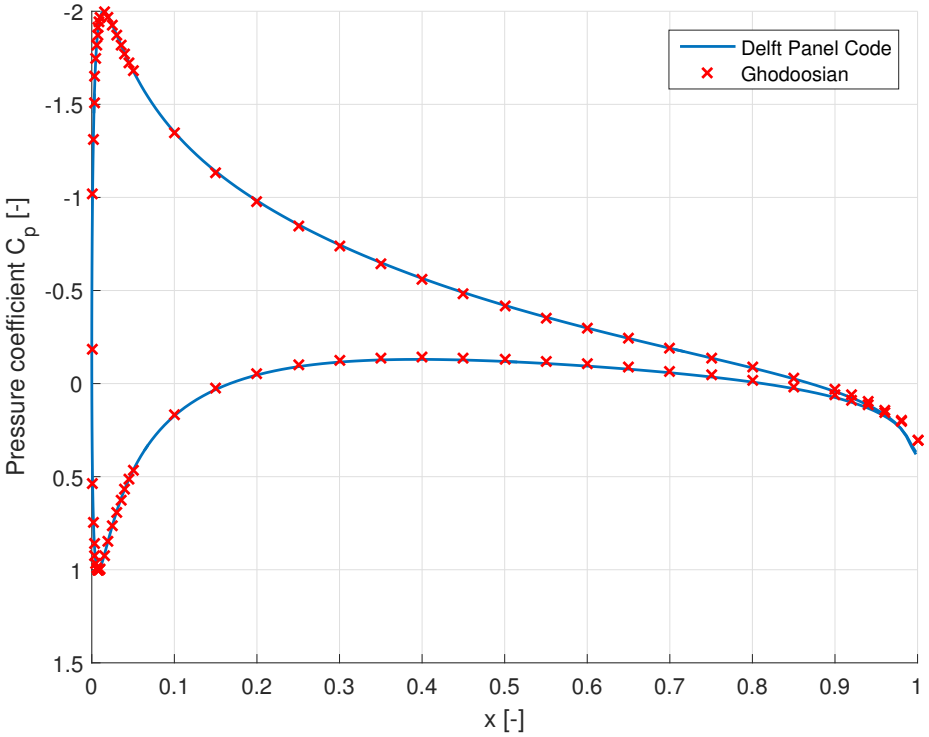

Figure 5.2: U2DIVA panel code verification with the Ghodoosian tabulated data.

As neither solution is analytical, it cannot definitively be said that both solutions are correct. But it is highly likely that if they correspond, this will be an accurate solution.

Therefore it can be concluded that the U2DIVA panel code performs accurately and can be used to produce benchmark results for future analyses. It must be noted that whenever this panel code is used in a comparison, inviscid conditions are used, as it is unable to include viscosity. This shall be true for the rest of the report.

5.3 Chapter Conclusions

- The U2DIVA panel code is an airfoil analysis tool based on an inviscid, incompressible potential flow solver. Using sources and doublets on a panelled airfoil, its aerodynamic behaviour can be tested in steady and quasi-steady situation.
- The steady solution is verified with the exact pressure distribution of a Joukowski airfoil. The pitching solution is verified based on third party data.
- It can be concluded the panel method is accurate.

Chapter 6

Flow Curvature Models

The knowledge that an airfoil in rotation behaves differently from a static one could stem from as early as the 1970s. Over the past decades some researchers have investigated such airfoil motions and found behaviours which could be categorised as flow curvature effects. A discussion will be presented on how various authors have coped with modelling flow curvature effects in the past. In general, all methods propose a transformation of a rotating airfoil to a virtual one which can be analysed in straight flow. Their different interpretation has led to different calculation approaches, and therefore different outcomes. Some models only vary minutely, whilst other compute the results on an entire different principle.

The virtual airfoil geometries of each method will be used to compute a pressure distributions in steady rectilinear flow with the U2DIVA code. These shall be compared with the panel code quasi-steady pithing solution. This will show whether these methods could be computationally cheap and easy alternatives to implement. It shall also provide the ability to conclude which model is preferable over the rest.

The chapter is structured as follows; first a description of each method is given, after which a comparison is made between their results, and a verification with the panel code. Finally, some conclusions shall be presented on the performance of the models.

6.1 Airfoil Transformations

As mentioned, th virtual airfoil transformations differ. They range from mere altering the camberline and adding the original thickness, to full conformal mapping, preserving local angles. However, not all literature is detailed enough to reproduce the models and results. Only five authors have been found which elaborate enough on their transformations. A sixth method is used based on general theory. These will be discussed below, after which in the following sections, their results will be discussed.

6.1.1 Migliore

One of the first to propose a transformation to a virtual airfoil are Migliore and Wolfe [30]. This transformation is based on conformal mapping. In their appendix, all the equations are derived, while only the most important steps in this derivation are shown below.

The authors argue that for a coordinate system rotating about an offset centre, the instantaneous streamlines form concentric circles. These are dependent on the tip speed ratio and the azimuthal position. Using a polar coordinate transformation these circles are transformed to straight lines. According to the authors, as conformal mapping is applied, the local angles of attack will remain the same. The equations are applied on a coordinate system with its origin at the blade mounting location. To relate the blade geometrical coordinates to this system, use can be made of Figure 6.1a. The x and y coordinates can be transformed to p and q coordinates in the blade coordinate system. This is merely a translation and rotation.

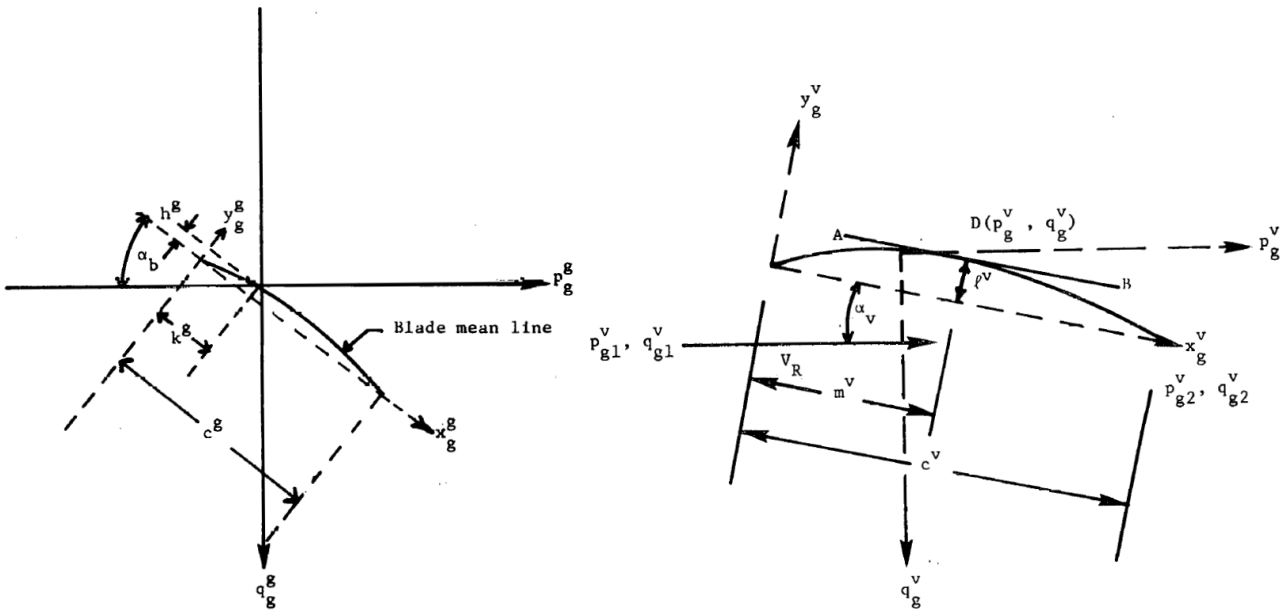

Figure 6.1: Coordinate system relations [30].

The transformed airfoil coordinates can be obtained by Equation 6.5 and Equation 6.6. Here, ε is the inverse of the tip speed ratio and θ is the blade azimuthal angle. The superscript g denotes the geometrical airfoil, and v the virtual one. While the subscripts g, v, and R denote which length has been used to non-dimensionalise, respectively the geometric chord c^g, the virtual chord c^v, and the VAWT radius R.

$$\gamma = \varepsilon \cos(\theta) \tag{6.1}$$

$$\lambda = 1 - \varepsilon \sin(\theta) \tag{6.2}$$

$$\Gamma = \frac{p_g^g}{R_g^g} + \gamma \tag{6.3}$$

$$\Lambda = \frac{q_g^g}{R_g} + \lambda \tag{6.4}$$

$$\frac{q_g^v}{R_g} = \left[\Gamma^2 + \Lambda^2\right]^{\frac{1}{2}} - \left[\gamma^2 + \lambda^2\right]^{\frac{1}{2}} \tag{6.5}$$

$$\frac{p_g^v}{R_g} = \left[\Gamma^2 + \Lambda^2\right]^{\frac{1}{2}} \cdot \left[\tan\left(\frac{\Gamma}{\Lambda}\right)^{-1} - \tan\left(\frac{\gamma}{\lambda}\right)^{-1}\right] \tag{6.6}$$

Afterwards, the virtual angle of attack and virtual chord length can be found according to Equation 6.7 and Equation 6.8, where 1 indicates the leading edge and 2 the trailing edge, as shown in Figure 6.1b. Finally, the virtual airfoil coordinates are calculated using Equation 6.9 and Equation 6.10.

$$\alpha_v = \tan\left(\frac{q^v_{g2} - q^v_{g1}}{p^v_{g2} - p^v_{g1}}\right)^{-1} \tag{6.7}$$

$$\frac{c^v}{c^g} = \left[\left(p^v_{g2} - p^v_{g1}\right)^2 + \left(q^v_{g2} - q^v_{g1}\right)^2\right]^{\frac{1}{2}} \tag{6.8}$$

$$x^v_v = \left[\left(p^v_g - p^v_{g1}\right)\cos\left(\alpha_v\right) + \left(q^v_g - q^v_{g1}\right)\sin\left(\alpha_v\right)\right]\frac{c^g}{c^v} \tag{6.9}$$

$$x^v_v = \left[\left(p^v_g - p^v_{g1}\right)\sin\left(\alpha_v\right) - \left(q^v_g - q^v_{g1}\right)\cos\left(\alpha_v\right)\right]\frac{c^g}{c^v} \tag{6.10}$$

6.1.2 Hirsch

Hirsch and Mandal [43] concluded that VAWTs with a high chord-to-radius ratio experience a continuous variation of angle of attack of the chord. They assume that an airfoil in this curvilinear flow is similar to a transformed airfoil in rectilinear flow. Their described method is categorised as a geometrical transformation. Based on the angle of attack at both the leading and trailing edge, induced by the rotation of the blade, a new camberline is proposed. The height of this circular arc can be computed using the provided equations, under that assumption thin airfoils are considered. The virtual incidence is added to the original angle of attack to obtain the aerodynamic coefficients.

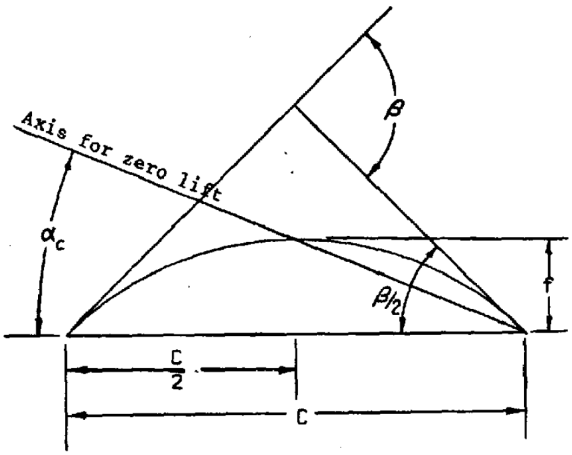

Figure 6.2: Definitions for the mean camber line transformation in Hirsch [43].

The height of the arc in Figure 6.2 is found according to Equation 6.12, which uses both the leading and trailing edge angles of attack of the original airfoil, as in Equation 6.11. The correction on the angle of attack by Equation 6.13.

$$\beta = \alpha_{TE} - \alpha_{LE} \tag{6.11}$$

$$\frac{2f}{c} = \frac{1 - \cos\left(\frac{\beta}{2}\right)}{\sin\left(\frac{\beta}{2}\right)} \tag{6.12}$$

$$\alpha_c = \tan\left(\frac{2f}{c}\right)^{-1} \tag{6.13}$$

The authors found the method to produce improved accuracy to a model which does not take into account flow curvature effects. The modified airfoil performed better, resulting in a closer approximation of experimental data.

6.1.3 Zervos

Zervos [7] observed that flow curvature results in an airfoil transformation, leading to a shift of airfoil sectional data. This results in an increase in force production in the upstroke and a decrease in the downstroke, partly due to the airfoil transformation and partly due to the increased wake of the upstroke. This leads to an undesired unsymmetrical force production over the rotation. Calculations showed that cambered airfoils mitigated these effects. Therefore, the author suggests a camber line transformation.

This geometrical transformation, is to use the circular arc swept by the VAWT blade as a camberline. To do so, the equation of the coordinates of a circle have been applied, as shown in Equation 6.14. The thickness of the original airfoil is preserved.

$$y = -R + \sqrt{R^2 - x^2} \tag{6.14}$$

Calculations performed by Zervos showed that this transformation resulted in a more beneficial force production. The author suggests that this will in the end have a diminishing effect on fatigue.

6.1.4 Gregory

Even a different geometrical mapping is employed by Gregory et al. [49]. The paper considers a body performing a steady turn with a constant radius. This is equated to a body with a camber line equal to the radius in rectilinear flow, what results in that the angle of attack in both situations is equal over the chord. The derivation of the corresponding equations is done according to Figure 6.3.

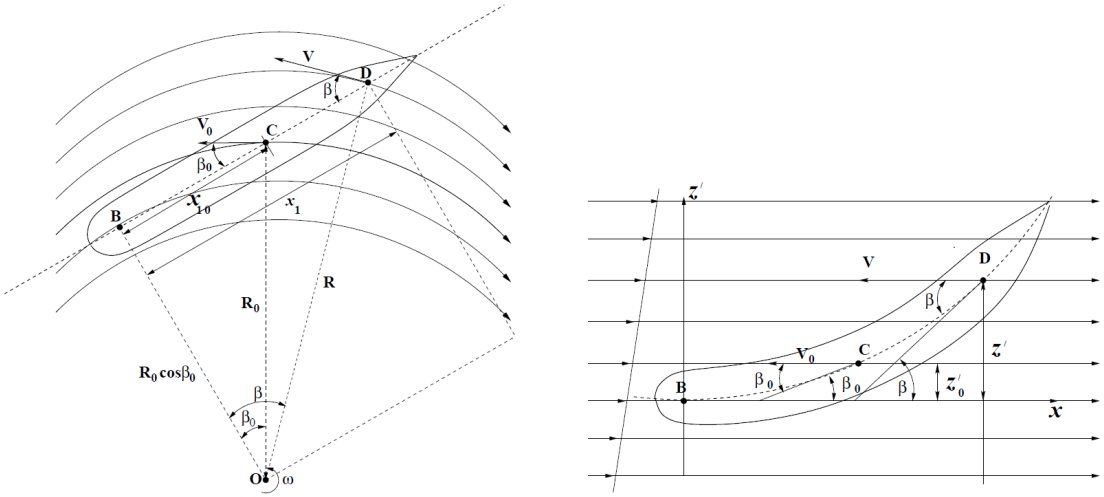

Figure 6.3: The transformation method described in Gregory [49].

From the figure, Equation 6.15 can be obtained to compute the distance from the leading edge to the centre of rotation. At any location on the mean camber line, the local angle of attack is defined by Equation 6.16 in the original coordinate system, and by Equation 6.17 in the transformed system. As mentioned, these should be equal. The mean camber line length should be preserved, which is achieved with Equation 6.18. Combining, rearranging, and differentiating results in Equation 6.19. The latter can be used to find the first-order linear differential Equation 6.20, which describes the curvature of the mean camber line of the transformed body.

$$\overline{OB} = R_0 \cos(\beta_0) \tag{6.15}$$

$$\tan(\beta) = \frac{\overline{BD}}{R_0 \cos(\beta_0)} = \frac{x_1}{R_0 \cos(\beta_0)} \tag{6.16}$$

$$\tan(\beta) = \frac{dz'}{dx} = \frac{x_1}{R_0 \cos(\beta_0)} \tag{6.17}$$

$$x_1 = \overline{BD} = \int_0^x \sqrt{1 + \left(\frac{dz'^2}{dx}\right)} dx \tag{6.18}$$

$$\frac{d^2 z'}{dx^2} = \frac{1}{R_0 \cos(\beta_0)} \sqrt{1 + \left(\frac{dz'^2}{dx}\right)} \tag{6.19}$$

$$z' = R_0 \cos(\beta_0) \left[\cosh\left(\frac{x}{R_0 \cos(\beta_0)}\right) - 1\right] \tag{6.20}$$

6.1.5 Akimoto

The second conformal mapping technique considered is the one applied by Akimoto et al. [50]. Conformal mapping means that a transformation is considered which takes into account the preservation of local angles. In this manner, the surface of the resulting airfoil shall be more accurately transformed. This transformation also applies flow similarity, taking in consideration the fluid dynamics around the original body must be consistent around the one around the new airfoil. To this extend, the following method is applied by the authors, on the airfoil shown in Figure 6.4.

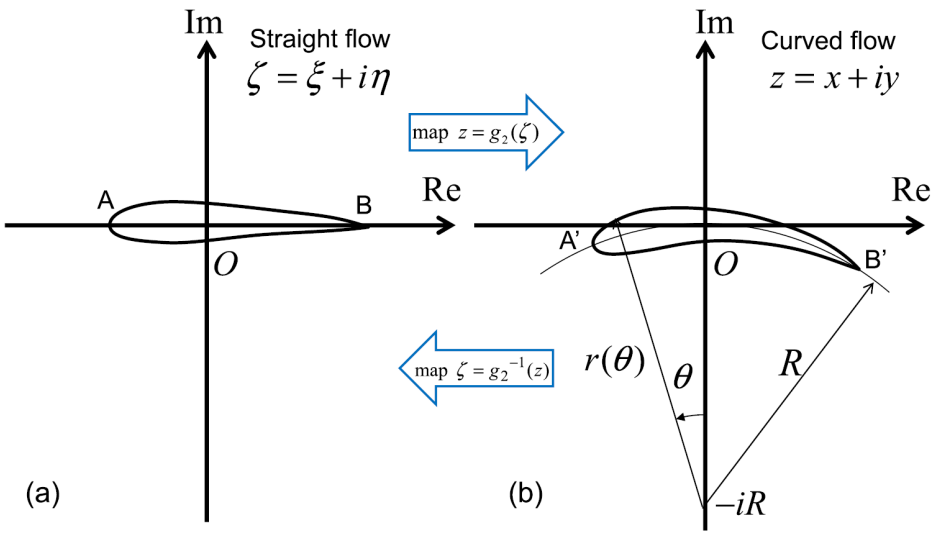

Figure 6.4: Definitions in the transformation method proposed by Akimoto [50].

The chord of the original airfoil is mapped into a circular arc by the mapping function in Equation 6.21. As the chord is mapped onto a circle, its length will slightly decrease and become $R\left[1 - \cos\left(\frac{c}{2R}\right)\right]$. This transformation is merely a geometrical one, and, as the authors mention, it is not a regular function (a function which is complex differentiable and single-valued at any point). This means that the velocity potential cannot be derived to obtain the velocity field. Therefore, to also transform the potential flow, the function is changed to Equation 6.22. The change in velocity on the surface, and thickness of the body is negligible using this method, and also the circulation on the airfoil remains the same. Lastly, to make sure the orientation of the airfoil is remained, one last modification is made and the final equation is Equation 6.23.

$$z = (R + \eta) e^{-\frac{i}{R}\xi} \tag{6.21}$$

$$z = R e^{-\frac{i}{R}\zeta} \tag{6.22}$$

$$z = iR e^{-\frac{i}{R}\zeta} - iR \tag{6.23}$$

6.1.6 e^z method

The last method applied is the e^z method. This method has not been found in any particular reference, but is thought to be applied in the past. A conformal transformation modifies the original airfoil based on the local radius of a coordinate. Figure 6.5 shows how a rectilinear grid is transformed to a curvilinear one, by the use of Equation 6.24. The same applies on the airfoil coordinates, resulting in a cambered profile.

$$f(z) = e^z \quad \text{with} \quad z = x + iy \tag{6.24}$$

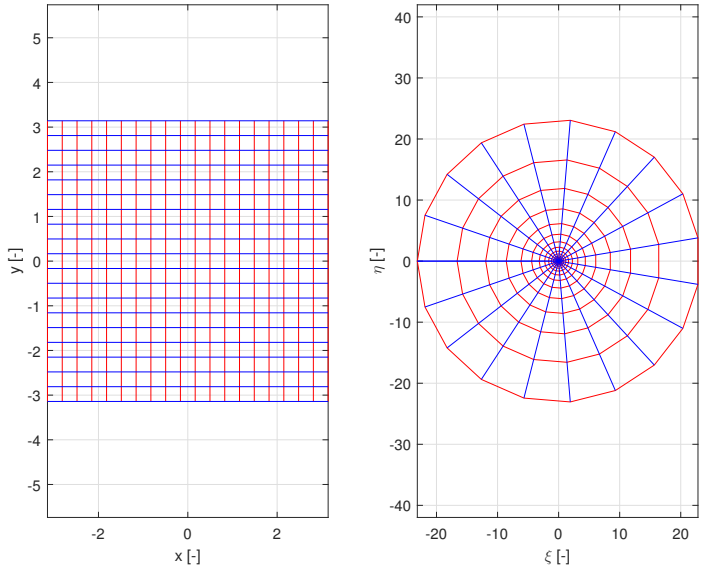

Figure 6.5: Conformal transformation using the e^z method.

6.2 Results

The above-mentioned transformations have been applied in several analyses to assess their behaviour. First, a visual inspection will show how the methods differ and a discussion on the resulting geometries will be presented. Afterwards, for the virtual airfoils a pressure distribution will be shown. These shall be calculated using the U2DIVA panel code, in steady flow. The results will be compared to the outcomes of the U2DIVA panel code computing the quasi-steady, pitching solution. Also, a viscous comparison is made using the modified version of XFOIL, to be explained in chapter 7. Finally, to objectively measure the performance of the methods, an error with respect to the pitching solution is to be computed.

6.2.1 Geometry

The variation of geometry will be discussed by the influence the three free variable have. Respectively, the effect of changing the chord-to-radius ratio, the mounting location, and the angle of attack will be investigated.

Chord-To-Radius Ratio

Figure 6.6 and Figure 6.7 show the resulting airfoils when the transformations are applied on a NACA0015 profile, respectively for a chord-to-radius ratio of 0.2 and 1. The airfoil mounting location, which is a variable for most transformations is at a quarter of the original chord length, and the original airfoil was at an angle of attack of zero degrees. The airfoils are grouped into the geometrical transformations in the upper plot, and the conformal ones in the lower.

All methods produce a slightly cambered airfoil. The added virtual incidence angle is not shown in this plot, as the airfoils are all rotated back to make the comparison easier. As one can see, for a high ratio of 0.2[1], the resulting airfoils are very similar and their deviation from the original airfoil is not drastic. This means that flow curvature effects for more regular, lower chord-to-radius ratios will be even smaller. For an exaggerated ratio of 1 the results do differ a lot, but one would never find a turbine with such a high value in practice. Though, these outcomes can serve as a way to identify differences between the models.

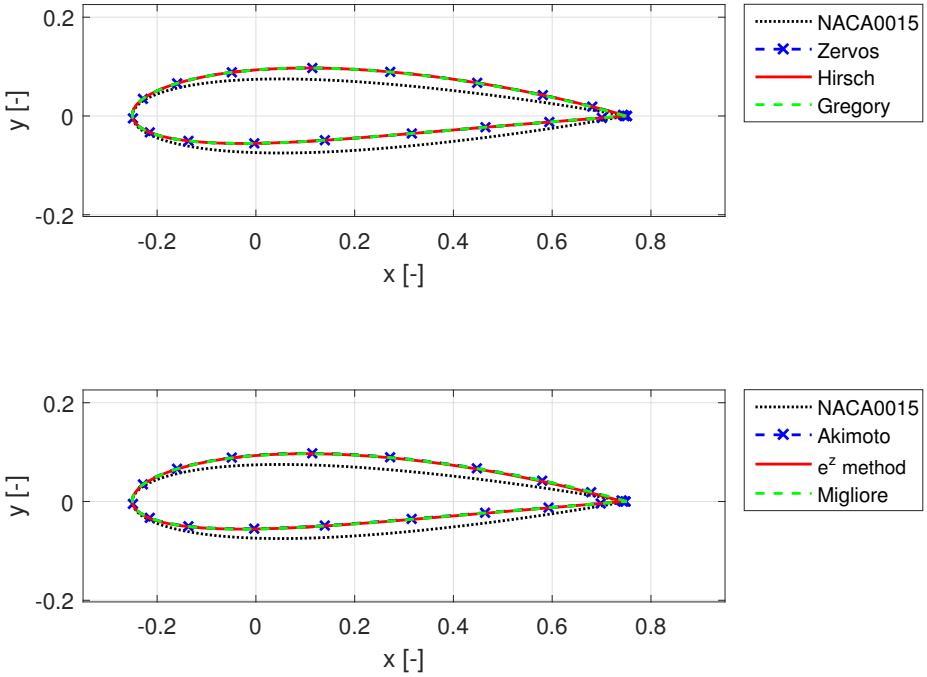

Figure 6.6: Virtual airfoil transformations for a chord-to-radius ratio of 0.2, and a mounting location at the quarter chord position..

As can be seen, the methods of Zervos and Hirsch are fairly similar, these methods rely on transforming the mean camberline into a circular arc. The only geometrical method which is different is the one from Gregory. The latter shows a chord decrease compared to the original, resulting in a more curved aft part of the airfoil. On the other hand, the conformal methods perform quite varying. Whereas Akimoto's and Migliore's methods act more gradually, the e^z method is quite drastic. Here, the length of the camberline is equal to the original chord length, resulting in a large decrease of the virtual chord. This leads to that the airfoil is not as slender as its counterparts.

[1] It will be shown in chapter 8 that a chord-to-radius ratio of 0.2 is a high value and commonly not found in practice.

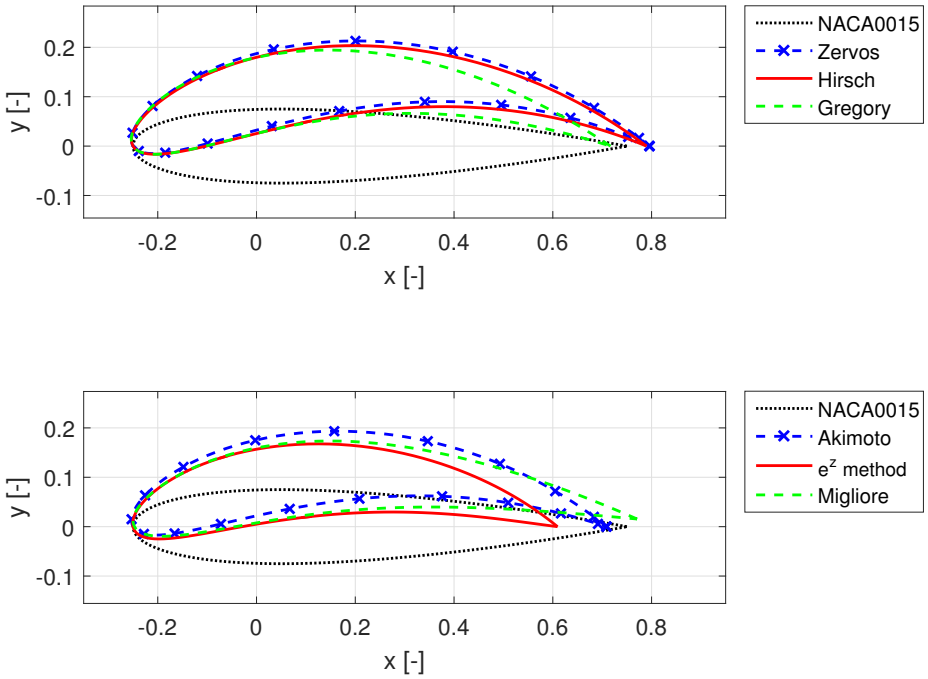

Figure 6.7: Virtual airfoil transformations for a chord-to-radius ratio of 1, and a mounting location at the quarter chord position.

Camber, Chord, and Incidence The differences between methods for a chord-to-radius ratio of 0.2 are shown in Table 6.1. It can be seen that the variation is very small, and in this situation the methods perform very similar. The maximum camber is the same for each method. One can see that the three geometrical methods (Hirsch, Zervos, and Gregory) are almost identical. This shows that for regular values for the $\frac{c}{R}$ ratio, it is difficult to distinguish differences between the models.

Table 6.1: Virtual airfoil parameters computed by the different methods, for a chord-to-radius ratio of 0.2 and a mounting location at a quarter chord.

	Migliore	**Hirsch**	**Zervos**	**Gregory**	**Akimoto**	**e^z method**
Chord [-]	1.004	1.001	1.001	0.998	0.998	0.993
Camber [-]	0.025	0.025	0.025	0.025	0.025	0.025
Position maximum camber [-]	0.493	0.504	0.504	0.504	0.495	0.497
Angle of incidence [deg]	2.837	2.873	2.880	2.877	2.865	2.834

To quantify the differences between the transformations better, the virtual camber, chord, and angle of incidence have been computed for the same profile and parameters, for a varying chord-to-radius ratio. The results in Figure 6.8a, Figure 6.8c, and Figure 6.8b show that for a ratio of up to 0.4 the virtual airfoils are quite similar, differing only in chord length. Thereafter, the results diverge. Again it must be stressed that in reality, a ratio of higher than 0.2 is very uncommon.

The virtual camber, indicated with the symbol for curvature κ_v, shows an increasing manner with increasing ratio in Figure 6.8a. This is to be expected as increasing the chord-to-radius ratio will increase the angle of attack variation along the chord. When the virtual transformation accounts for this level of flow curvature, a more cambered virtual airfoil will be obtained. Of all methods, the three geometrical transformation show the most similarity.

As for the angle of incidence obtained by the transformation, the geometrical transformations again are fairly similar, while the rest shows differing results. It must be noted here that the angle of incidence is not only dependent on the chord-to-radius ratio, but also on the mounting location of the airfoil. Namely, this location determines the amount and location of the camber. Placing the mounting axis more forward will result in an increased incidence angle, while using the half-chord location, the camber would be symmetrical and no virtual incidence would be obtained. One can intuitively determine this by looking at the rotational induced normal velocities of a flat plate, which will be symmetrical, so no net sum of virtual incidence angle will be obtained. Benedict et al. [16] confirm this.

For the transformed chord length however, the methods vary significantly, as seen in Figure 6.8c. The transformed length is normalised as the original airfoil has a chord length of 1. As seen before, the e^z method shows a large decrease in length. Furthermore, Hirsch and Zervos again show similarity.

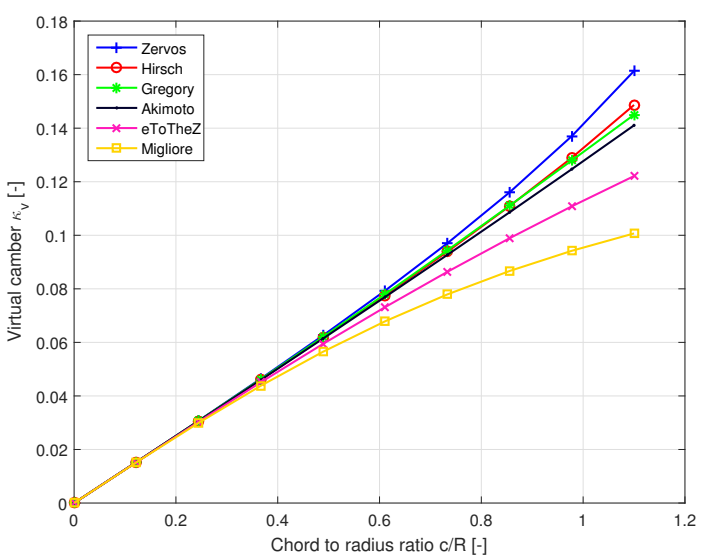

(a) Virtual camber.

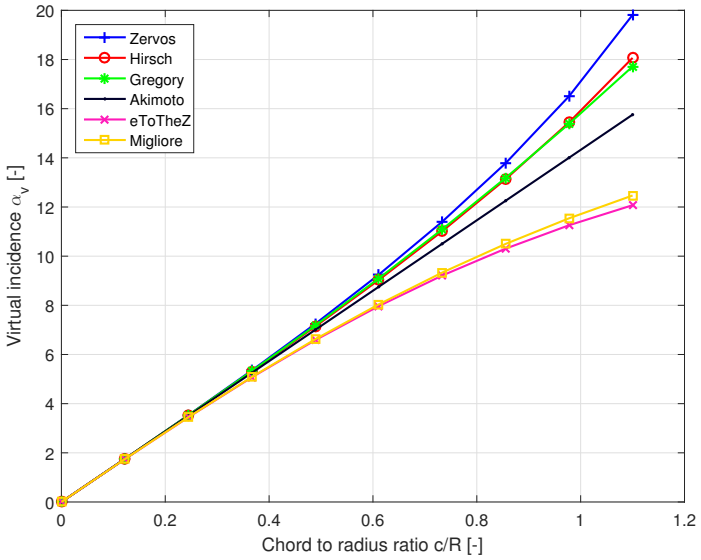

(b) Virtual incidence.

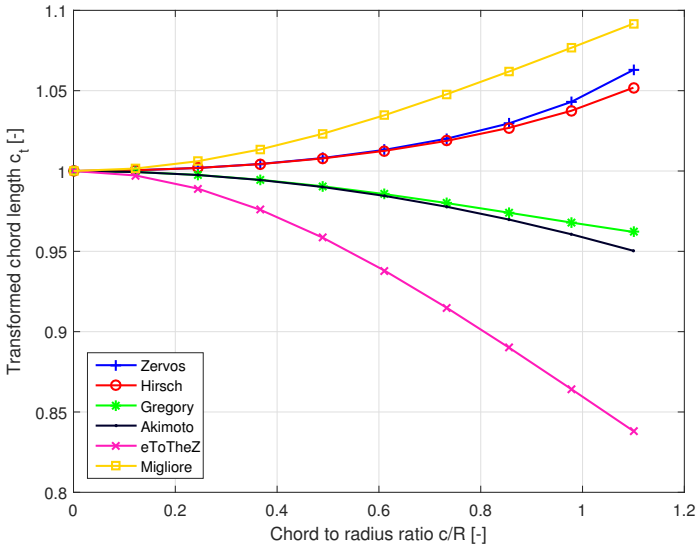

(c) Transformed chord length.

Figure 6.8: Variation of virtual airfoil characteristics for varying chord-to-radius ratios.

Mounting Location

When varying the mounting location, very different results are obtained. Expected is that the camber and its position will vary due to the transformation, as well as the maximum thickness and its location. However, for each method these variables change differently. The results are indistinguishable for a lower chord-to-radius ratio, again indicating that in practice the methods are exchangeable. Therefore, an exaggerated value of 1 is used to spot any differences.

In Figure 6.9a, for the Migliore method the maximum camber, indicated with the marker, moves aft and increases. The maximum thickness moves aft, but remains the same and the chord length decreases. However, for the e^z method, the camber moves forward and increases, the maximum thickness moves forward, and the chord length increases. The rest of the methods also show no trend for any of the variables.

Therefore, Table 6.2 shows what the effect of moving the mounting location aft has on the virtual airfoils geometrical parameters. For each of the method, an increase of a parameter is indicated with a (+), a decrease with (−), and no change with (=). The maximum thickness position and chord length behave the most similar for all methods except Akimoto and the e^z method.

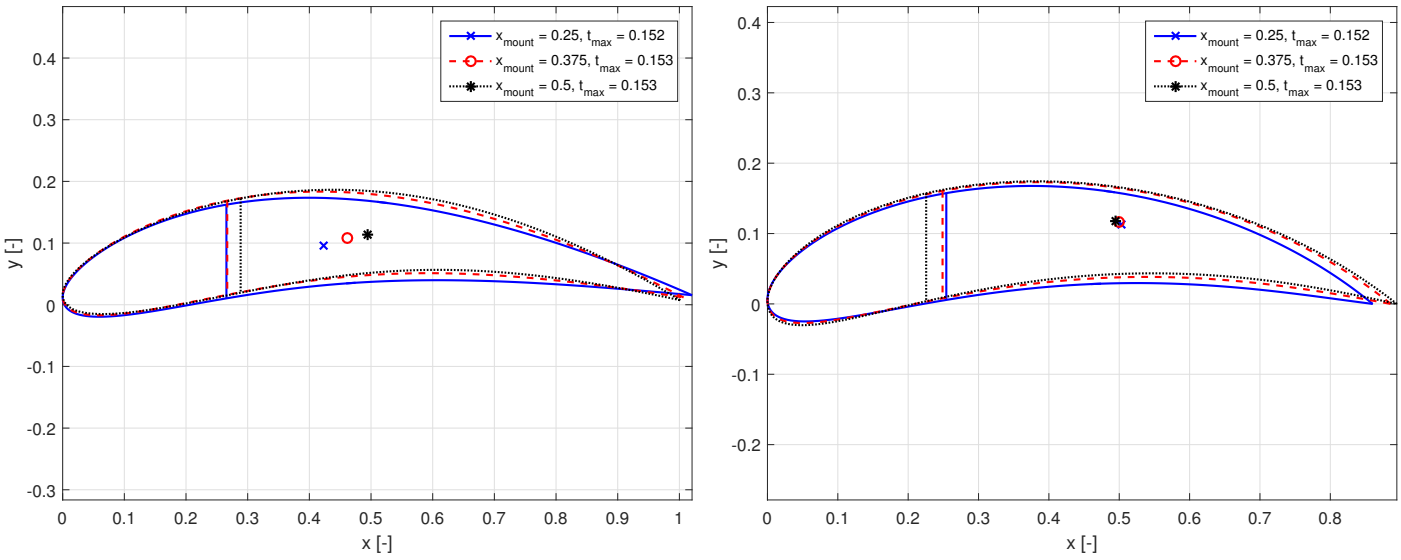

(a) Migliore method.

(b) e^z method.

Figure 6.9: Variation of geometrical parameters as a result of an aft moving mounting location, with a chord-to-radius ratio of 1 and an angle of attack of 0 degrees.

Table 6.2: Variation of geometrical parameters as results of a change in mounting location.

	Migliore	Hirsch	Zervos	Gregory	Akimoto	e^z
Maximum camber [-]	+	+	-	+	=	+
Maximum camber position [-]	+	-	-	+	-	-
Maximum thickness [-]	+	-	-	-	=	+
Maximum thickness position [-]	+	+	+	+	=	-
Chord length [-]	-	-	-	-	=	+

Angle of Attack

Only the Gregory transformation is dependent on the angle of attack of the to be transformed airfoil. As can be seen in Figure 6.3, the angle between the body and the flow determines the variation of angle of attack over the body. The method therefore includes the angle of attack β_0 in its equations. However, a quick study of its influence showed that its impact is negligible. One could also have seen that from Equation 6.20, where the cosine of the small angle can be approximated with 1.

6.2.2 Inviscid Pressure Distribution

For the same two cases displayed above, the pressure distribution has been computed with the U2DIVA code, where the mounting location is on a quarter of the chord. As the transformations influence the chord length of an airfoil, the resulting airfoils are normalised before further analysis is done. Normalisation is valid as the pressure coefficient is dimensionless. The pitching solution computed by the U2DIVA panel code is marked in the legend as the quasi-steady solution.

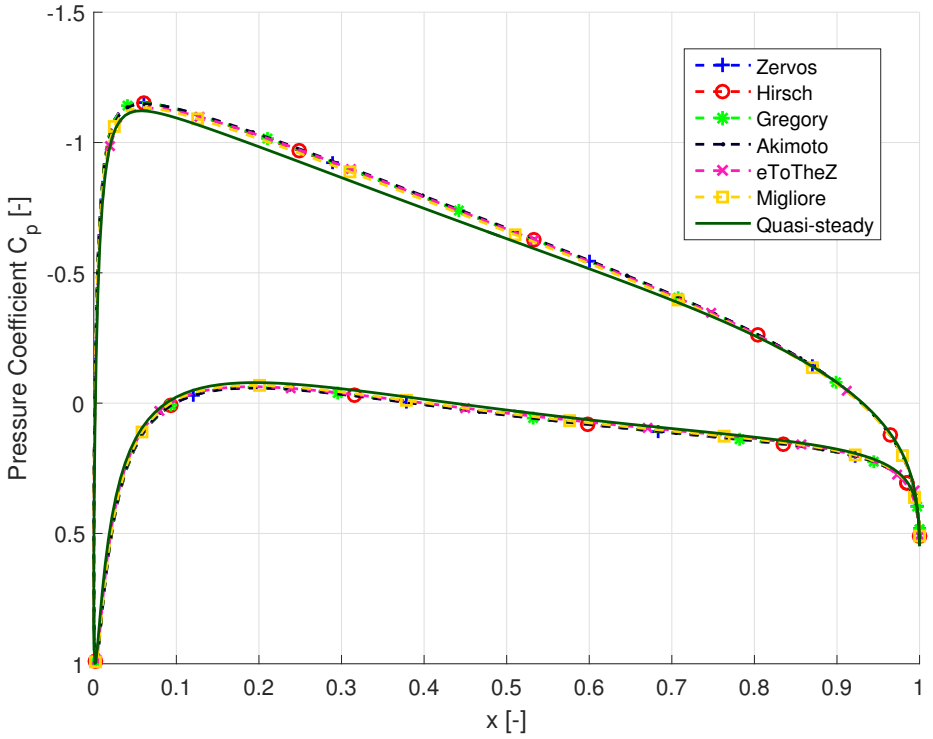

Figure 6.10: Pressure distributions for a chord-to-radius ratio of 0.2, and a mounting location at a quarter-chord length.

As can be seen in Figure 6.10, for the lower chord-to-radius ratio, the results are marginally different from each other. Also, they approximate the quasi-steady solution reasonably well. As lower chord-to-radius ratios are more common, it is expected that neither method will perform any better than another and that the difference with the quasi-steady solution will decrease.

These distributions are computed for a regular mounting location between a quarter and half of the chord. In the unlikely case that a location beyond these bounds is chosen, the distributions show more differences. This investigation should be performed when required, and shall not be performed here.

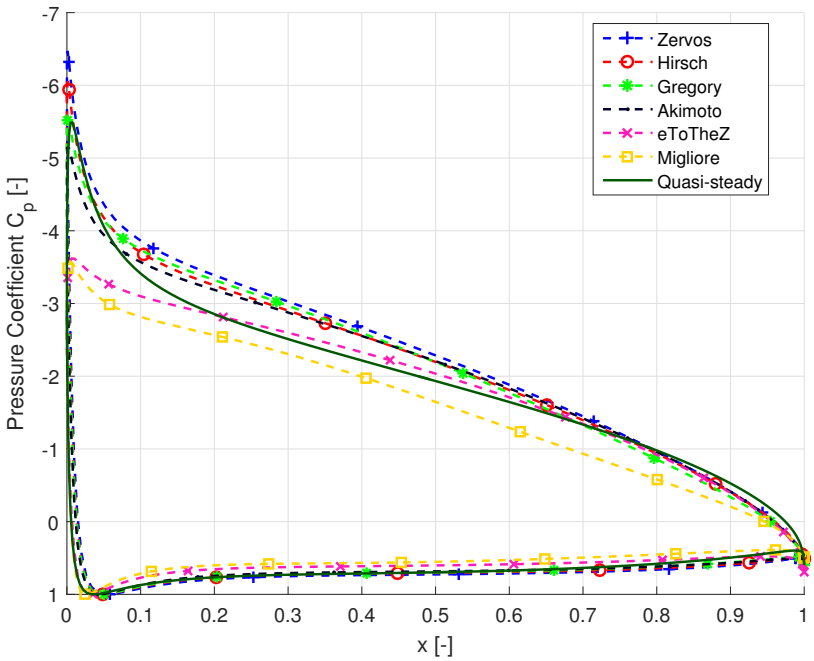

Figure 6.11: Pressure distributions for a chord-to-radius ratio of 0.8, and a mounting location at the quarter-chord location. For legibility reasons the legend is omitted, but is the same as in Figure 6.10.

As shown, for common situations the methods perform equally well. However, to illustrate the differences between the method, a chord-to-radius ratio of 0.8 is also applied. The results are shown in Figure 6.7. The Zervos and Hirsch methods produces such a thin trailing edge of the virtual airfoil at a higher ratio, that the panel code could not cope with its surface, as mentioned this has to do with numerical errors due to the close proximity of the panels to each other. Therefore, a slightly lower, but still uncommonly high ratio is chosen to depict the differences.

It can be seen that the pressure side of the distribution is captured well, indicating that the flow over the lower surface of the virtual airfoils is comparable to the quasi-steady situation. However, on the suction side large discrepancies are obtained. The leading edge suction peak is only captured well enough by Gregory's method, while the rest do only slightly worse, except for Migliore and the e^z method. The latter two show a large mismatch of surface velocities near the leading edge. The trailing edge also poses problems, as no method seems to facilitate the lower pressure computed for the quasi-steady model. Furthermore, the only method which resembles the rest of the upper airfoil surface is the e^z method. This could be ascribed to its lower virtual camber and angle of incidence. Migliore and this method have the lowest camber and incidence, as seen in Figure 6.8. The leads to a lower surface velocity on the suction side of the airfoil, and therefore a higher pressure than the other methods.

6.2.3 Viscous Pressure Distribution

A viscous comparison is made with the modified version of XFOIL. The theory and modification of this software shall be reserved for chapter 7. The software is able to compute the viscous pressure distribution in both steady and pitching cases, which now will serve to compare the virtual airfoil models against the quasi-steady solution. It must be mentioned that as no comparison methods were available for the viscous pitching solution, the viscous XFOIL implementation has not been verified. This analysis will serve the purpose a preliminary comparison to the XFOIL solution, but mostly between the methods.

The same analysis as above is done for all the virtual airfoils. The Reynolds number and mounting location is varied to see their effects. The results are shown in Figure 6.12, where again a high chord-to-radius ratio of 0.2 is applied to show the most drastic effects. For lower ratios, the differences are confirmed to decrease.

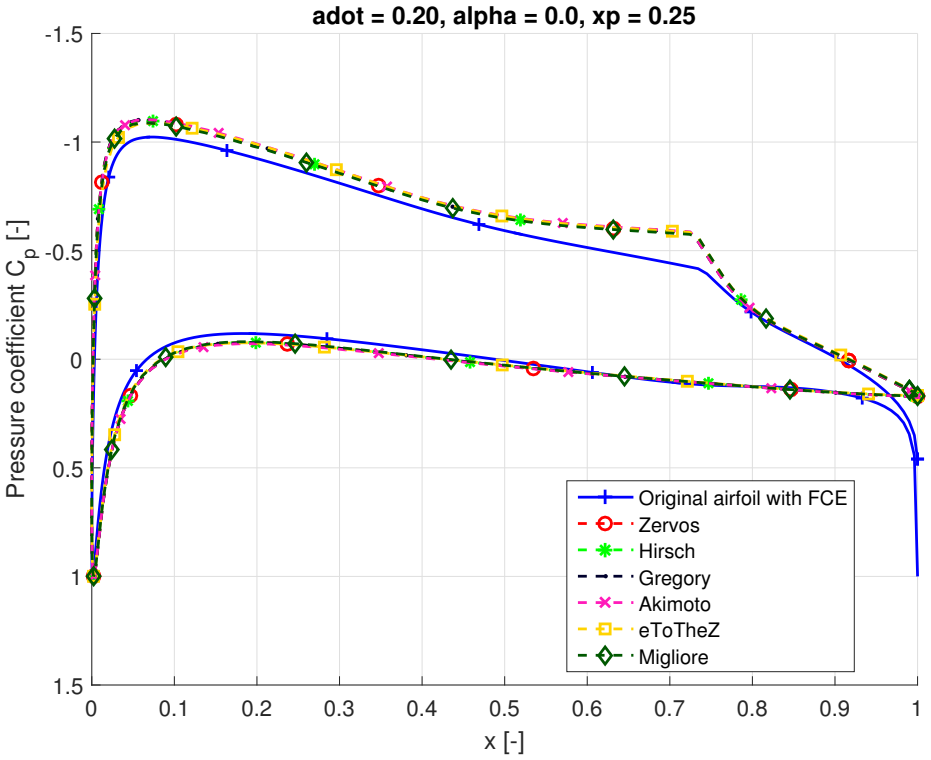

Figure 6.12: Viscous pressure distributions for the virtual airfoils and the pitching solution, with an angle of attack of 0 degrees, a pitching rate of 0.2, mounting location of $0.25c$, and a Reynolds number of 10^5.

The figure shows the existence of a laminar separation bubble on the suction side of the airfoil, which is typical for a Reynolds number of 10^5. As can be seen, the bubble is larger and longer for the virtual airfoils, and also the trailing edge does not comply very well. The other differences are also visible in the inviscid solution, so are not discussed again. The larger bubble indicates that either the virtual airfoils have an upper surface which results in a too steep pressure gradient, resulting in local separation and reattachment of the flow. Or the rotation of the airfoil results in decreased surface velocities of the pitching solution. As the viscous solution has not been verified, no conclusions can be drawn. As also can be seen, all transformation methods show a very similar behaviour, and again are interchangeable.

What can be said however, is that the comparison enhances with increasing Reynolds number or angle of attack. As the former shows an increased importance of inertial forces over viscous ones, and the latter results in an increase of surface speeds, the laminar separation bubble tends to diminish. This is shown in Figure 6.13a and Figure 6.13b respectively. The solutions for the virtual airfoils also improve with respect to the pitching solution.

When the mounting location is changed to half the chord in Figure 6.13c, the viscous differences do not change. However, the virtual airfoil's geometries have changed as such that there is now a laminar separation bubble on the other surface as well. Again, there is an overestimation of its magnitude by the transformation methods, but overall, the approximation to the bubble computed by the pitching solution is well.

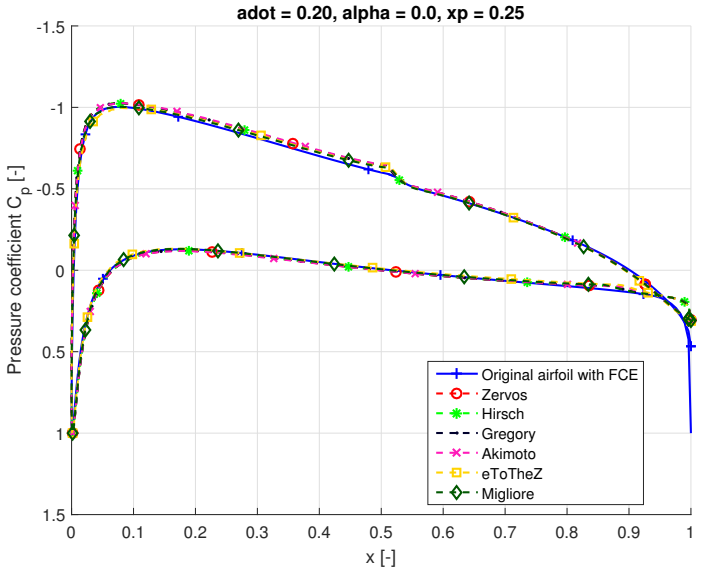

(a) Angle of attack of 0 degrees, Reynolds number of 10^6, mounting location at $0.25c$.

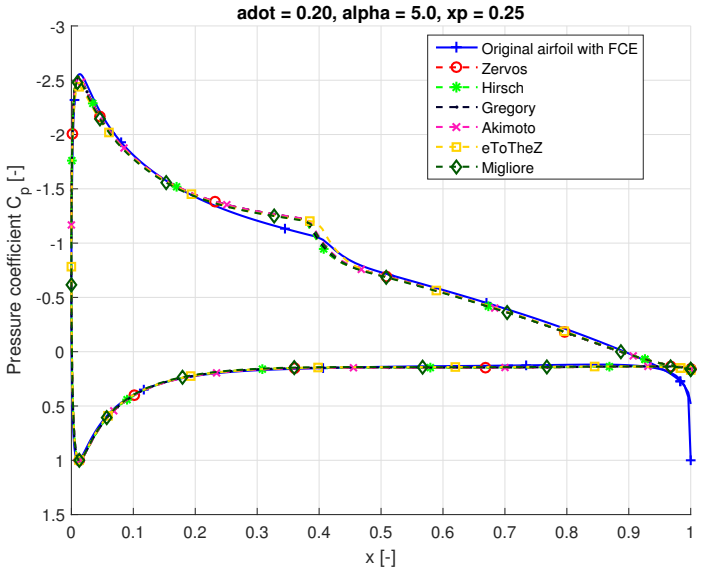

(b) Angle of attack of 5 degrees, Reynolds number of 10^5, mounting location at $0.25c$.

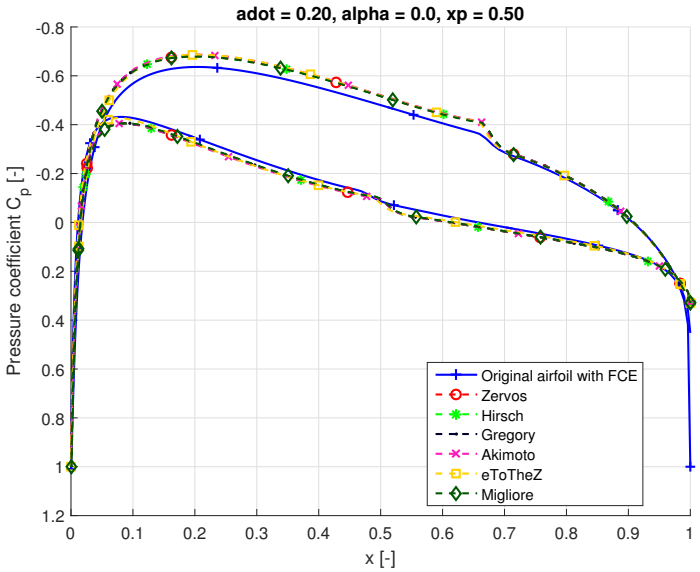

(c) Angle of attack of 0 degrees, Reynolds number of 10^6, mounting location at $0.5c$.

Figure 6.13: Viscous pressure distributions for the virtual airfoils and the pitching solution, with a pitching rate of 0.2.

6.2.4 Error measure

As mentioned before, when varying the chord-to-radius ratio, mounting location, and angle of attack to their extremes, differences start to show. However these are very dependent on the situation, and an appropriate method should be chosen accordingly. Still, an analysis is performed to objectively measure the difference between the quasi-steady solution computed by the U2DIVA panel code and its solution for the virtual airfoils in varying situations. This is done only for the inviscid solutions, as this shows the behaviour of the methods sufficiently enough.

The sum of the absolute difference between the pressure distributions is taken. This of course does not tell the shape of the resulting distributions and might provide a false results, as some solutions might compare very well for the most part of the surface but have a large error at say the leading edge. However, it is unreasonable to analyse all cases visually, so this at least gives some indication.

Only reasonable values for the parameters are chosen. The chord-to-radius ratio is varied from 0 to 0.2 with steps of 0.05, the angle of attack of the original airfoil from -10 to 10 with steps of 5, and the mounting location from 0.25 to 0.75 with steps of 0.125. For these 125 simulations run for each calculated virtual airfoil and the pitching solution of the original airfoil, the results are as follows.

- For the first three mounting locations [0.25 0.375 0.5], the conformal Migliore method performs best in nearly all cases.
- For a location on 0.675 of the chord the Hirsch method performs better in most cases.
- And for the very last mounting location the three geometrical transformations have the upper hand (Hirsch, Zervos, and Gregory).

It must be emphasised that for the range of these parameters all pressure distributions are really close together. Outside these bounds, where the variables have an uncommon value, this analysis has to be redone to evaluate the best suitable method.

6.3 Chapter Conclusions

- In the past several authors have created different models to investigate flow curvature. These all are based on a virtual airfoil transformation, although the methods are quite diverse. Each of them are based on different principles and either apply a geometrical or conformal transformation. The latter accounts for the preservation of local angles.
- The resulting airfoils are dependent on the chord-to-radius ratio and the mounting location. For regular ratios below 0.2, the difference are indistinguishable in both the produced geometries and pressure distributions. The inviscid pressure distribution only marginally differs from the U2DIVA panel code solution. After a ratio of 0.4 the methods diverge, leading to varying virtual camber, virtual incidence, and transformed chord length. Their accuracy with respect to the U2DIVA panel code also diverged. As these chord-to-radius ratios are very uncommon, a tailored analysis is recommended where necessary.
- The viscous solutions showed a large difference between the virtual airfoil methods and XFOIL. Changing the Reynolds number or angle of attack of the airfoil an improvement of the comparison is obtained. Moving the mounting location does not influence the discrepancy. It must be noted that the viscous XFOIL solution is not verified, so could also computed erroneous pressure distributions.
- Varying the mounting location proved of varying influence, stressing the need for a tailored analysis when this variable is varied outside its regular bounds.
- Finally it can be concluded that when the free variables of the methods are kept within their common and feasible bounds, the methods vary so little that they are exchangeable. Also their difficulty of implementation is so low that either method can be used.

Chapter 7

XFOIL

With the use of a potential flow panel method, airfoil analysis is made fast and efficient. Also, the most recent software packages have proven to provide accurate solutions. One of the most used programs, and also the main topic of this thesis research, is the XFOIL system. As its source code and theoretical background is publicly available, it provides the perfect opportunity to implement the modelling of flow curvature.

This chapter will concern the implementation of flow curvature effects in XFOIL. First, a brief introduction into the software will be presented, investigating the available tools and functionalities of the software, and the foundations and fundamental theory of the algorithm. Afterwards, a derivation of a model will be presented, which can be used to simulate an airfoil undergoing a VAWT rotation. Then, the method of application in the algorithm is discussed. Here a detailed explanation of the (altered) code and functions is given. Finally, it will be shown how the altered XFOIL can be put into use and the results it produces.

7.1 The XFOIL Code

One of the most well-known and proven aerodynamic airfoil tools is XFOIL. This code was presented in 1986 and was developed at MIT by Drela [8]. The software provides user friendly analysis tools for subsonic airfoils, in both inviscid as viscous conditions. Its routines are nicely depicted in Figure 7.1. After an airfoil has been set, and if necessary geometrically edited, the flow solver can be used to compute airfoil characteristics. These can include aerodynamic polars, boundary layer characteristics, and the pressure distribution. It also allows for (partial-) inverse airfoil design where a desired pressure distribution is an input. This solver then iterates until it converges on an airfoil surface.

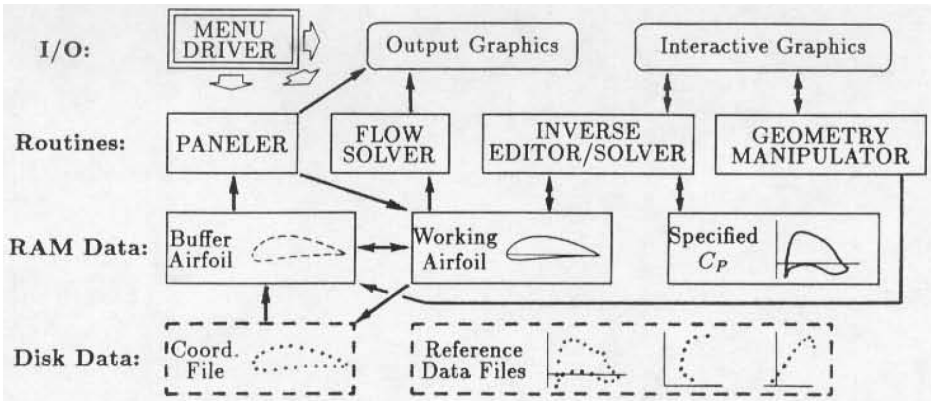

Figure 7.1: A block-scheme depicting the functionalities of the XFOIL software [8].

This thesis will focus on the direct solver only, to obtain inviscid and viscous solutions of an airfoil. The goal is to implement the modified code in an airfoil optimisation tool. The mentioned Optiflow optimiser will take beforehand generated airfoils and compute their characteristics. As a desired pressure distribution is not known beforehand, the inverse solver can not be used to find an optimal shape.

7.1.1 Inviscid Formulation

The two-dimensional panel code is based on a linear-vorticity streamfunction. By superimposing on the freestream both a vortex sheet γ, on the airfoil surface, and a source sheet σ, on the surface and in the wake, the flow field can be constructed according to Equation 7.4. This is shown in Figure 7.2.

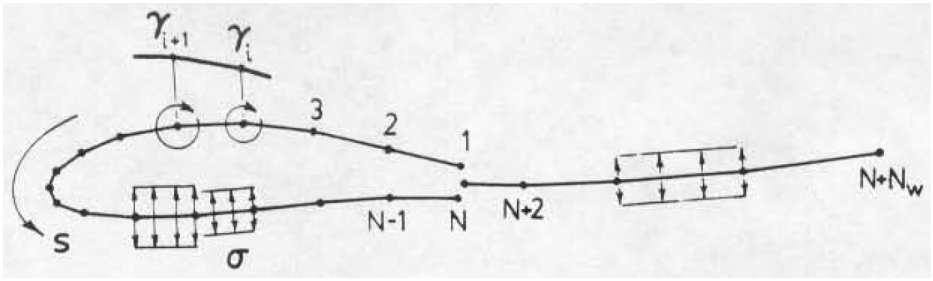

Figure 7.2: Singularity distribution definitions on the airfoil surface and its wake.

The streamfunctions for the freestream, point vortex, and point source can be retrieved from Katz and Plotkin [52] and are shown below. Combined, this results in Equation 7.4.

$$\Psi_\infty = uy - vx \tag{7.1}$$

$$\Psi_\gamma = \frac{\Gamma}{2\pi} \ln r \tag{7.2}$$

$$\Psi_\sigma = \frac{\sigma}{2\pi} \theta \tag{7.3}$$

$$\Psi(x,y) = u_\infty y - v_\infty x + \frac{1}{2\pi} \int \gamma(s) \ln\left(r(s;x,y)\right)\, ds + \frac{1}{2\pi} \int \sigma(s)\, \theta(s;x,y)\, ds \tag{7.4}$$

Here, u_∞ and v_∞ are the horizontal and vertical freestream components, s is the coordinate along the vortex and source sheets, r is the magnitude of the vector from the surface to a field point (x,y), and θ its corresponding angle, as depicted in Figure 7.3. A linear vorticity and constant source distribution are used.

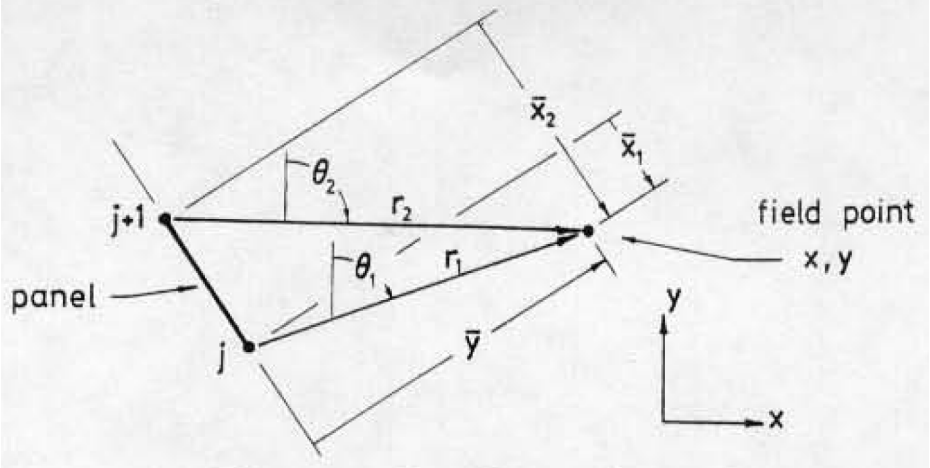

Figure 7.3: Local panel coordinates [8].

By applying this streamfunction on each panel, a linear system of equations can be set up, as shown in Equation 7.5. Here, the local streamfunctions fill the coefficient matrices a and b and are set equal to some constant value Ψ_0, dependent on the freestream. This is done for the panel and wake nodes, x and y. Combined with an additional equation to enforce the Kutta condition (Equation 7.6) at the trailing edge, these equations can be solved using Gaussian elimination.

$$\sum_{j=1}^{N} a_{ij}\gamma_{ij} - \Psi_0 = -u_\infty y_i + v_\infty x_i - \sum_{j=1}^{N+N_w-1} b_{ij}\sigma_j \quad ;\ 1 \leq i \leq N \tag{7.5}$$

$$\gamma_1 + \gamma_N = 0 \tag{7.6}$$

This method is applied for two cases, where the airfoil is either at an angle of attack of 0 or at 90 degrees. For a specific angle of attack, now these vectors are used to compute the surface vorticity. Multiplied by the cosine and sine of the angle respectively, the two vectors are added, as seen in Equation 7.7. By setting the source distribution to zero, an inviscid solution is immediately obtained.

$$\gamma_i = \gamma_{0_i}\cos(\alpha) + \gamma_{90_i}\sin(\alpha) + \sum_{j=1}^{N+N_w-1} b'_{ij}\sigma_j \quad ;\ 1 \leq i \leq N \tag{7.7}$$

The pressure distribution can be obtained from the vorticity distribution with the steady Bernoulli equation. As the flow is inviscid, and the impermeability condition enforces zero normal flow, the vorticity is equal to the tangential velocity when the airfoil and flow are steady. Therefore, the pressure is found according to Equation 7.8. Drela [8] shows that with increasing panel density, the solution becomes more than sufficiently accurate.

$$C_p = 1 - \left(\frac{\gamma}{q_\infty}\right)^2 \tag{7.8}$$

7.1.2 Viscous Formulation

Viscous analysis is performed based on two fundamental equations, the standard compressible integral momentum and kinetic energy shape parameter equations, respectively Equation 7.9 and Equation 7.10. Coupling with the inviscid solution takes place using the wall transpiration concept, which states that "the local source strength is equal to the local gradient of the mass defect" [8].

$$\frac{d\theta}{d\xi} + \left(2 + H - M_e^2\right) \frac{\theta}{u_e} \frac{du_e}{d\xi} = \frac{C_f}{2} \tag{7.9}$$

$$\theta \frac{dH^*}{d\xi} + \left(2H^{**} + H^*(1-H)\right) \frac{\theta}{u_e} \frac{du_e}{d\xi} = 2C_D - H^* \frac{C_f}{2} \tag{7.10}$$

The way to solve this non-linear system of equations is by using a full Newton's method. The principle is that based on the derivative of a function, at the evaluation point, a new approximation of the roots of that function can be found. When iterating, this approximation will tend to the exact solution. This method is performed using a sparse Jacobian matrix and predetermined Newton variables, in XFOIL's custom solver [8].

7.2 Pitching Similarity

This section will show that the motion of a blade undergoing a VAWT rotation can be kinematically equal to that blade pitching in straight flow. This similarity can then be used to correctly model a pitching airfoil in XFOIL. This allows flow curvature effects to be investigated by simulating such a motion.

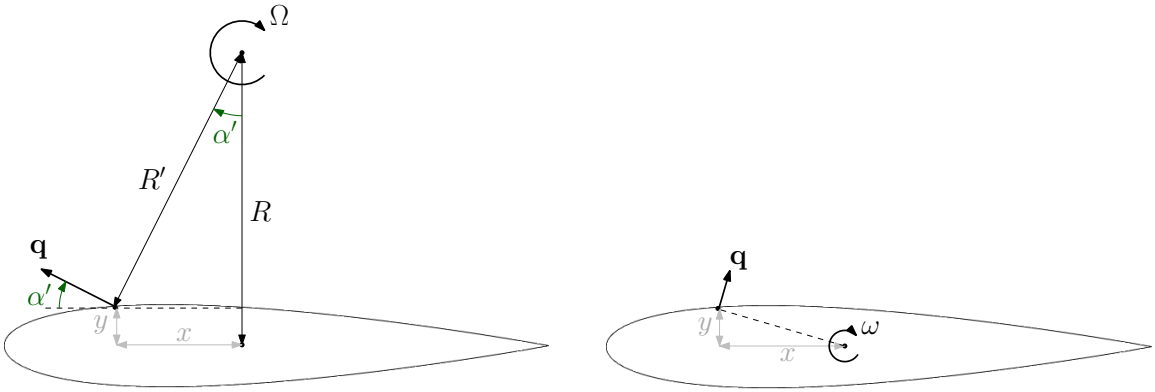

Figure 7.4: Pitching similarity.

In the left figure of Figure 7.4, the kinematics of an airfoil undergoing a rotation around an offset centre is visible. The rotation is performed in absence of a freestream. Here, Ω is the VAWT rotational velocity, R is the VAWT arm, R' is the local arm, α' is the local angle of attack of the rotation induced velocity at the surface coordinates x and y. The surface velocity $\boldsymbol{q}$ is comprised of its horizontal and vertical components u and v, which can be found using Equation 7.11 and Equation 7.12.

$$u = \cos\left(\alpha'\right) \Omega R' = \frac{R-y}{R'} \Omega R' = \Omega(R-y) \tag{7.11}$$

$$v = \sin\left(\alpha'\right) \Omega R' = \frac{x}{R'} \Omega R' = \Omega x \tag{7.12}$$

$$\boldsymbol{q} = \begin{pmatrix} u \\ v \end{pmatrix} = \begin{pmatrix} \Omega(R-y) \\ \Omega x \end{pmatrix} = \Omega R \begin{pmatrix} 1 \\ 0 \end{pmatrix} + \Omega \begin{pmatrix} -y \\ x \end{pmatrix} \tag{7.13}$$

In the situation of a pitching airfoil, the same can be derived for a pitching velocity ω, resulting in a surface velocity as shown in Equation 7.16. For both motions to have similar kinematics, the freestream velocity u_∞ must be equal to ΩR, which results in that the pitching velocity in both rotations is equal. This proves that an airfoil in VAWT rotation, without freestream, can be modelled by an continuously pitching airfoil in straight flow.

$$u = u_\infty - \omega y \tag{7.14}$$

$$v = \omega x \tag{7.15}$$

$$\boldsymbol{q} = \begin{pmatrix} u \\ v \end{pmatrix} = \begin{pmatrix} u_\infty - \omega y \\ \omega x \end{pmatrix} = u_\infty \begin{pmatrix} 1 \\ 0 \end{pmatrix} + \omega \begin{pmatrix} -y \\ x \end{pmatrix} \tag{7.16}$$

As has been shown before (subsection 3.2.2), flow curvature effects are dependent on the chord-to-radius ratio. In order to investigate its influence, a relation needs to be found to the pitching airfoil model. This can be achieved by simply rearranging the equations, as shown in Equation 7.17 to Equation 7.19.

$$\omega R = u_\infty \tag{7.17}$$

$$\frac{1}{R} = \frac{\omega}{u_\infty} \tag{7.18}$$

$$\frac{c}{R} = \frac{\omega c}{u_\infty} \tag{7.19}$$

Now the last equation is key to perform simulations. It makes it possible to simulate different chord-to-radius ratios by changing the normalised rotational velocity. Therefore the extent of the impact of flow curvature can be simulated accurately.

Note that these results only hold when the freestream is neglected. If this would have been included, the velocity on the airfoil would have varied over the rotation, and the equations would not be this simplified. Therefore, it is important to realise the results show an approximation.

7.2.1 Pitching Implications

To show how these results affect the behaviour of an airfoil, a comparison is made between a steady airfoil in rectilinear flow and an airfoil undergoing a VAWT rotation. To that extent, the pressure distribution of a NACA0015 is computed in a case without pitching, so where the chord-to-radius ratio is zero and for a chord-to-radius ratio of 0.1. The results are shown in Figure 7.5. The angle of attack is zero and the pitching location is 0.5. The solutions are computed using the U2DIVA panel code.

As the NACA0015 is a symmetric profile, at zero angle of attack, no pressure difference over the surface is obtained, as the surrounding flow is symmetric. But due to the added rotation, an asymmetric surface velocity distribution is obtained, resulting in a pressure difference. This shows that a pitching airfoil will produce a different lift force. The geometry of the airfoil, the sense of the rotation, and the starting orientation of the airfoil all determine whether there will be a lift increase or decrease.

This model shows that to investigate the influence of flow curvature, which is dependent on the chord-to-radius ratio, the pitching rate can be varied. By implementing this rotational rate in XFOIL, the impact of flow curvature can be made visible in both inviscid and viscous results. Consequently, by using the airfoil optimiser, also the impact on airfoil design can be shown.

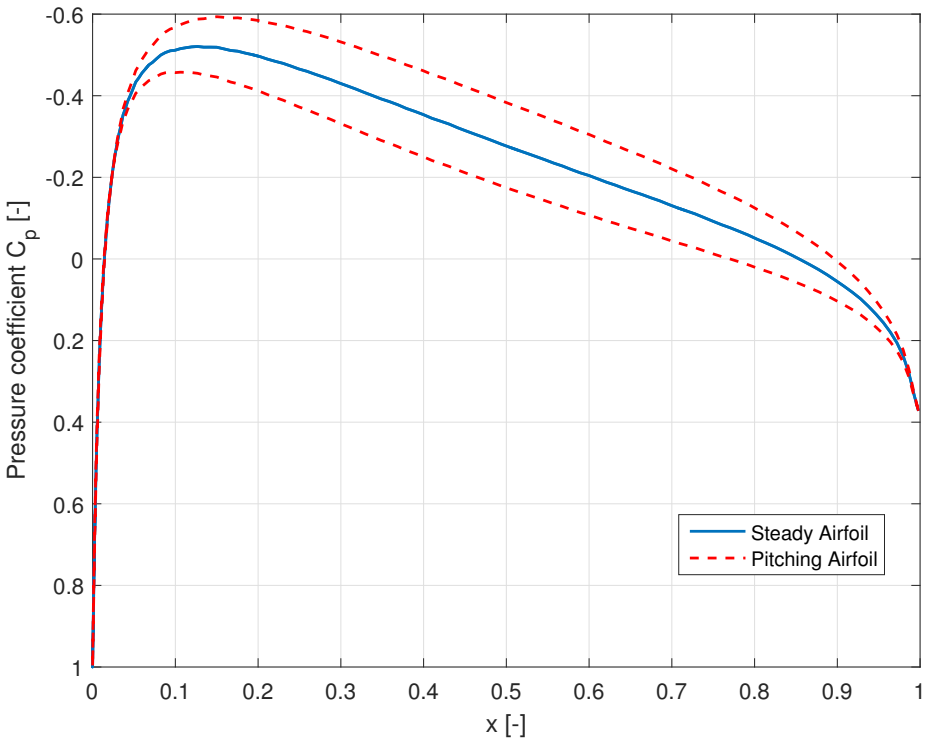

Figure 7.5: The pressure distribution for a steady airfoil and a pitching one.

7.3 Application

Now that the fundamentals of the code are clear and a model is developed which can simulate flow curvature, the actual functions and sub-routines of the XFOIL source code can be investigated. In this section, the code will be scrutinised to find where the algorithm should be altered. Afterwards, the implementation of the pitching model will be discussed. and the respective modifications it requires shall be clarified. An instruction will be provided on how a user can access the new functionality.

7.3.1 XFOIL Source Code

Below, the original XFOIL code shall be investigated, to have a good insight in its routines. It is written in FORTRAN77, and is built-up out of sub-routines called from a main script. Each of these routines are located in various source files, but are not all relevant. All sub-routines which are called in the computation of the pressure distribution and aerodynamic coefficients are considered below. A short description is presented, explaining its relevant actions. The sub-routines are structured in a manner which shows the hierarchy of the functions. Behind each function is written in which source file the function is present.

Algorithm 1 XFOIL Source Code

XFOIL (xfoil.f)
- Define an airfoil by using the NACA-command, or loading a coordinate file.
- Go to the 'direct operating points' routine by calling OPER.

OPER (xoper.f)
- Prescribe an angle of attack by typing ALFA.

ALFA (xoper.f)
- The SPECAL sub-routine is called to converge to the specified angle of attack.

SPECAL (xoper.f)
- The surface vorticity distributions for an angle of attack of 0°and 90°are computed in the GGALC sub-routine.

GGCALC (xpanel.f)
- Based on the streamfunction, the freestream influence for those angles of attack are computed. The Kutta condition is applied, and the system of equations is solved by Gaussian elimination in the following sub-routine.

BAKSUB (xsolve.f)

- Using the specified angle of attack, the two previously computed vorticity distributions are weighted to obtain the surface vorticity distribution.

CPCALC (xfoil.f)
- The steady Bernoulli equation is applied to find the pressure distribution.

CLCALC (xfoil.f)
- The lift, drag, and moment coefficient are computed based on the pressure distribution.

- For the viscous solution, **VISCAL** (xoper.f) is called, which performs similarly to **SPECAL**, but also includes boundary layer characteristics.

7.3.2 Streamfunction Modification

The vorticity distribution, which is the basis of all further solutions, is computed in the GGCALC routine. Here the streamfunction for the freestream flow and the vorticity and source distribution is applied. As shown before in section 7.2, the airfoil can be modelled as continuously pitching, resulting in added surface velocities. These rotation induced velocities can be included in the horizontal and vertical surface velocity components. The resulting streamfunction is derived below.

The definition of the streamfunction is as such that it defines streamlines where the volumetric flow rate of the fluid is constant, which is shown in Equation 7.20 (Katz and Plotkin [52]). Worked out, this results in XFOIL's original streamfunction formulation in Equation 7.22, where the subscript src refers to the source code.

$$\frac{\partial \Psi}{\partial x} = -v \quad ; \quad \frac{\partial \Psi}{\partial y} = u \tag{7.20}$$

$$u = u_\infty \quad ; \quad v = v_\infty \tag{7.21}$$

$$\Psi_{src} = -v_\infty x + u_\infty y = -q_\infty \sin(\alpha)\, x + q_\infty \cos(\alpha)\, y \tag{7.22}$$

Now, based on Figure 7.6, the added velocities are included, to obtain Equation 7.23 and Equation 7.24. Note that these are relative to the airfoil surface, and the pitching location (x_p,y_p) is variable. The corresponding streamfunction components can be found by integrating. On the premise of superposition, these components can be added to obtain the altered streamfunction shown in Equation 7.27, where the subscript mod refers to the modification. Note that the pitching location is equivalent to the mounting location used in the virtual airfoil methods, and therefore these terms are interchangeable.

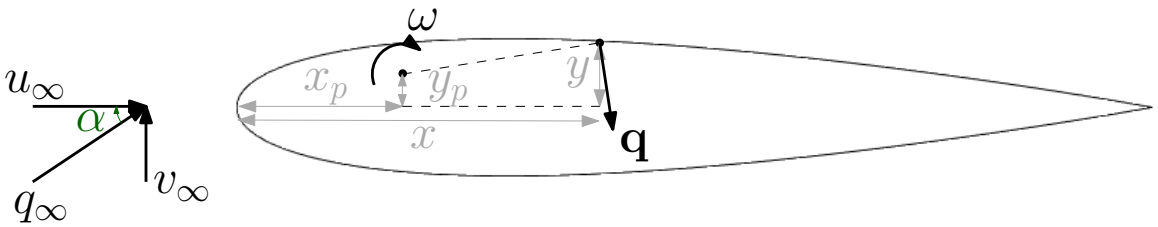

Figure 7.6: Parameter definitions of a pitching airfoil.

$$u = u_\infty - \omega(y - y_p) = u_\infty - \omega y + \omega y_p \tag{7.23}$$

$$v = v_\infty + \omega(x - x_p) = v_\infty + \omega x - \omega x_p \tag{7.24}$$

$$\Psi_x = \int -v\, dx = -v_\infty x - \frac{\omega x^2}{2} + \omega x_p x \tag{7.25}$$

$$\Psi_y = \int u\, dy = u_\infty y - \frac{\omega y^2}{2} + \omega y_p y \tag{7.26}$$

$$\Psi_{mod} = \Psi_x + \Psi_y = -q_\infty \sin(\alpha)\, x + q_\infty \cos(\alpha)\, y - \omega \left(\frac{x^2 + y^2}{2} - (x_p x + y_p y) \right) \tag{7.27}$$

Verification To verify this modification actually is correct, a small test case is set up. Based on thin-airfoil theory, an analytical approximation of the lift coefficient can be calculated for an unsteady flat plate. This equation is found in Leishman [53] and repeated in Equation 7.28. Here, $\dot{h}$ is the plunge velocity, which is zero in this case, a is a fraction of the semi-chord b, and $\dot{\alpha}$ is the pitching rate. a is measured from the centre of the airfoil and determines where the pitching axis will be on the chord. This analytical lift coefficient shall be compared with the results computed by a point vortex distribution which is found by applying the impermeability boundary condition. It shall also be compared with a constant vortex distribution based on the streamfunction formulation, as this algorithm was readily available. This provides the opportunity to verify the streamfunction modification.

$$C_l = 2\pi \left[\alpha + \frac{\dot{h}}{Q_\infty} + b \left(\frac{1}{2} - a \right) \frac{\dot{\alpha}}{Q_\infty} \right] \tag{7.28}$$

The results are shown in Figure 7.7, and show very good correspondence between the two methods and the theoretical solution. The lift coefficients for two test cases are indicated in the legend of either plot. Results are shown for both the original streamfunction formulation for a steady flat plate, and for a quasi-steady pitching plate. This shows that modifying the streamfunction in the explained manner is valid.

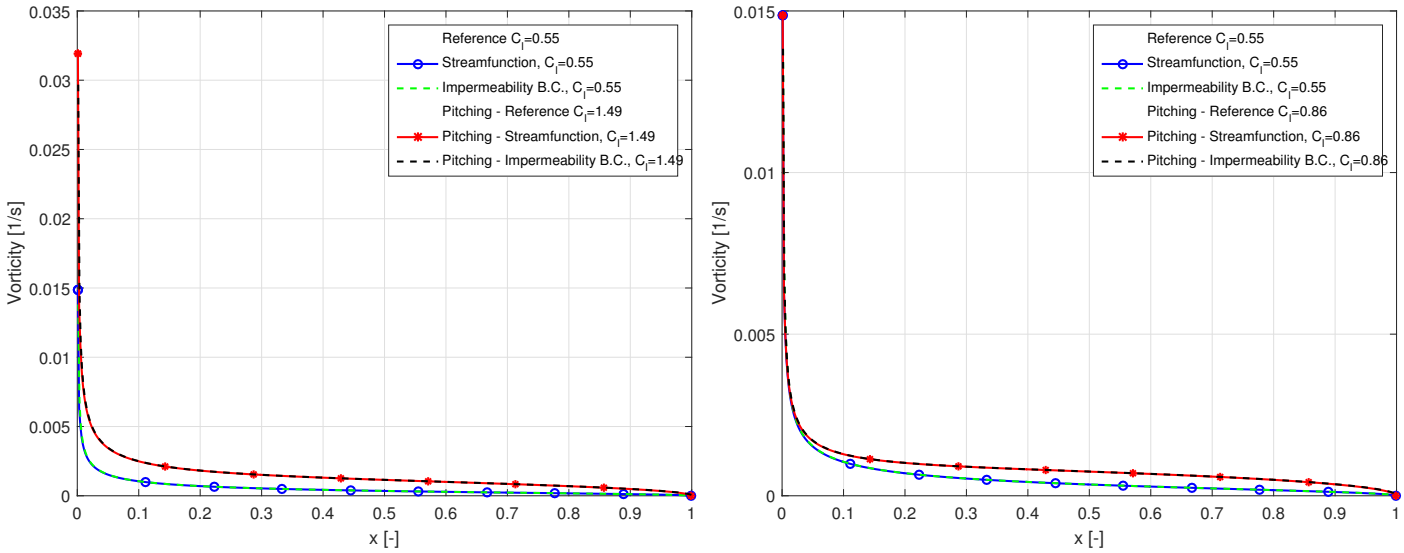

(a) Pitching location at the leading edge.

(b) Pitching location at half chord.

Figure 7.7: Vorticity distribution for a pitching flat plate at an angle of attack of 5 degrees, with a pitching rate of 0.2.

7.3.3 Implementation

The implementation of the pitching model is easily accomplished by altering the streamfunction. This however, turned out not to be the only modifications necessary to obtain an accurate solution. Below, two other required alterations are described, namely the use of induced velocities and a change of reference frame.

Induced Velocities

In the XFOIL source code, the vorticity is set equal to the tangential velocity. However, when applied, this proved to produce a wrong pressure distribution. Therefore a further investigation into the computation of pressure was performed. This was done by looking at the velocities induced by the vorticity. As mentioned a constant-strength vortex panel method was readily available and its induced velocities could be found in Katz and Plotkin [52], Equation 7.29 and Equation 7.30. Note that these velocities are calculated in the panel coordinate system, so a transformation of reference frame before and after is necessary.

$$u_p = \frac{\gamma}{2\pi}\left[\tan^{-1}\left(\frac{z-z_2}{x-x_2}\right) - \tan^{-1}\left(\frac{z-z_1}{x-x_1}\right)\right] \tag{7.29}$$

$$v_p = -\frac{\gamma}{4\pi}\ln\left(\frac{(x-x_1)^2+(z-z_1)^2}{(x-x_2)^2+(z-z_2)^2}\right) \tag{7.30}$$

By looking at the velocity vectors around the airfoil and converging to its surface, a nice agreement was found with the quasi-steady solution of the U2DIVA panel code. Figure 7.8 shows the results for a NACA0015 airfoil at zero angle of attack, chord-to-radius ratio of 0.2, and a pitching location at either $0.25c$ or $0.5c$. The solution is computed at collocation points on half the panel, slightly outside the surface 10^{-15} to avoid singularities. Note that this is not yet the implementation in XFOIL, and the discrepancy between the solutions shall not further be investigated.

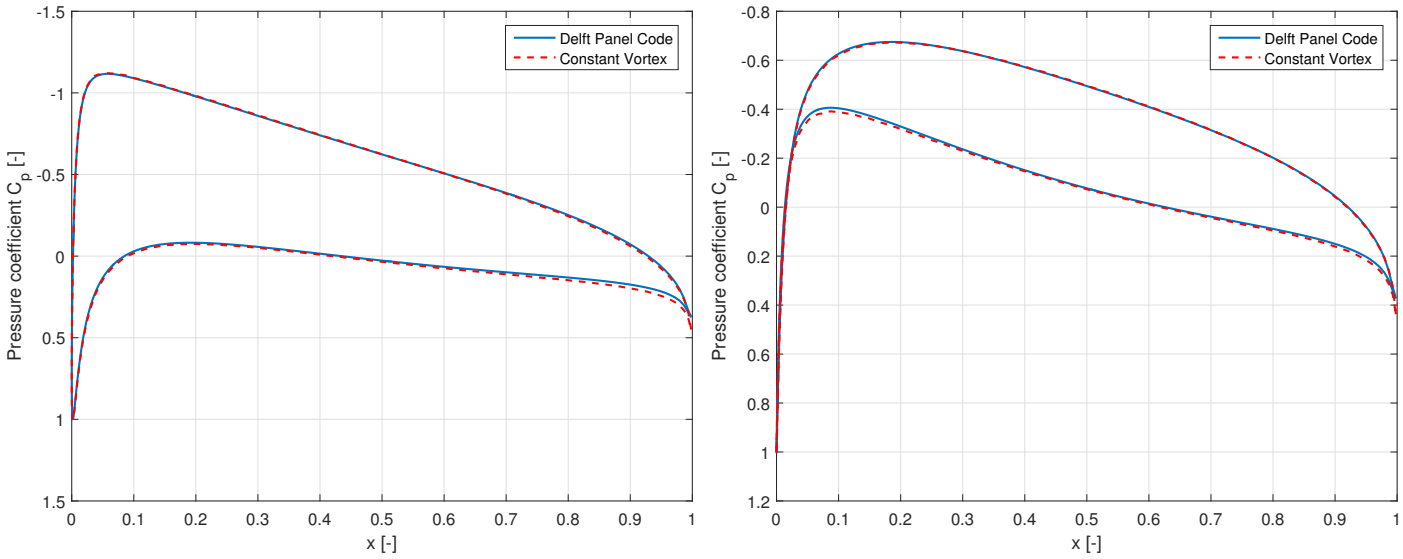

(a) Pitching location at a quarter of the chord.

(b) Pitching location at half of the chord.

Figure 7.8: Pressure distribution computed by the U2DIVA panel code and the induced velocity near the surface of a constant-strength vortex method, for NACA0015 at an angle of attack of 0 degrees, with a chord-to-radius ratio of 0.2.

Change of Reference Frame

Because the airfoil is no longer static with respect to the freestream, but is quasi-steadily pitching, an erroneous pressure distribution will be obtained if the original Bernoulli equation is used. Instead, the pressure must be computed in the moving airfoil reference frame, and therefore its own velocity has to be included. Based on equation (13.28a) in Katz and Plotkin [52] the pressure can be computed with the surface velocity distribution and the airfoil's kinematic velocity. The equation is repeated in Equation 7.31, where the time-dependent variables are omitted, as the solution is quasi-steady, and therefore not changing over time.

$$C_p = -\frac{(\nabla\Phi)^2}{Q_\infty^2} + \frac{2}{Q_\infty^2}\left[\boldsymbol{V}_0 + \boldsymbol{\Omega} \times \boldsymbol{r}\right] \cdot \nabla\Phi \tag{7.31}$$

Now, the kinematic velocity of the airfoil is purely the rotational velocity due to pitching. And the derivative of the potential and the Laplacian result in the surface velocities and their square respectively. As the rotational velocity is easily computed in a tangential and normal surface coordinate system, so shall the velocities due to the vorticity be calculated.

Modified Code

All three additions are included into the XFOIL source code. The streamfunction formulation is altered to accommodate a pitching motion. Using a newly created sub-routine called INDUCED_VEL the panel-averaged vorticity distribution is used to calculate the induced velocities at desired collocation points. And finally the pressure is computed using the modified equation. The new calculation routine is shown below, where for brevity the previous descriptions are omitted, and only the additions are described.

User Commands The code will be adjusted as such that the original functionality remains untouched. To that extent, any new parameters shall be made globally available, just as for instance the Reynolds number is defined in the source code. These parameters shall include the pitch-rate and normalised pitching x- and y-location. These variables can be specified by the user when the PTCH-command is used, found in the OPER menu. Afterwards, the regular procedure is applied to obtain desired results.

Algorithm 2 Modified XFOIL

XFOIL (xfoil.f)

- **OPER** (xoper.f)
  - **PTCH** (xoper.f)
    - Prescribe the pitching rate and pitching location.
  - **ALFA** (xoper.f)
    - **SPECAL** (xoper.f)
      - **GGCALC** (xpanel.f)
        - The altered streamfunction is included here.
        - **BAKSUB** (xsolve.f)
      - **CPCALC** (xfoil.f)
        - The panel-averaged vorticity distribution is used to find the induced velocities on the surface with **INDUCED_VEL** (xfoil.f).
        - The altered pressure equation is used afterwards.
      - **CLCALC** (xfoil.f)
        - The same applies to the calculation of the aerodynamic coefficients.

7.4 Results

This section shows the computed results when the modified software is put to the test. The effect of each of the three modifications is shown and thereafter the steady and quasi-steady pressure distributions. Then, an analysis is performed on the influence of the free variables the model has. Lastly, the found discrepancy between the XFOIL and U2DIVA panel code solutions is addressed.

7.4.1 Vorticity Distribution

The above results show a good promise for an implementation in XFOIL. However, XFOIL uses a linear vortex distribution and even with an extensive amount of attempts, its induced velocities could not be implemented in XFOIL. Therefore it has been chosen to average the linear distribution to a constant strength per panel. As for the constant-strength vortex distribution the velocities could be computed. To show this is allowable, both the linear vorticity distribution computed by XFOIL and its panel averaged constant version are shown in Figure 7.9. As can be seen, virtually no loss of precision is obtained as the solutions match very well. If a smaller amount of panels is used, it is expected that the difference increases. The distributions are computed for a NACA0015 profile at angle of attack, rotating around its quarter chord position with a rate of 0.2 rad/s.

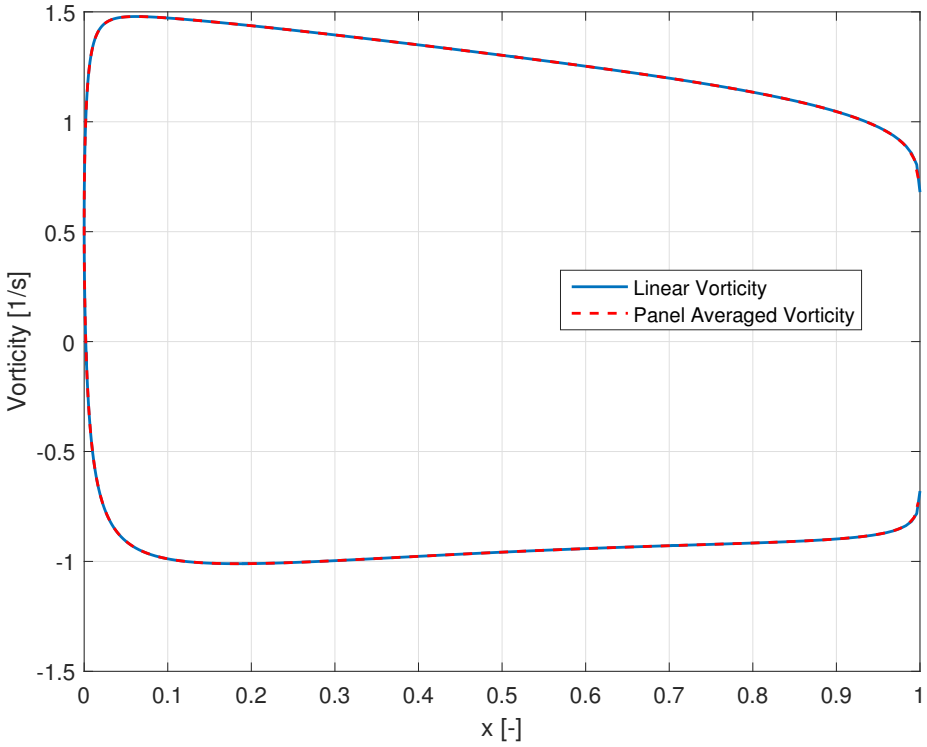

Figure 7.9: Linear and panel averaged vorticity distribution from XFOIL.

7.4.2 Modifications

Figure 7.10 shows the results of each of the three consecutive modifications. Respectively the distributions are shown for; 1 just the streamfunction modification, 2 altering the pressure calculation, and finally 3 including the induced velocity computation. In the magnified portion of the plot, it is clearly seen that the solution improves with each addition.

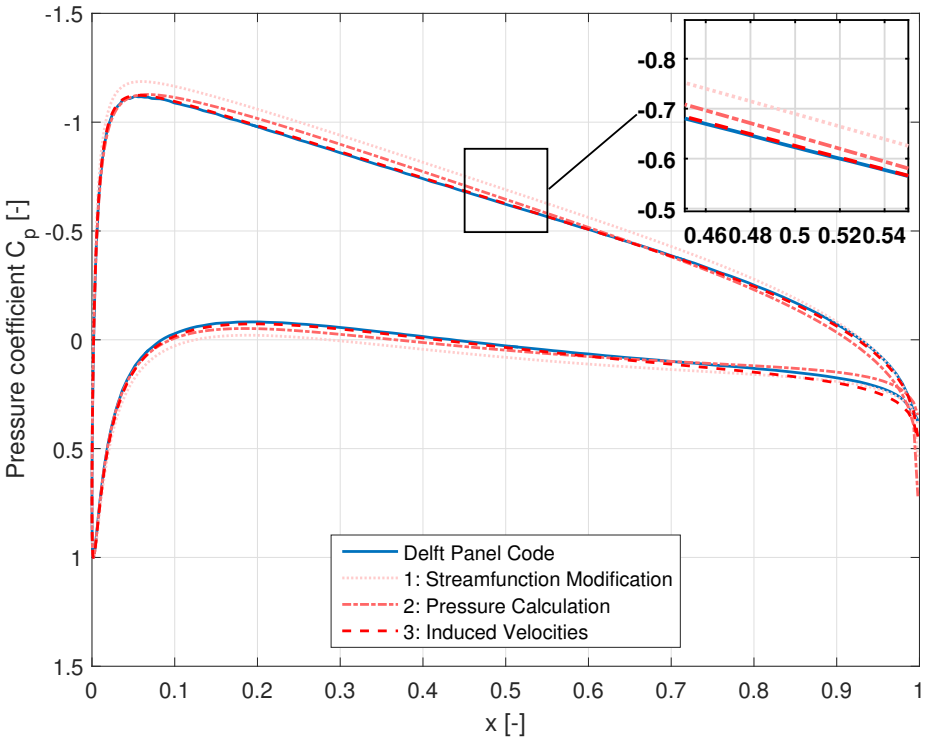

Figure 7.10: Pressure distribution computed by the U2DIVA panel code and various modifications in XFOIL, for NACA0015 at an angle of attack of 0 degrees, with a chord-to-radius ratio of 0.2 and a pitching location at a quarter of the chord.

7.4.3 Steady Pressure Distribution

When the pitching rate is set to zero, and the steady pressure distributions are computed for a NACA0015 profile at an angle of attack of 5 degrees, Figure 7.11 is obtained. As can be seen, the distributions match very well, and there is only a 1% difference between the lift coefficients. This shows that the modifications for the pressure calculation perform accurate enough. The solutions are computed slightly outside of a collocation point located at the centre of the panel.

7.4.4 Quasi-Steady Pressure Distribution

With a non-zero pitching rate, the surface velocities are altered by the rotation. This affects the accuracy of the XFOIL solution and as a result, it does not match as well as in the steady case. Figure 7.12 still shows a good approximation of the U2DIVA panel code solution by XFOIL. The suction surface of the airfoil corresponds very well, and there exists only a small offset for the rest of the solution. The leading and trailing edge velocities are captured well.

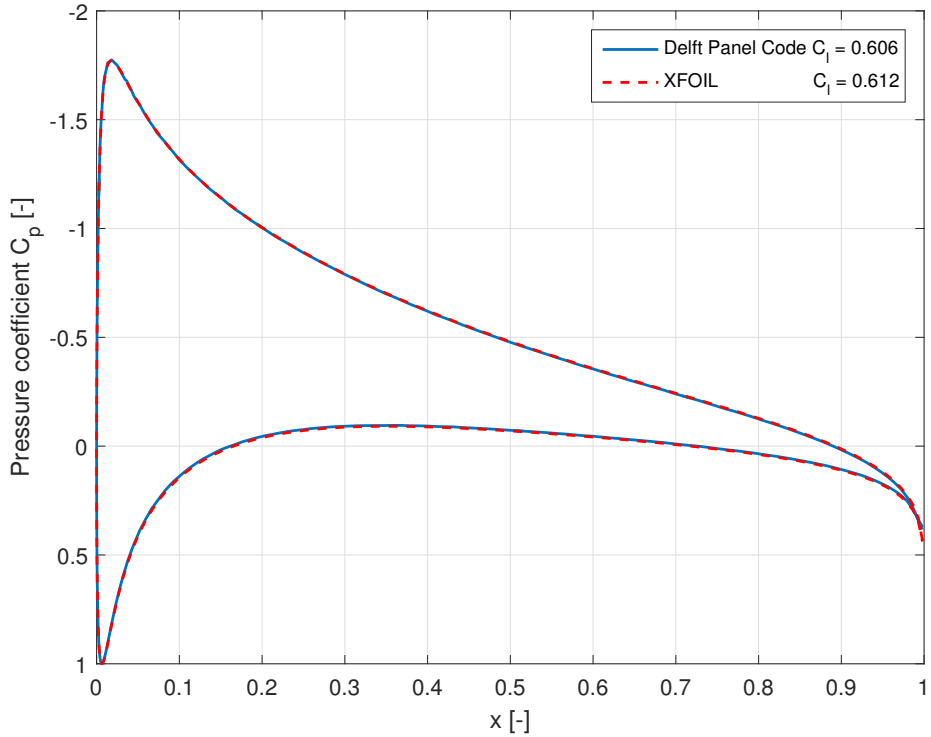

Figure 7.11: Steady pressure distributions for a NACA0015 at 5 degrees angle of attack, from the U2DIVA panel code and XFOIL.

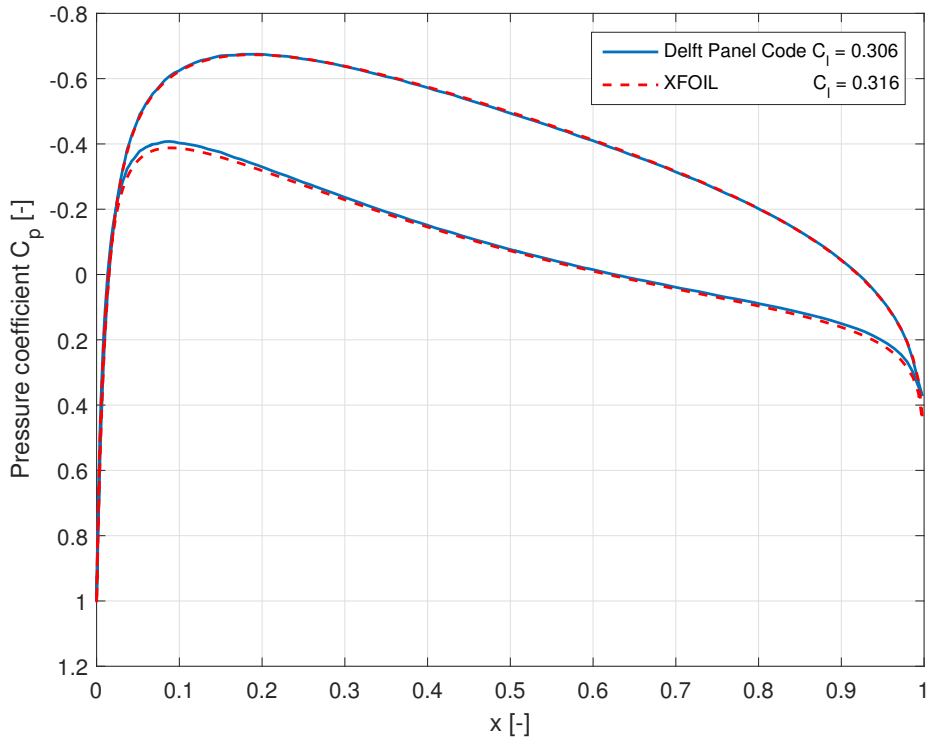

Figure 7.12: Pressure distribution computed by the U2DIVA panel code and XFOIL, for NACA0015 at an angle of attack of 0 degrees, with a chord-to-radius ratio of 0.2 and a pitching location at half of the chord.

Also for different airfoils, under different conditions, the solutions match very well. Figure 7.13a depicts the solutions for a NACA2415 airfoil with an angle of attack of 0 degrees, pitching rate of 0.1, and a pitching location at 0.25% of the chord. And in Figure 7.13b the pressure distributions are shown for a NACA24012 airfoil with an angle of attack of 5 degrees, pitching rate of 0.05, and a pitching location at $0.75c$.

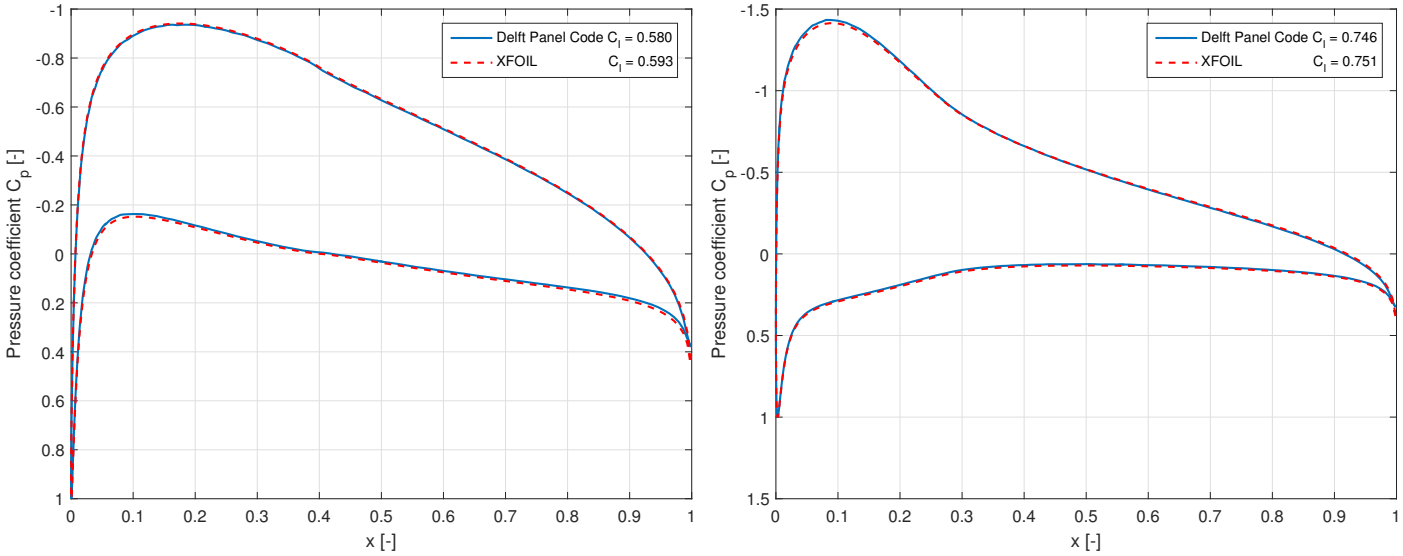

(a) Solutions for a NACA2415 profile.

(b) Solutions for a NACA24012 profile.

Figure 7.13: Pressure distribution solutions from the U2DIVA panel code and modified XFOIL, for two airfoil under various conditions.

Viscous results have previously been shown in chapter 6, with the comparison of the flow curvature models. The accuracy of this solution is unknown however, as there is no comparison method readily available to verify the viscous solution. Therefore it must be assumed that the implemented modifications are also valid for the viscous calculations XFOIL performs. These remain untouched.

7.4.5 Influence of Parameters

The following will discuss what effect a change of one of the free variables has on the quasi-steady pressure distribution. The analysis is performed by varying the angle of attack, pitching rate, or the pitching location. It has been verified that the solution is in the same order of accuracy for any variation of the airfoil geometry. Therefore a standard NACA0015 will be the subject of investigation.

Angle of Attack

When increasing the angle of attack, the inviscid solutions of the U2DIVA panel code and XFOIL converge. For a pitching rate of 0.1 and a pitching location of 0.5, with each increment of 5 degrees, the difference between the lift coefficient decreases with about 0.5%. This can be explained by the fact that for the inviscid solution, the surface velocities increase with increasing angle of attack. The difference between pressure distributions induced by the added rotation therefore diminishes relatively.

Also, the starting orientation of the airfoil determines whether a rotation will have an increasing or decreasing effect on the lift. If an airfoil at a positive angle of attack is pitched nose up, the rotation induced velocities will increase the pressure difference and therefore the lift. A negative rotation results in a lift decrease. Also, the opposite holds when the airfoil starts with a negative angle to the flow.

Pitching Rate

The pitching rate determines the magnitude of the rotational induced velocities. It therefore has a large impact on the pressure distribution and therefore the lift coefficient. The sense of the rotation and the geometry of an airfoil determine the impact. Namely, the former will either increase the existing velocities or act opposite to them. The rotation induced velocities on either surface are opposite to those on the other surface. Therefore, when the rotation results in an enlargement of the surface velocities, an increase in lift is felt, and the same holds for the opposite.

For a cambered profile, as the pressure difference is already increased with respect to a symmetric airfoil, the added rotation will have a smaller effect. For a NACA0015 profile at an angle of attack of 5 degrees, a rotation in either direction of 0.2 rad/s around $0.5c$ will result in a 50% change of lift coefficient. Now for a highly cambered NACA6415 profile under the same conditions a nose up rotation will result in a 20% lift increase, and a nose down pitch in a 21% decrease.

Pitching Location

The pitching or mounting location will affect the arm the surface has to the centre of rotation and resultantly the magnitude of the rotation induced velocities. This in turn affects the vorticity distribution, which needs to uphold the impermeability boundary condition on the surface. As a result, with increasing arm and therefore velocity magnitude, the lift increases. This can be seen in Figure 7.8, where for the U2DIVA panel code and the constant-strength vortex panel method the results are shown for a NACA0015 at 0 angle of attack, rotating with 0.2 rad/s, around either $0.25c$ (a) or $0.5c$ (b). As for the quarter chord position the arm towards the trailing edge is longer, the rotational induced velocity is higher here, and the vorticity distribution has to account for that. As a result, the pressure difference and lift are higher.

This effect is also seen in the thin-airfoil lift coefficient approximation by Leishman [53], in Equation 7.28. When a is 0, meaning the pitching location is at half the chord, the influence of the pitching rate will be halved. But when the location is at a quarter chord, with $a = -\frac{1}{2}$, this half falls out and the pitching rate will have double the impact on the lift coefficient.

The pitching location will furthermore alter the shape of the pressure distribution, as seen in Figure 7.8. This is because the local angles between the rotational velocity and the surface change. As the airfoil has a curved surface, the change in shape is difficult to predict.

7.4.6 Discrepancy

At this point it is unclear where the difference between the solutions of the U2DIVA panel code and the XFOIL implementation originates. The solutions do not match perfectly, and this could be ascribed to the fact that the algorithms use different methods and equations to compute the vorticity and surface velocities. Therefore there is an inherent difference between the two systems and their solutions will likely never match completely.

It has been checked whether the discrepancy is dependent on the number of panels. However, as the amount increases, no improvement of the correspondence has been found. Still, the maximum number of panels XFOIL is capable of computing, namely 280, is used.

Lift Coefficient

The lift coefficient is a good measure of how close the distributions are, as it is a consequence of the pressure over distribution over the airfoil. It can be obtained by summing the contributions of each panel to the force normal to the flow.

When the lift coefficients are compared, a discrepancy between them is found. The difference is as low as 2% of the U2DIVA panel code lift coefficient in some cases and even up to 10%. As mentioned, this might be explained by the huge difference in the chain of equations for the different methods, where in each step numerical errors can be obtained as well. The result is that a different vorticity is obtained, resulting in a different pressure and therefore force distribution.

Pitching Location

That the XFOIL implementation is not exactly flawless is seen when the pitching location is changed to outside its regular bounds. When only the horizontal mounting location is varied towards the leading edge or even beyond, the pressure at the trailing edge of the airfoil seems to be miscalculated. The opposite occurs when the location is changed towards the trailing edge or further. The velocities are lower than the U2DIVA panel code, which is probably caused by an inaccuracy in including the rotational induced velocities. Namely, as soon as the arm increases, the solution diverges.

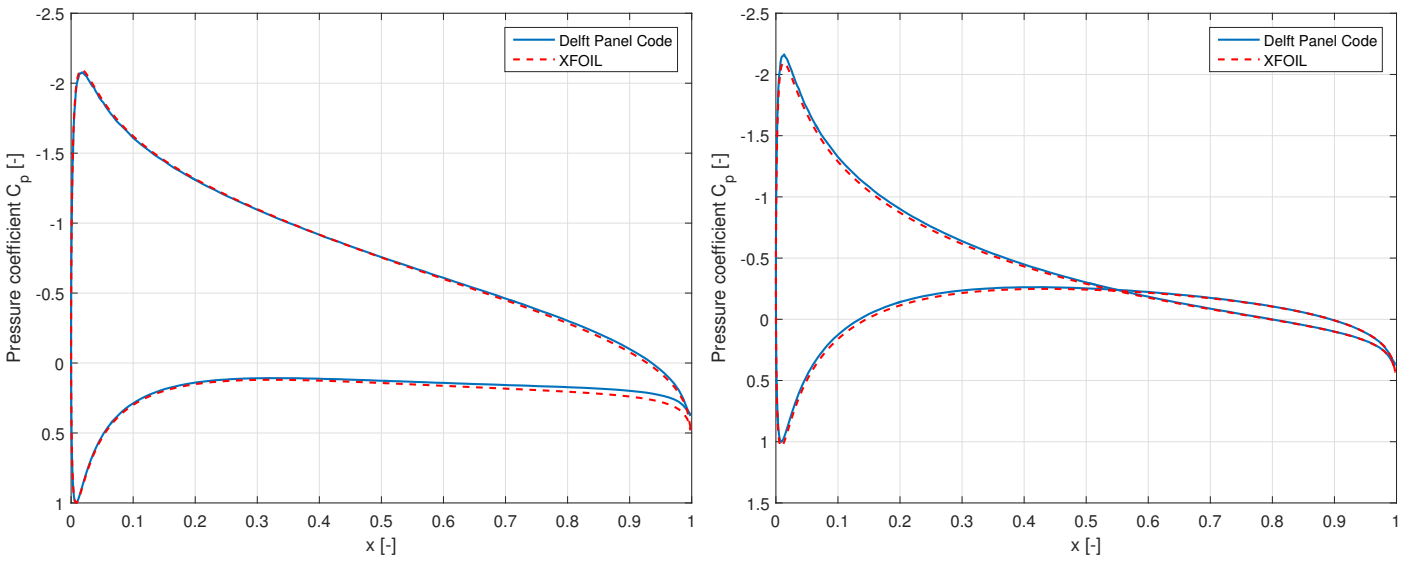

(a) At the leading edge.

(b) At the trailing edge.

Figure 7.14: Pressure distributions for a horizontally changing pitching location.

The same happens when only the vertical pitching location is varied. With respect to the solution where y_p is zero in Figure 7.10, either the suction side or the pressure side changes more when y_p is changed to 0.5 or -0.5 respectively. This can be seen in Figure 7.15. Again, this error could be produced by a mistake in the inclusion of the rotational induced velocity. Naturally these pitching locations are infeasible, but still the XFOIL solution should have matched the U2DIVA panel code's.

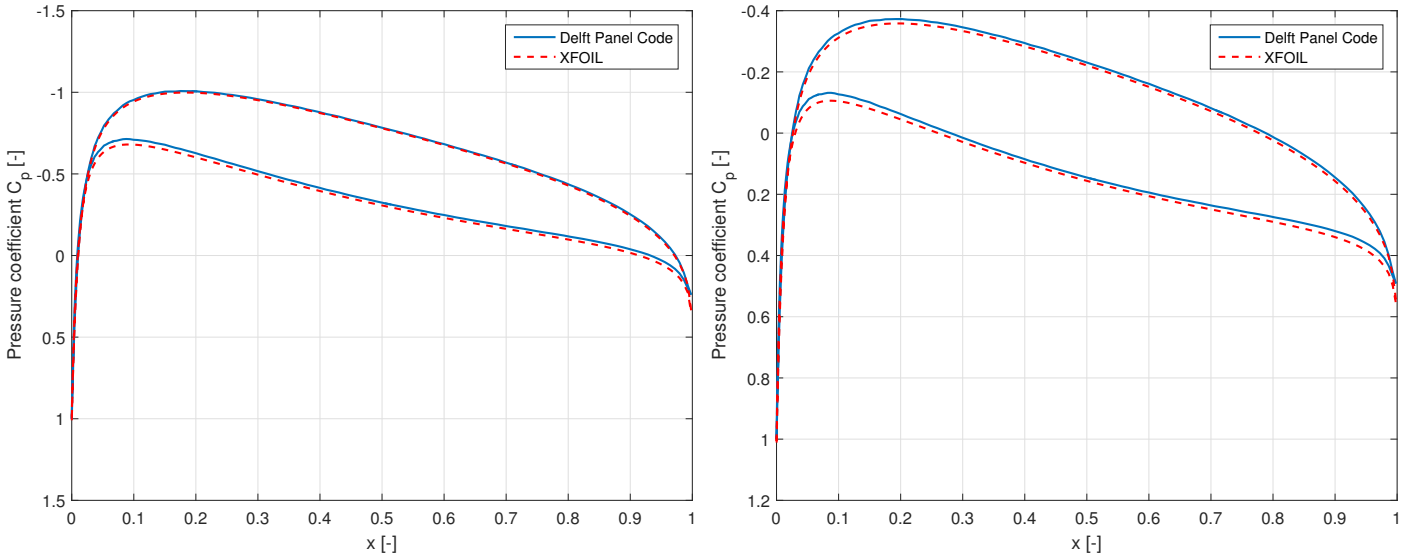

(a) Above half the chord.

(b) Below half the chord.

Figure 7.15: Pressure distributions for a vertically changing pitching location.

7.5 Chapter Conclusions

- This chapter first described the foundations of the airfoil analysis software XFOIL, identifying it as a potential flow solver using a panelled vorticity and source distribution on the airfoil and wake, imposed on the freestream, solved using a streamfunction formulation. Viscous coupling takes place using momentum and kinetic energy relations.
- By kinematically comparing an airfoil in VAWT rotation to an airfoil pitching around its own axis, a useful model could be applied into the source code. By varying the pitch rate of the airfoil, the chord-to-radius ratio could be varied, eventually providing the opportunity to investigate flow curvature effects.
- The necessary modifications in XFOIL proved a modification of the streamfunction formulation, to include the rotational induced velocities; the inclusion of induced velocities by a panel averaged linear vorticity distribution near the surface to compute the pressure; and a change of reference frame for the pressure calculation. The new functionalities are accessed by the PTCH-command, letting the user define a global pitch rate and -location.
- The results show a nice comparison to the U2DIVA panel code in varying situation, where the lift coefficient difference is below 10%. It was shown that profiles at a higher angle of attack showed better correspondence.
- Also, the pitch rate, together with the starting orientation of the airfoil, determines the amount of lift in- or decrease by affecting the pressure distribution. Cambered airfoils showed to be less affected.
- By varying the pitch location, the amount of lift changes, as the arm to the pitch location lengthens or shortens. Also, the discrepancy to the benchmark showed to be increased when the arm increased.

Chapter 8

Airfoil Optimisation

As mentioned before, airfoils specifically tailored for a vertical axis wind turbine have the possibility to improve efficiency and boost performance. It it therefore crucial that a well performing airfoil optimisation strategy is used. One could argue to let an optimiser freely design a shape to meet desired requirements. However, this would be extremely computationally expensive as the design space is huge. Next to that, if the most accurate airfoil performance analysis method is used, for instance computational fluid dynamics, this would increase the computational cost even more. This chapter will cover the results of a simpler and less expensive airfoil optimisation campaign, where the solutions will be bounded and found by a multi-objective optimiser, coupled with XFOIL, without settling for accuracy and precision.

As airfoil optimisation is not the main topic of this thesis, the results will mostly show a proof of concept. The airfoils found when varying the pitch-rate will show whether including flow curvature has a large influence and whether it would have merit to include in a design process. This means that no extensive simulations are ran, and the requirements will be kept simple.

The first section in this chapter will give a concise description of the Optiflow solver. It will cover the working principles of the algorithm. Afterwards, the optimisation strategy shall be presented. This section will give insight into with which inputs the optimisations will be ran. Finally, the results shall be discussed.

A lot of this work has already been covered by my predecessor Rody Kemp during his thesis. Much of the following chapter therefore relies on his research. This means that a lot of similarities exist between the discussion below and his report.

8.1 Description

The airfoil optimiser Optiflow was developed during the thesis work of G. de Oliveira [51]. In essence, this optimiser generates a large number of 'random' airfoils and computes their performance in XFOIL. By minimising for two objectives, it seeks the most optimal airfoils meeting the requirements. To find an airfoil for a VAWT specifically, the optimiser will be coupled with the modified version of XFOIL, which now includes the simulation of flow curvature effects. The resulting airfoils will be investigated and compared to optimised airfoils found for a pitch-rate of 0. This will shed light on the impact of flow curvature on the design of an airfoil.

The Optiflow software will be described in three main topics, the genetic algorithm and its Pareto front, the coupling with XFOIL via the objective functions, and the airfoil parametrisation. What the optimiser does is create a lot of airfoils using an airfoil parametrisation technique. A reference dataset will provide initial guesses for the optimiser to increase simulation speed. Each of the created airfoils will be fed into XFOIL to retrieve the aerodynamic performance and will be structurally analysed. Afterwards, their performance will be compared with other airfoils in the dataset and it will be given a score. In this manner the most optimal airfoils will be found.

8.1.1 Genetic Algorithm

The optimiser uses Matlab's genetic algorithm optimiser $\mathrm{gamultiobj}$, which is able to find minima of multiple objective functions. It has built-in properties to avoid getting stuck at a local optimum and to increase diversity in the solutions. In this case two functions will be used, which will be described below. When using multiple objectives, it is extremely difficult to optimise for a single best solution. Namely, having found a optimum for one objective, it is highly unlikely this solution will also be the best with respect to the second objective. Therefore, this optimiser will produce a so-called Pareto front. This frontier contains the best solutions of a dataset, with optimal values for both objectives. This is visualised in Figure 8.1.

The Pareto front is comprised of the optimal solutions for objective functions OF_1 and OF_2, they are called the Pareto-set and are indicated with the blue points in the figure. These points scored better than all the rest in the dataset, who are indicated with the white points. Point (a) is the optimal solution of the set of solutions indicated with the red points for objective function OF_2. Likewise, point (b) is the best of the green solutions in aspect of the other objective OF_1. Together with similar optimal solutions, they form the front. Now when one tries to improve solution (c) in the Pareto-set, by shifting it to point (d), the solution will always improve for one objective and deteriorate for the other. This shows that there is almost never a single optimal solution.

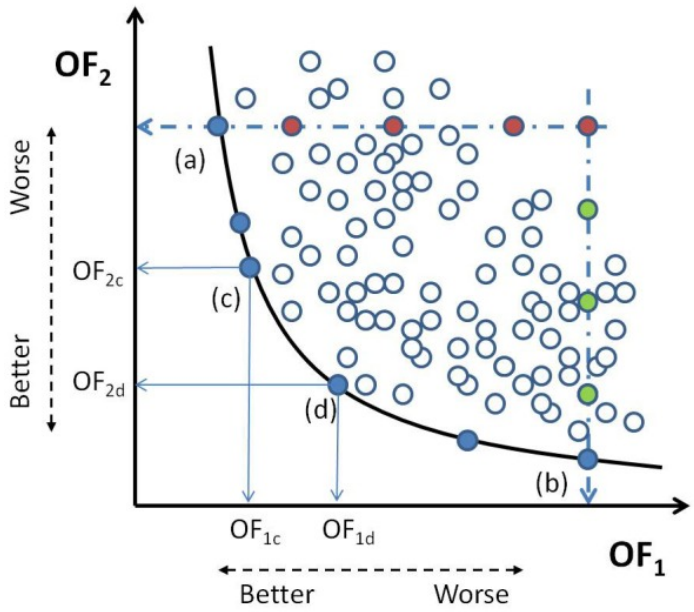

Figure 8.1: Pareto front of a genetic algorithm [1].

[1] As found on `http://krauthammerlab.med.yale.edu/imagefinder`, visited on 06-10-2015.

8.1.2 Objective Functions

To find an airfoil which is optimally performing for a VAWT, the optimiser searches for profiles which optimise the power output of the turbine. According to Simão Ferreira and Geurts [37], this is equal to optimising the shedding of the wake of the turbine, which determines the energy conversion from the flow. The wake shed from the turbine is dependent on the load distribution of the blades. Their research shows that in order to optimise this distribution, the drag produced by the airfoil should be minimised, resultantly minimising the ratio of the average lift curve slope over the average drag coefficient over a rotation: $\frac{\overline{C_{l_\alpha}}}{\overline{C_d}}$.

To calculate this coefficient, the lift and drag polars are computed by XFOIL, both for a free and forced transition on the airfoil, after which their solution is averaged. From the first, the slope of the lift polar C_{l_α} is obtained. The found drag coefficients C_d are filtered by weighting the values based on whether its angle of attack occurs often in one rotation of a VAWT. This means that in the drag polar, coefficients at uncommon angle of attack are taken less into account when computing the objective.

The inclusion of roughness, achieved by tripping the boundary layer of the airfoil near the leading edge in XFOIL, will result in conservative airfoils. Namely, if only clean polars are used, the resulting airfoils would encounter undesired turbulent transition due to roughness when put in practice. By already accounting for that during the optimisation process, more conservative results are obtained.

To also obtain structurally advantageous profiles, the second objective function tries to maximise the bending stiffness in flapwise direction of the blade [37]. This is done by computing the moment of inertia of the skin of the airfoil is based on the distance to the centroid of the airfoil. The skin is assumed to be thin. Furthermore a penalty is applied to airfoils with a relative thickness above 33% and for bad aerodynamic performance. For instance, structurally a rectangle would be optimally stiff, but this design is aerodynamically unusable.

8.1.3 Airfoil Parametrisation

To generate the to be analyses airfoils, use is made of the Class Shape Transform (CST) developed by Kulfan [54]. This method creates an airfoil using three functions based on the horizontal coordinate of the airfoil, as shown in Equation 8.1. Here, ψ, ζ, and ζ_{TE} are the normalised x, y, and trailing edge thickness $\Delta\zeta_{TE}$ respectively.

$$\zeta(\psi) = \sqrt{\psi}\,(1-\psi)\cdot\sum_{i=0}^{N} A_i\psi^i + \psi\zeta_{TE} = C(\psi)\cdot S(\psi) + \psi\zeta_{TE} \tag{8.1}$$

The class function $C(\psi)$ ensures the basic shape of an airfoil. At the leading edge ($\psi = 0$) the function will create an infinite slope and a finite curvature, at the trailing edge ($\psi = 1$) it will be zero, as to result in a finite trailing edge thickness. This thickness is simply controlled by a user input for $\Delta\zeta_{TE}$. This function is chosen as it already defines the general shape of an airfoil, as shown in Figure 8.2a.

The shape function $S(\psi)$ is a general function to uniquely define the geometry of the airfoil between the leading and trailing edge. Due to the class function this surface will have only one extreme on either side. The function creates a Bézier curve and is comprised of a Bernstein polynomial. A Bernstein basis polynomial of degree n can be obtained using Equation 8.3, where K_i is the binomial coefficient. The shape function can be controlled using the Bernstein coefficients A_i, which are the control point for the curve.

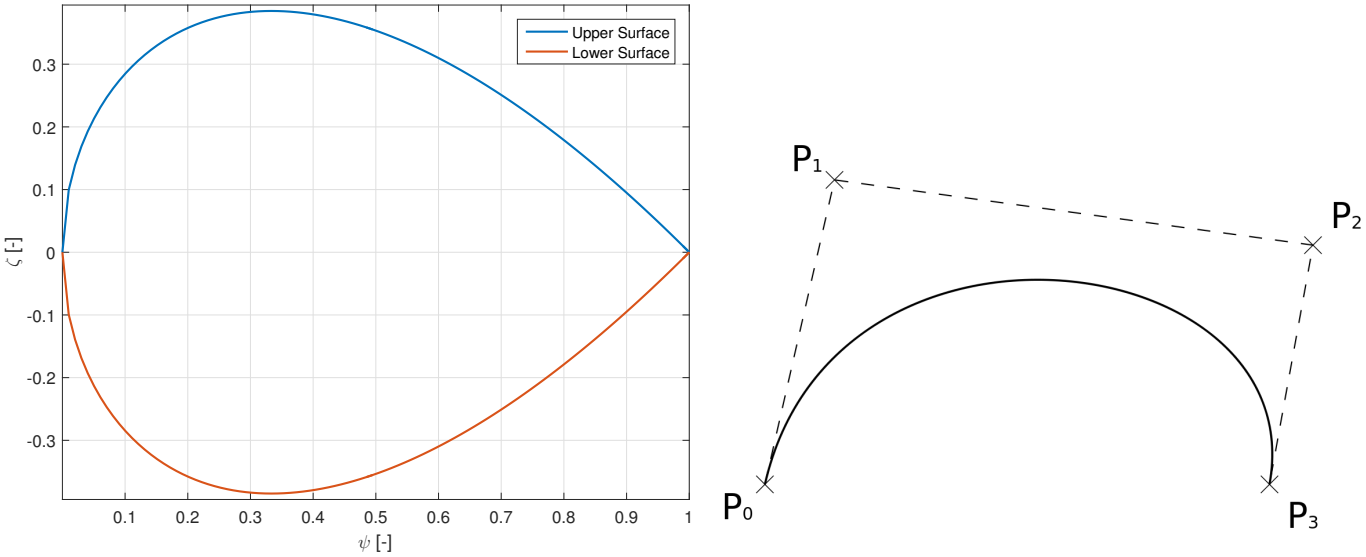

(a) Class function.

(b) Cubic Bézier curve controlled by control points P_i [2].

Figure 8.2: Class Shape Transform

Equation 8.4 shows how either the upper or the lower surface ($surf$) can be controlled. For example, Figure 8.2b shows how the coefficients of a cubic polynomial form a polygon which controls the curve.

$$K_i \equiv \binom{n}{i} = \frac{n!}{i!(n-i)!} \tag{8.2}$$

$$S_i(\psi) = K_i \psi_i (1-\psi)^{n-i} \tag{8.3}$$

$$S_{surf}(\psi) = A_{surf,i} \cdot S_i(\psi) \tag{8.4}$$

8.1.4 Constraints

Constraints are placed on the optimiser to prevent finding infeasible and unusable solutions. The upper and lower surface of the airfoil are bounded, so their Bernstein coefficients are constrained as well. These bounds are created from the reference airfoil data set, and will result in feasible and manufacturable airfoils. The used constraints are shown in Figure 8.3, where the white area exists as the generated airfoil will always have to be thicker than that, and the overlapping area leaves freedom for the trailing edge.

The upper bounds had to be carefully chosen. It turned out that due to the altered surface velocities by the added rotation, the convergence of some airfoils was unstable. If the optimiser could have chosen any geometry, often a shape would have been produced which quickly developed instabilities in the boundary layer. Whenever such a solution could not converge, the optimiser had trouble neglecting this airfoil and continuing. This meant that the optimiser had to be shut down and no usable results were obtained. Therefore, it has been chosen to limit the freedom of the airfoil generation, and improve the chance of the optimiser finding converged solutions. The resulting constraints shown in the figure led to that the optimiser worked most of the times.

[2] As found on `https://en.wikipedia.org/wiki/File:Bezier_curve.svg`, visited on 06-10-2015.

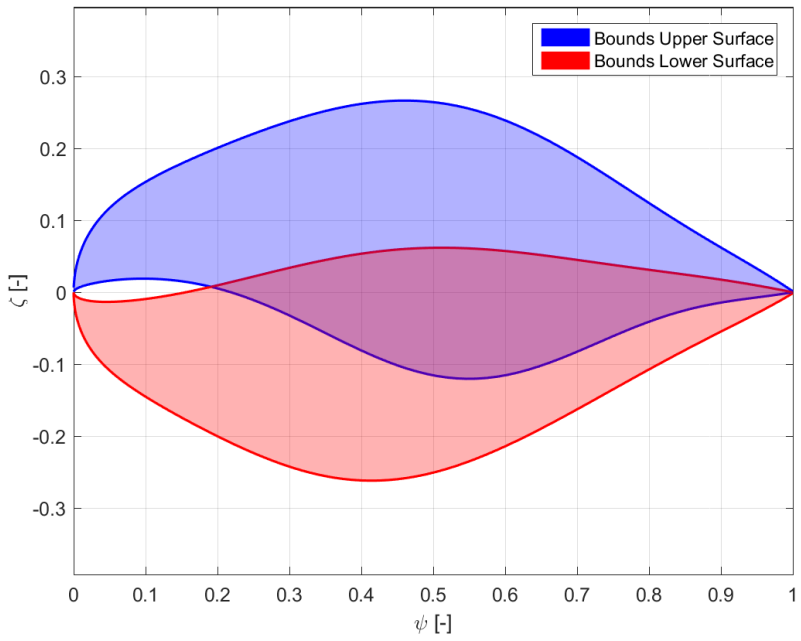

Figure 8.3: Upper and lower bounds for the upper and lower surface.

8.1.5 Optimisation Strategy

A thoughtful strategy must be adopted to clearly conclude the influence of the flow curvature effects. Obtaining the most useful results will make an analysis and comparison much easier afterwards. Therefore below the test cases are discussed which are used to produce the right outcomes.

The optimiser uses an 10th order Bernstein polynomial, so that there are 10 coefficients to control each surface. Adding a coefficient to control the trailing edge thickness, this leaves the optimiser with 21 free parameters. The optimiser is ran with a population size of 50 and a generation size of 5. In each population it will create 5 generations, where, just like breeding, each time the best solution remains. The reason why these numbers are so low is to diminish the chance of the optimiser trying an airfoil shape for which it cannot converge.

All cases will be ran at a Reynolds number of 1 million. This will ensure good convergence and as it is a proof of concept, this variable does not have to be investigated for its influence. Free transition on both the upper and lower surface is applied. Furthermore, the critical flow amplification factor N_{crit} is set to 6, which will mimic typical VAWT flow conditions. Lastly, all polars for each case are produced for a range of angle of attack of -15 to +15 degrees, with steps of 0.5 degrees. As has been encountered, this improves the chance of convergence, as the added surface velocities due to flow curvature alter the boundary layer, promoting stall at high angles.

Naturally, a benchmark case will be ran where the pitching rate is set to zero. The optimal airfoils for this case will be the ones to compare with. Then, to investigate whether flow curvature has effect, and if so, the impact of it, cases will be ran for pitching rates between 0.025 to 0.2 with steps of 0.025 rad/s. In this manner the flow curvature is gradually increased, making it possible to detect if there is a trend in the optimal airfoils.

As mentioned before, a chord-to-radius ratio and therefore a pitch rate of 0.2 is quite high. Simão Ferreira and Geurts [37] and Ragni et al. [55] used more common ratios for their research, where the highest is not even 0.1. Also, Kirke [11] mentions that typical VAWTs have a $\frac{c}{R}$ of up to 0.2. This means that investigating the results for a pitch rate of 0.2 rad/s will show the behaviour at its extreme, and that for common applications less influence of flow curvature can be expected. However, exotic turbines are investigated having larger chord-to-radius ratio's. Van de Wiel [56] shows the optimisation of a high solidity VAWT, having a chord-to-radius ratio of 0.33, which is "three to four times larger than in common vertical axis wind turbines."

Lastly, the pitching location is varied between $0.25c$ and $0.5c$. These are two mounting locations which are used in practice. As shown, these affect the streamfunction formulation, and therefore have an effect on the XFOIL calculations. And also for the virtual airfoil transformations, this location clearly affected the virtual camber and angle of incidence. Therefore, this test case should prove whether this variation also affects the produced optimal airfoils.

8.2 Results

Finally, the results from the optimising campaign shall be discussed. A sample of the output airfoils is presented, and their aerodynamic behaviour is reviewed. The results are also investigated as a function of pitching rate, which will determine what effect it has on airfoil design.

8.2.1 Airfoils

On average each simulation case produced 18 airfoils. These were the best performing airfoils of the tested datasets, being evaluated for the two objective functions. The optimiser gave them a score for either functions, as can be seen in the Pareto front depicted in Figure 8.4a. This value is non-related to the airfoil geometry, and is merely an optimiser output. The figure shows that there is quite some divergence, which is also visible when all airfoils are shown together in Figure 8.4b.

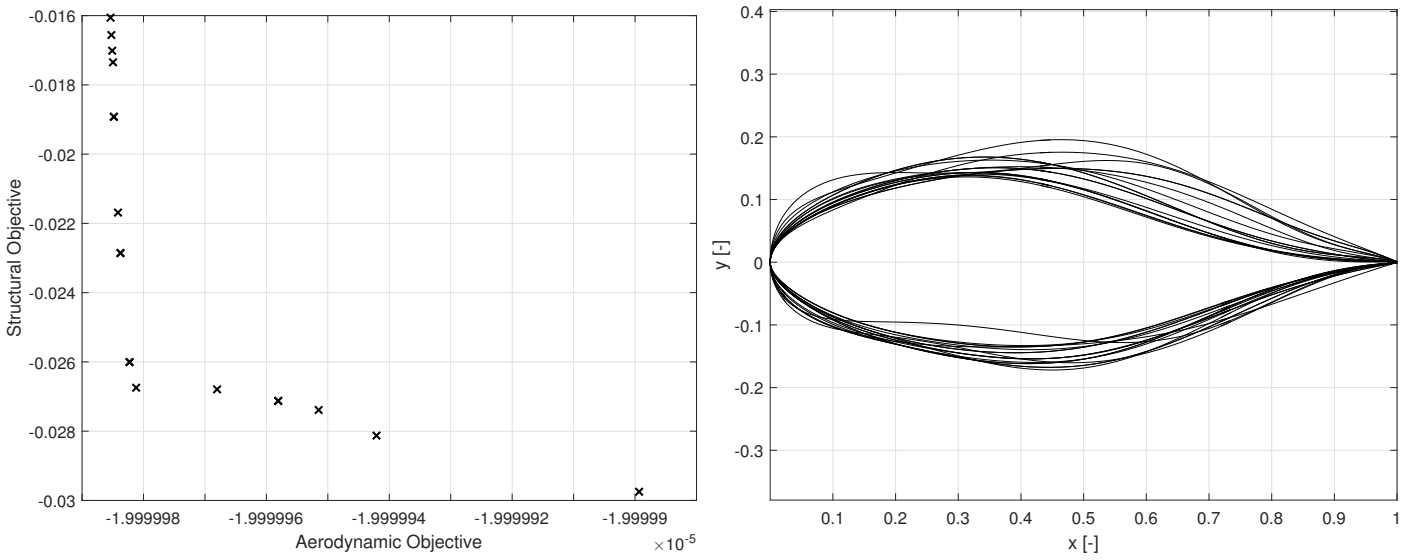

(a) Pareto front.

(b) All airfoils.

Figure 8.4: Optimiser output for the non-pitching case.

Of all these airfoils, the best aerodynamic performing airfoil is compared to the best structural performing one, both shown in Figure 8.5. For each airfoil, the camberline is shown, as well as the location of the maximum camber. The legend shows the values of maximum camber and thickness and their horizontal position. As can be seen, the aerodynamic airfoil is quite regular, having a thicker front part and a cusped trailing edge. The camber shows to be of higher order, but overall this is a feasible airfoil.

The structural airfoil is not however. Although it may score high on the structural objective, this is by no means an airfoil which could be used on a VAWT, as its is completely not aerodynamically shaped. However, it might still be useful to investigate flow curvature, as the variation of this shape with respect to pitching rate is of interest.

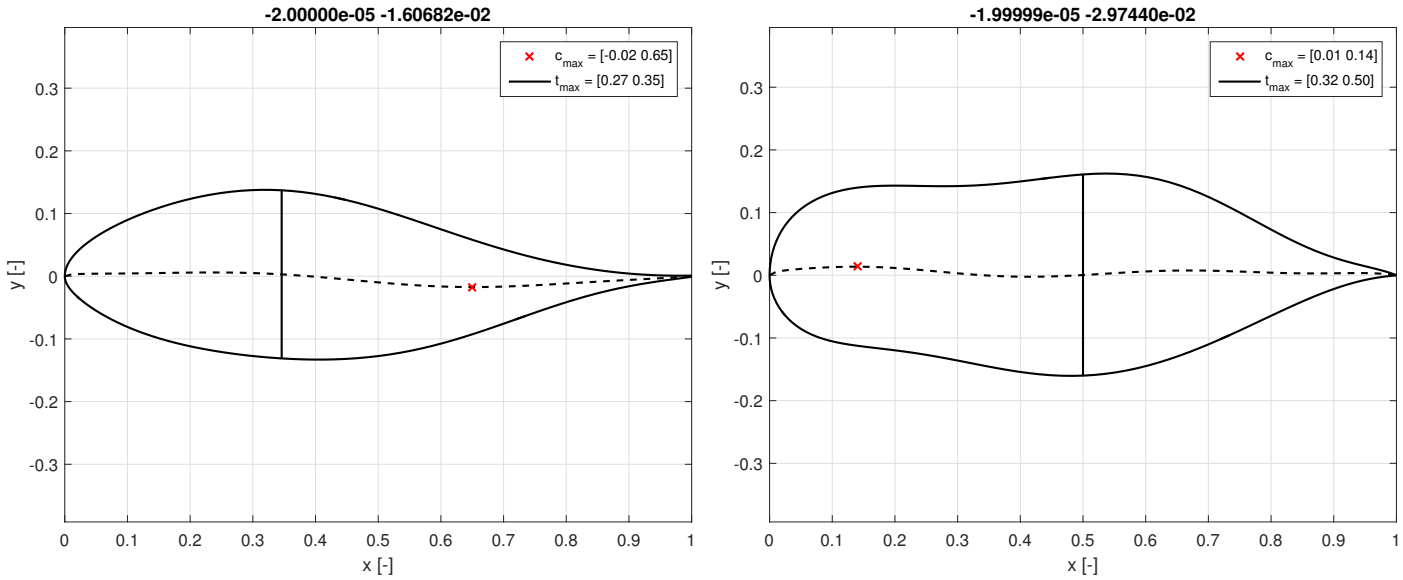

(a) Best aerodynamically.

(b) Best structurally.

Figure 8.5: Best performing airfoil for either objective, for the non-pitching case.

8.2.2 Variation of Pitch Rate and Location

The normalised geometrical parameters of either the aerodynamically or structurally best performing airfoils have been investigated as a function of pitch rate and pitching location. These variables are the maximum camber and its chord-wise position and the maximum thickness and its position. The results are shown in Figure 8.6 to Figure 8.10.

In every left plot (a) the geometric variables are shown for the best aerodynamic profile, in the other (b) for the structural one. For each of the parameters a regression line is plotted based on the least-squares method. This should show whether there is a trend in the data, after exclusion of any outliers. If the data is too scattered, the regression line is omitted. The non-pitching case is indicated with the filled circle.

The interpretation of these trends has to be done carefully, as not to make erroneous conclusions. Also, it has to be stressed that there is a certain aspect of randomness in the optimiser's result. As the Pareto set is so small, a trend is difficult to distinguish. Next to that, it may not be avoided that the optimiser finds local optima, leading to an even more indistinctive view.

With a larger set of optimal airfoils, one could say more conclusively that an airfoil is aerodynamically best. Comparing these airfoils for varying pitch-rate will likely result in less outliers or scattered data and a more clearly visible trend. But even then these airfoils could have been the results from a local optimum.

This means that the results below are only indicative. For all the results, the scale of the variation is marginal. Therefore, only the general regression of all the data is considered. This means no distinguishment shall be made between the results of varying pitch location.

Maximum Camber

The maximum camber for the most aerodynamic airfoils shows a trend for both pitching locations. The regression lines show that with increasing pitch rate the magnitude of the maximum camber increases. For the non-pitching case the maximum camber is larger than for almost all other pitching rates. As this is only a single data point, it can not be excluded that this is an outlier as well. The structural airfoil shows too much divergence in the data to conclude a trend. These airfoils are so complexly shaped, that their camber line is of higher order and therefore its maximum varies too much with increasing pitching rate.

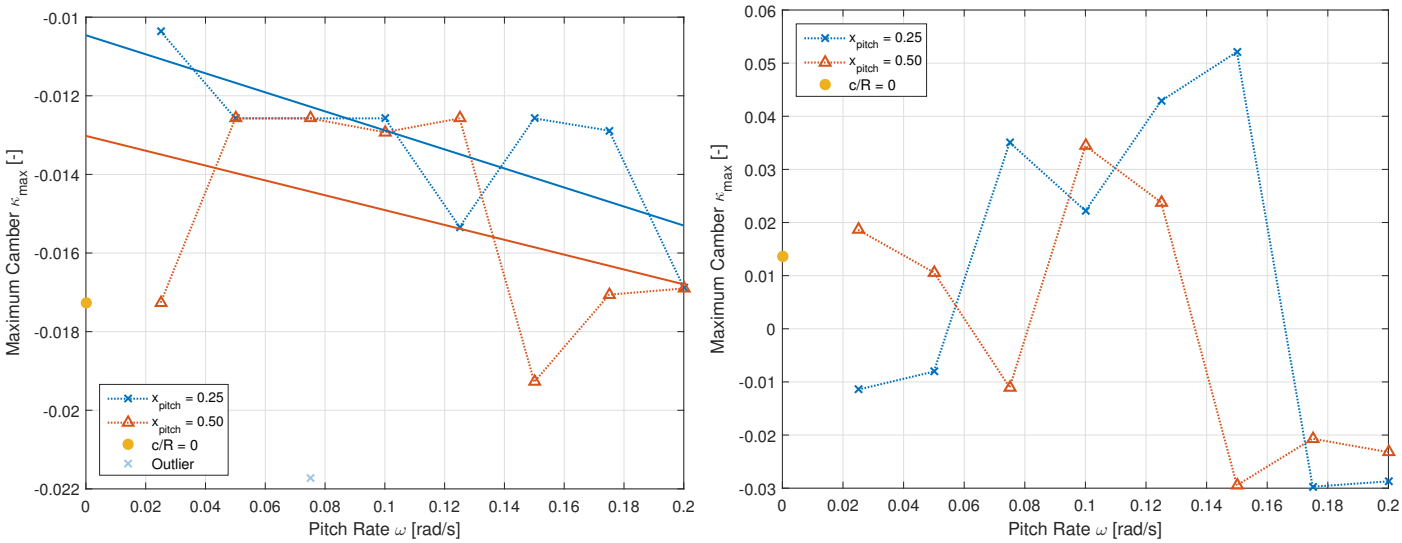

(a) Best aerodynamically.

(b) Best structurally.

Figure 8.6: Variation of maximum camber with varying pitching rate.

The results show that to account for an increasing effect of flow curvature, the aerodynamic profiles tend to have increased negative camber. During the optimisation process airfoils with positive camber would have shown earlier stall at common angles of attack, due to the increase of lift of the rotation. This would have resulted in a lower score for the aerodynamic objective, as the drag coefficient is in the denominator of the objective. Therefore, airfoils with more negative camber performed optimally for higher pitch rates.

As shown in chapter 3, the positive camber of a VAWT airfoil, resulting from flow curvature, will likely result in a higher lift production in the upwind half of the rotation, and a decreased on in the downwind half. Adding to that, the increased wake of the upstroke and the 'bluff-body type wake' Benedict et al. [16] described, this will result in an asymmetric force distribution over the rotation.

Likely this will decrease the power output and energy conversion from the flow. Now, when applying a negatively cambered airfoil, flow curvature would 'bend' it back towards a more symmetric virtual airfoil. This will mitigate these phenomena and increase the power output from the turbine, just as the optimiser was instructed to do.

Position Maximum Camber

The position of the maximum camber shifts forward for the aerodynamic profiles. For both pitch locations the regression line seems to have the same slope. The non-pitching case could be lying at the start of the trend lines when an uncertainty is taken into account. Also for the structural airfoils a negative trend is visible. Moving the pitch location aft will result in a larger movement of the position of maximum camber. The non-pitching case seems to be an outlier, having its maximum camber really far forward.

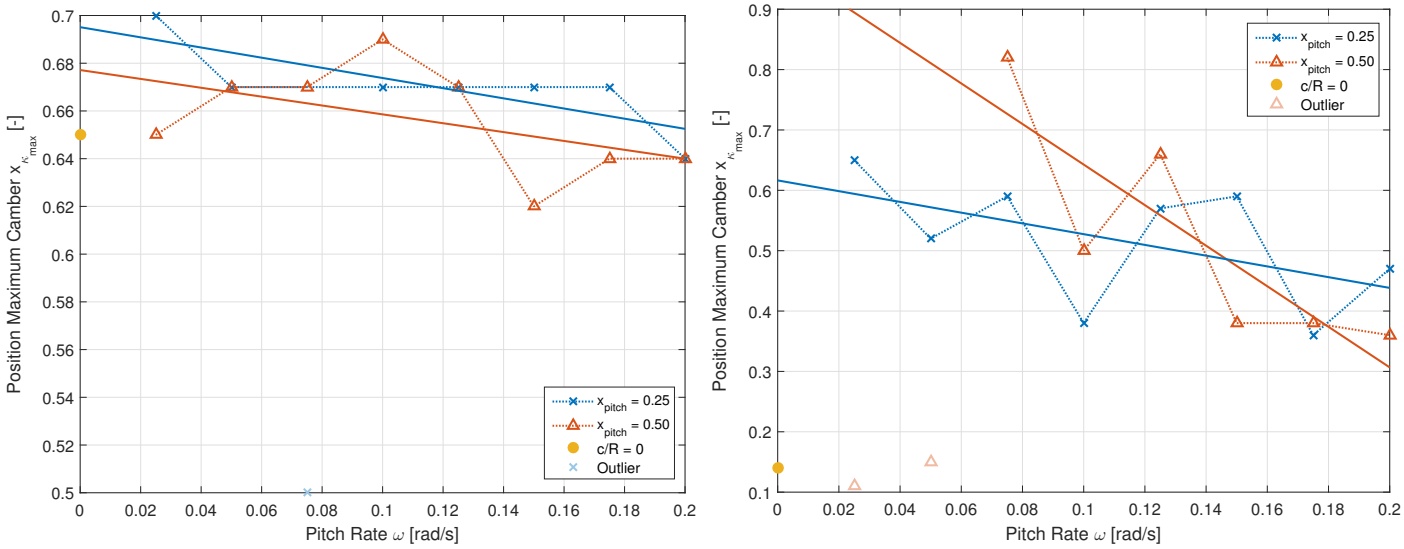

(a) Best aerodynamically.

(b) Best structurally.

Figure 8.7: Variation of position of maximum camber with varying pitching rate.

Using an quick test in XFOIL, the trends are explained as follows. Figure 8.8 shows what effect shifting the camber has on the lift over drag polar of the NACA 4-series, where the second number indicates the position of maximum camber in tenths of the chord. When the camber moves aft, the drag of the profile increases. At high angles of attack these profiles produce more lift, but as mentioned a filter weighs drag coefficient with the most common angles of attack. With a lower drag, a more optimal power production of the turbine is obtained, so the optimiser favours profiles with a more forward placed maximum camber. This results in the negative slope of the regression lines.

Maximum Thickness

The maximum thickness of the aerodynamic profiles decreases slightly when the pitch rate is increased. It seems to be unaffected by a shift of pitch location, and the non-pitching cases matches with the trend line within a margin. The structural data shows that their maximum thickness is unaffected by the pitch rate. The data for the pitch location at half the chord shows a large difference to those for $0.25c$ and a large spread. No conclusions can therefore be drawn about this dataset.

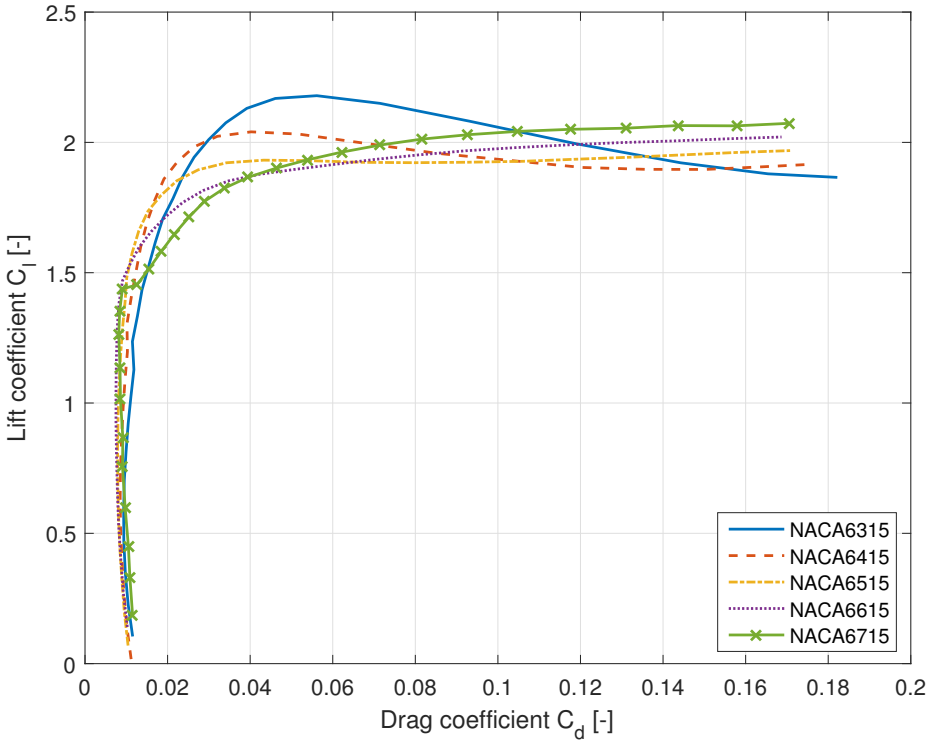

Figure 8.8: Lift over drag polar for some NACA 4-series airfoils, at a Reynolds number of 1 million, with a pitch rate of 0.2 rad/s and a pitch location at 025c.

Simão Ferreira and Geurts [37] explain that an increase of maximum thickness of the airfoil will increase the lift slope of an airfoil. This means that for the same range of angles of attack, thicker profiles are more likely to stall, leading to a lower score for the aerodynamic objectives. As flow curvature enhances the lift even further, thinner profiles will likely be more optimal. The data does not show clear enough whether changing the pitch location has any influence.

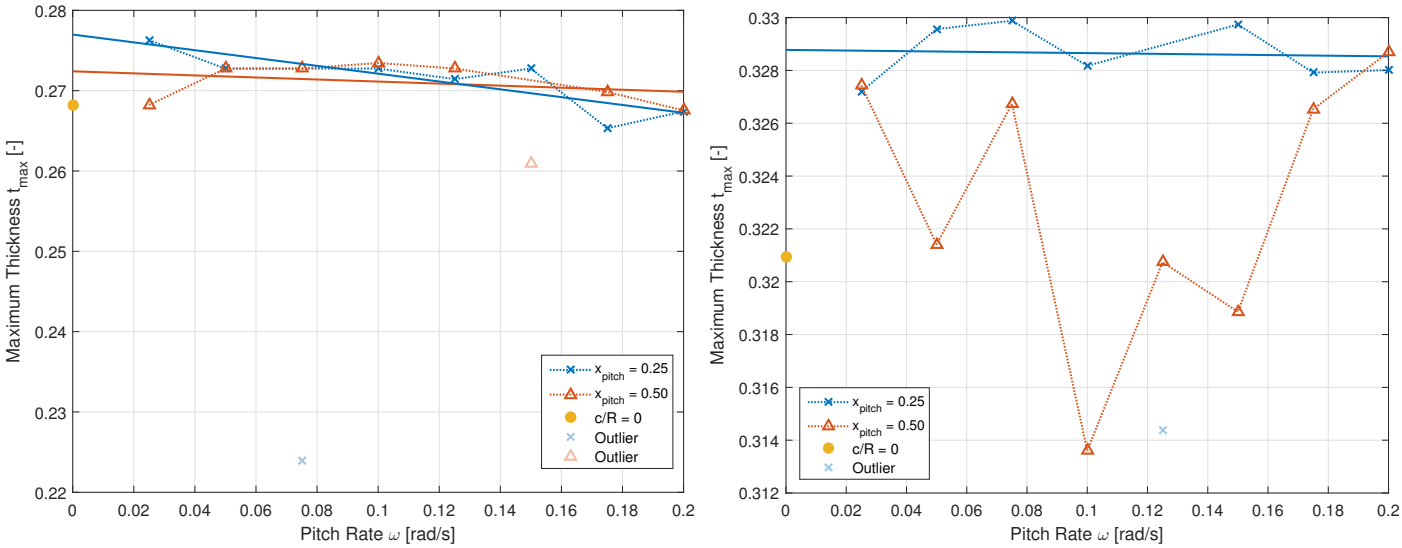

(a) Best aerodynamically.

(b) Best structurally.

Figure 8.9: Variation of maximum thickness with varying pitching rate.

Position Maximum Thickness

The data of the position of the maximum thickness shows a very large spread, but only over a small interval of about 5% of the mean value. As the non-pitching case is also close to these values, it can be concluded that this geometrical parameter is invariant to a change in pitch. The position of the maximum thickness of the structurally best airfoils moves aft with increasing pitch rate.

To show the effect of changing the position of maximum thickness, a small analysis has been performed using XFOIL. For a couple of symmetric NACA 6-series airfoil the lift versus drag polar has been computed at a Reynolds number of 1 million and a non-zero pitch rate. The classification of these airfoils shows the position of maximum thickness in tenths of the chord in the second number of the name of the airfoil. As can be seen in Figure 8.11, when moving the thickness aft, the boundary layer has an increased chance of separating due to the steep pressure gradient invoked by the larger gradient of the airfoil surface. This results in less lift and a higher drag at high angles.

This means that the airfoils with a forward position of maximum thickness produce higher lift, which is increased even more due to the flow curvature. These airfoils would show more undesired behaviour and the optimiser would have chosen airfoils with a lower lift over drag. This confirms the trend shown in Figure 8.10b.

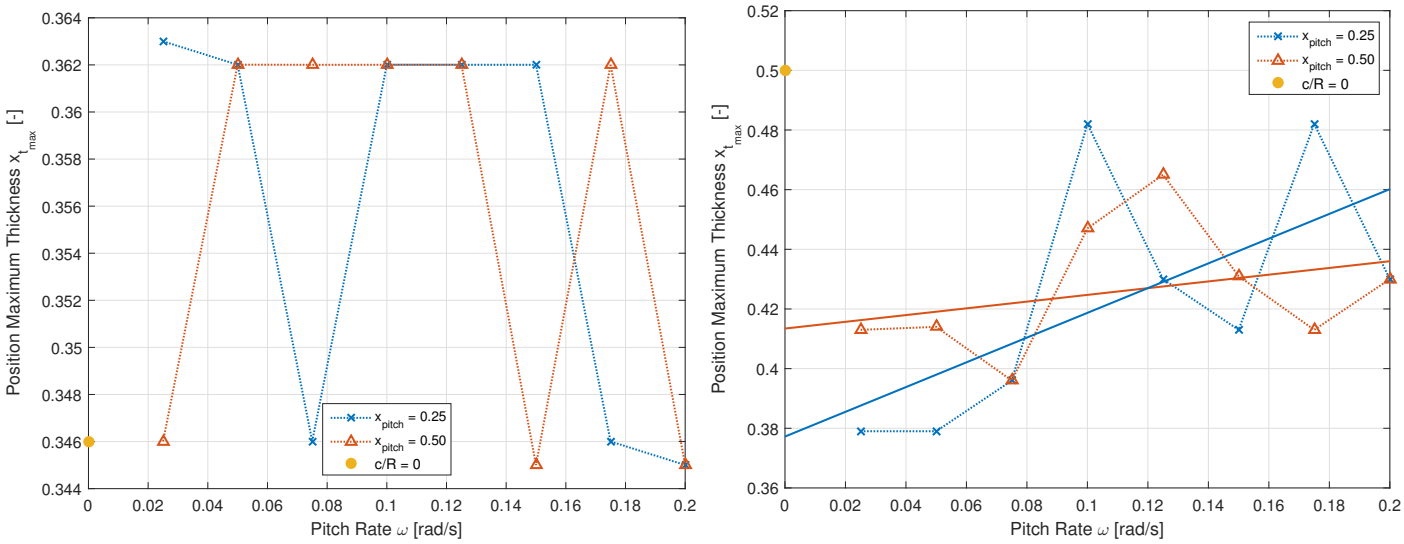

(a) Best aerodynamically.

(b) Best structurally.

Figure 8.10: Variation of position of maximum thickness with varying pitching rate.

8.2.3 Aerodynamic Performance

To investigate whether including flow curvature in airfoil design improves the performance of a VAWT, the following will discuss the aerodynamic behaviour of the optimal airfoils. The non-pitching aerodynamic optimal airfoil shall be compared with the two profiles for the high pitch rate of 0.2 rad/s. Their aerodynamic polars are compared below, and the turbine power output is investigated. To this extent, the airfoils are applied in a two-dimensional VAWT analysis code developed by Simão Ferreira [45], which shall be explained below.

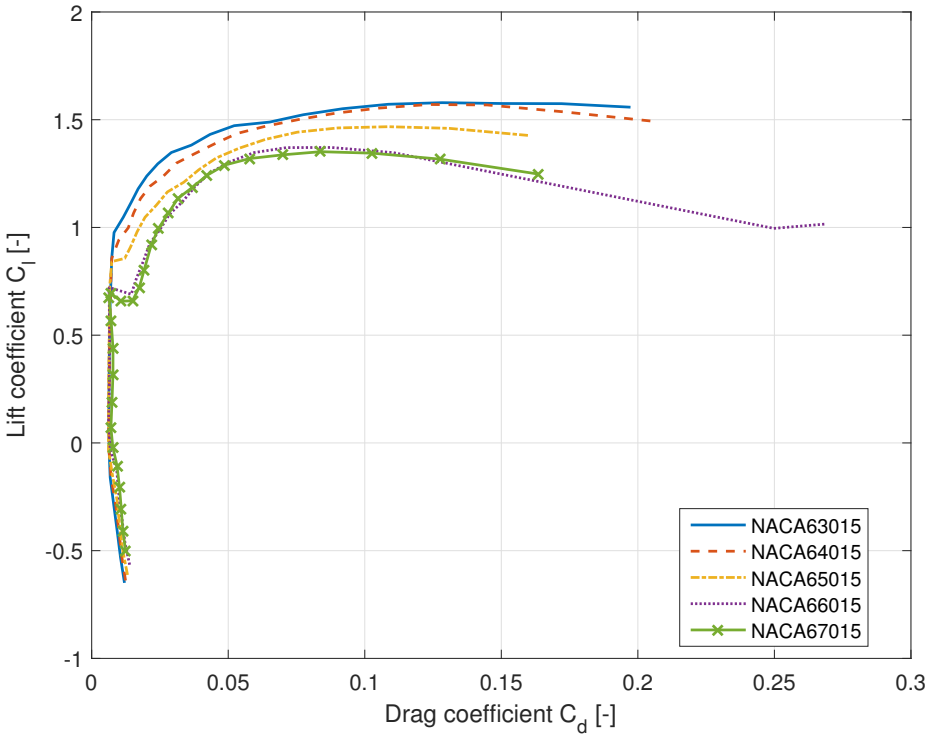

Figure 8.11: Lift over drag polar for some NACA 6-series airfoils, at a Reynolds number of 1 million, with a pitch rate of 0.2 rad/s and a pitch location at 025c.

Geometry

To more clearly explain the results below, the geometries of the three cases ($\frac{c}{R} = 0$; $\frac{c}{R} = 0.2, x_p = 0.25c$; $\frac{c}{R} = 0.2, x_p = 0.50c$) are shown in Figure 8.12. For clarification, they have been named using the following rule: AIR - CR (chord-to-radius ratio in hundredths) - XP (pitch location in hundredths of the chord). This gives the following optimised airfoils for the three cases respectively: AIR-CR00-XP00, AIR-CR20-XP25, and AIR-CR20-XP50.

As can be seen, it is very difficult to observe any differences. The optimisation process generated airfoil which are very similar. This could either be because it got stuck in a local optimum, or that the effect of flow curvature is not that severe. The non-pitching airfoil is slightly thicker, while the difference in camber cannot be seen.

Aerodynamic Polar

The optimal aerodynamic airfoils of the three cases are compared for their lift and drag in Figure 8.13. The polars are ran for their respective pitch rate of 0 and 0.2 rad/s, and their pitch locations.

Both pitching optimised airfoils produce more lift due to the added rotation of the airfoil. The most forward pitch location has a higher lift as the arm from the pitch location is longer to aft parts of the airfoil. Due to the impermeability boundary condition this results in a larger vorticity distribution and lift. These added rotational velocities also induce earlier stall compared to the non-pitching optimised airfoil.

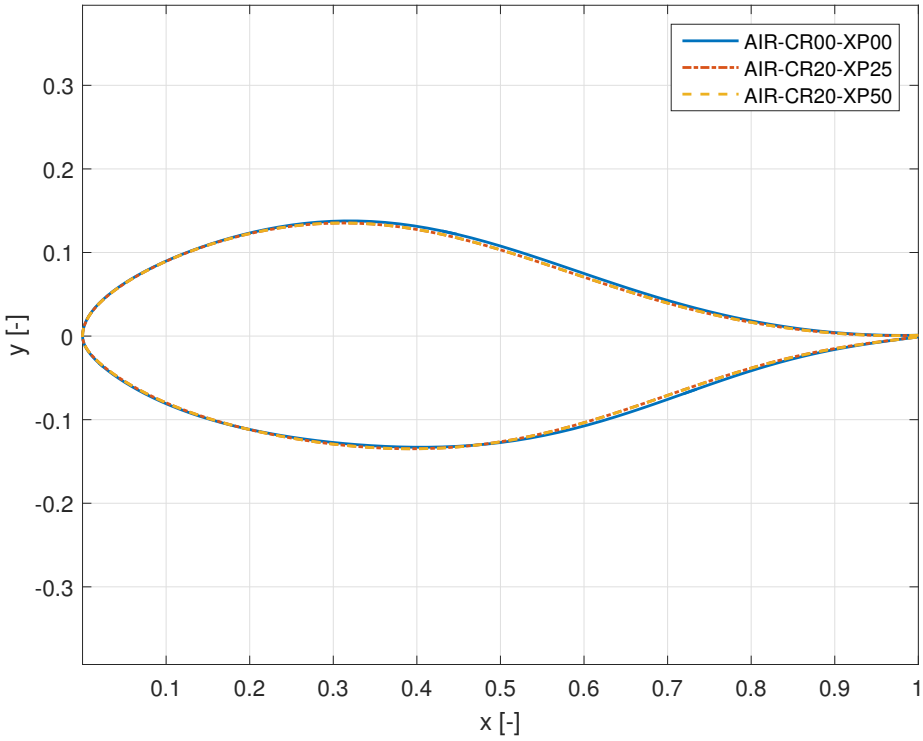

Figure 8.12: Optimal aerodynamic profiles for a pitch rate of 0 and 0.2 rad/s.

The shift in polar is also visible in the drag. The AIR-CR20-XP25 experiences earlier stall and therefore higher drag for large positive angles of attack. The AIR-CR20-XP50 airfoil is less affected, and shows a decrease of drag even. In the lift over drag polar this behaviour is summarised, showing more lift before stall in the upper left corner, but due to the increased camber also more drag for large negative angle of attack. This is also important as a VAWT airfoil encounters the whole range of angles.

Turbine Power

The power output of the turbine is obtained using an inviscid panel model, developed by Simão Ferreira [45]. As mentioned, the U2DIVA panel code from chapter 5 is the part of this model used to compute airfoil behaviour. The total model applied here contains a turbine with two blades, the rest of the turbine is not modelled. The wake is included when computing the turbine power.

For a simulation with a NACA0015 profile the angle of attack and velocity distribution are obtained, based on the induction and wake. As the inviscid code does not compute drag forces, these are the only usable parameters. These are in turn linked to XFOIL to retrieve viscous results.

As the simulation over a a range of solidity values of the turbine is only performed with a NACA0015 profile, the results are corrected when different airfoils are applied. This is done based on the fraction of the lift slope of the NACA over the optimised profile. This means that the inviscid results are now coupled with the viscous slope of the optimal airfoil. A correction is made when stall occurs, as the original NACA results are inviscid and do not take into account separation.

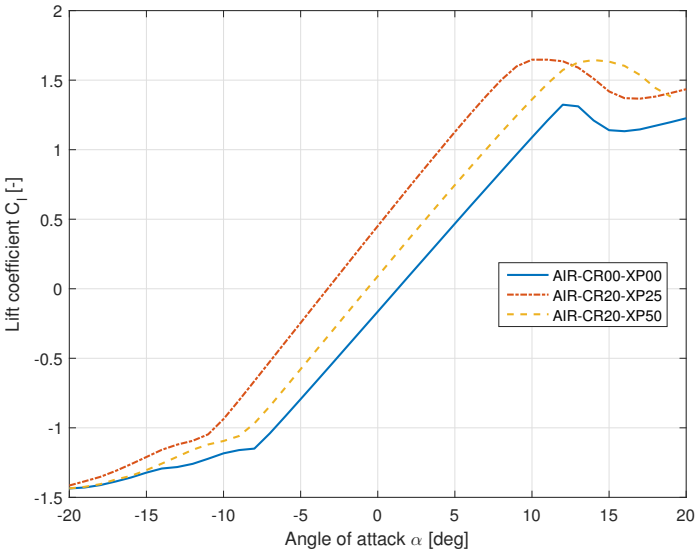

(a) Lift.

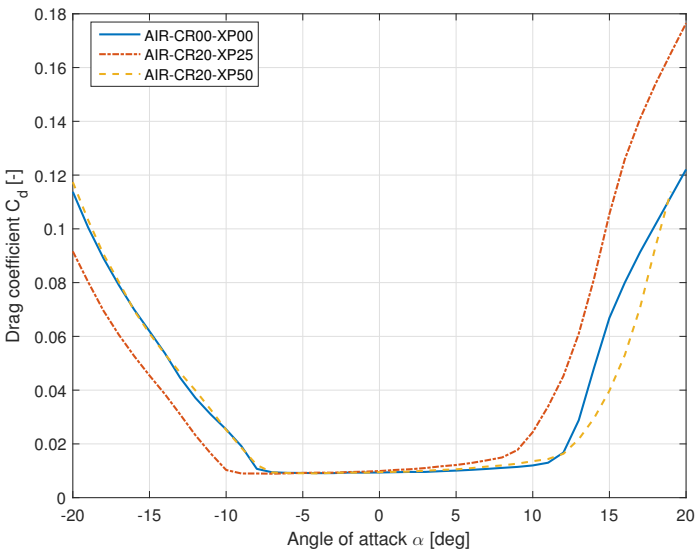

(b) Drag.

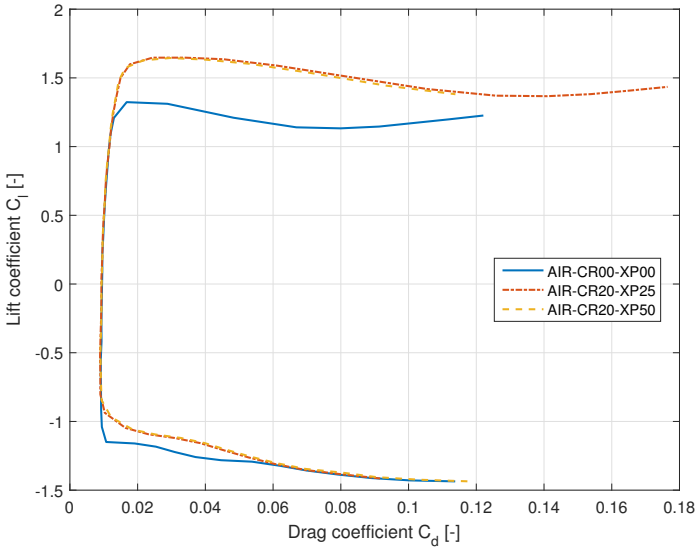

(c) Lift over drag.

Figure 8.13: Lift and drag polars for the three optimised profiles.

As there is a shift in the polars of the three airfoils, the code automatically search the most optimal angles of attack to run at. This is then implemented as a pitch setting of the airfoil, unique for each tip speed ratio. The resulting power coefficients are set out against the tip speed ratio in Figure 8.14. The plot shows that for lower tip speed ratios, up to about 5.5 the pitch optimised airfoils have increased power. Thereafter, the non-pitching optimised airfoil performs best.

At lower tip speed ratio, the performance is dominated by stall behaviour. The pitch optimised airfoil have smoother stall and higher lift coefficients. These could result in a higher power. But as stall is unpredictable, this cannot be said with certainty. In the high tip speed ratio region the AIR-CR00-XP00 airfoil seems to do better as it has slightly lower drag in the drag bucket in Figure 8.13b.

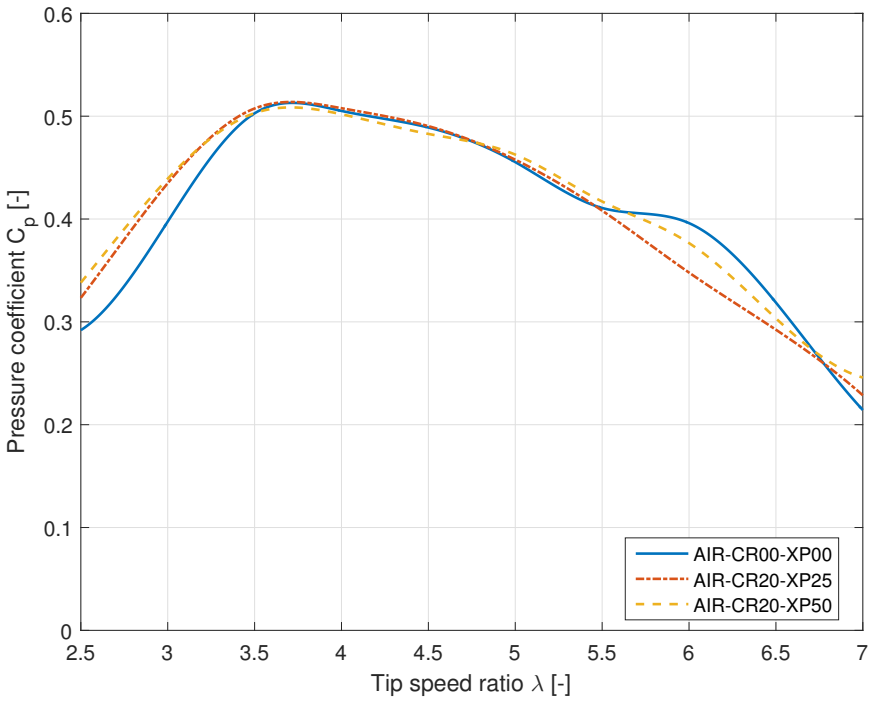

Figure 8.14: Pressure coefficient versus tip speed ratio of the most aerodynamic profiles of the non-pitching case and for a chord-to-radius ratio of 0.2 and either a pitch location at $0.25c$ or $0.5c$.

To show that including the flow curvature simulation in the airfoil optimisation process has merit, the non-pitching optimised airfoil AIR-CR00-XP00 is simulated with the same pitch rate as the other are optimised for. The results for the non-pitching optimised airfoil pitching around $0.25c$ are shown in Figure 8.15, the results for the other pitch location are similar. This shows that for tip speed between 3 and 5 the AIR-CR00-XP00 performs worse than the airfoil which has been optimised for this case. Afterwards their difference is very small. Also the AIR-CR00-XP00 simulated with a chord-to-radius ratio of 0.2 performs worse than the AIR-CR20-XP50 for high tip speed ratios. This means that including flow curvature could result in a small increase of turbine power.

Note that these optimisation cases are only ran for a chord-to-radius ratio of 0.2, so only for one turbine solidity value. To really evaluate the influence of the flow curvature model inclusion, the power optimisation code has to be ran for a range of solidities. This truly show the impact of the modified XFOIL code.

8.2.4 Virtual Airfoil Transformation

It would be interesting to see if the same optimal airfoils would have been obtained using one of the virtual airfoil transformations, applied on the airfoils of the non-pitching case. As has been shown that all of the transformations perform equal for a high value of 0.2 of the chord-to-radius, also the pitch rate. Therefore, in Figure 8.16 all the transformations are shown, applied on the optimal aerodynamic airfoil of the non-pitching case. Their maximum camber location is indicated with the marker. Also shown is the optimal airfoil for the situation where the pitch rate is 0.2 rad/s and the pitch location is at a quarter chord.

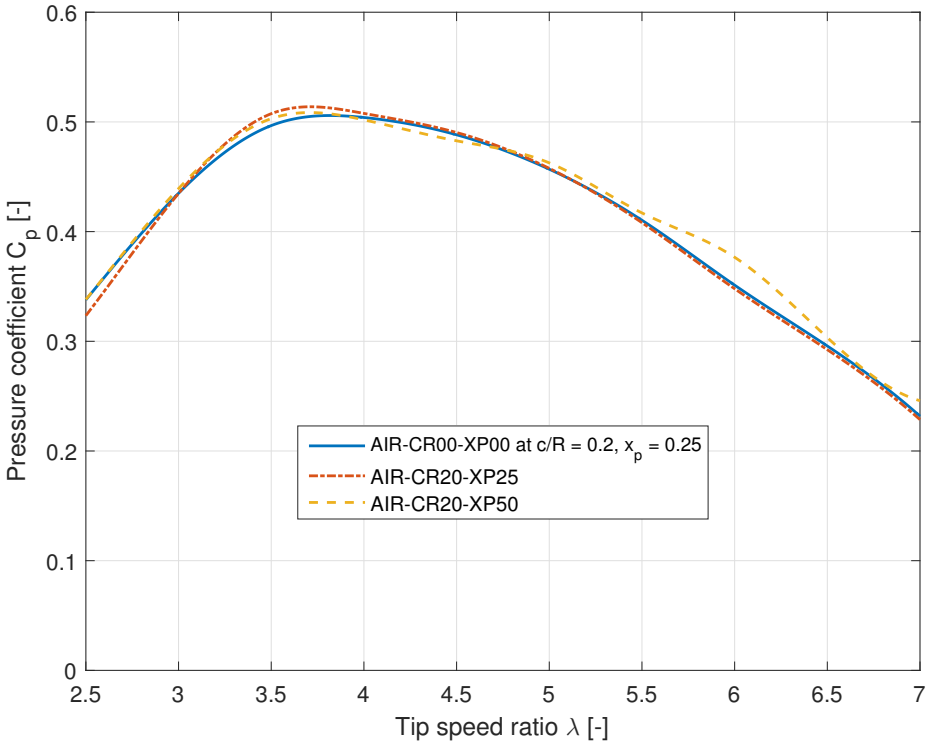

Figure 8.15: The power of all three airfoils simulated with a chord-to-radius ratio of 0.2.

What is seen is that the virtual airfoil transformations produce a much more drastic change. The camber of the airfoil is a lot higher and more forward than the airfoil with pitch rate. As all transformations are so similar, only the Migliore method shall be compared in its aerodynamic performance, it shall be named the AIR-CR00-XP00_VIRT airfoil.

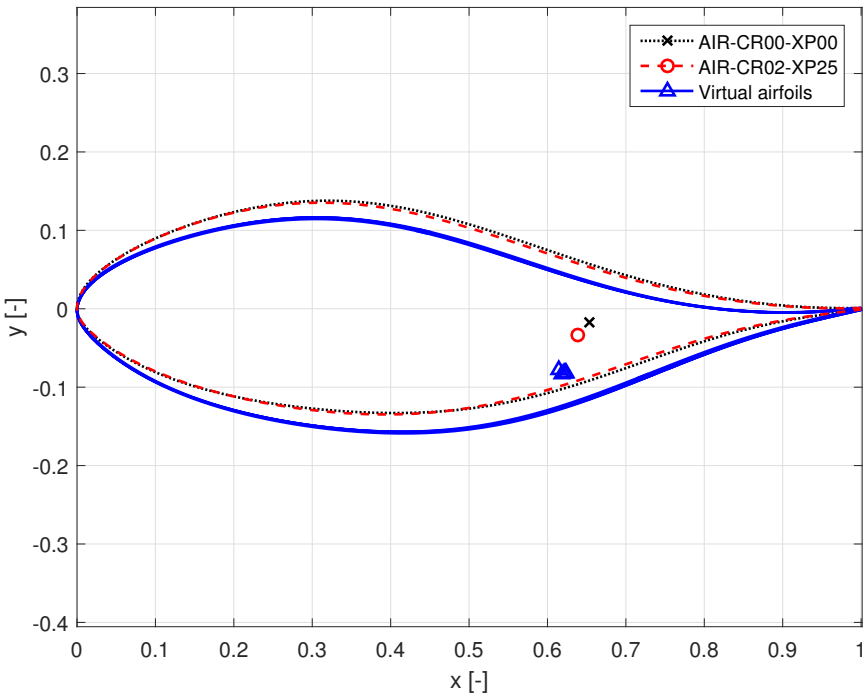

Figure 8.16: All virtual airfoil transformations applied on the non-pitching optimal airfoil, compared with the optimal airfoil for a pitch rate of 0.2 rad/s.

In Figure 8.17, the result this has on the lift and drag polars is a same shift to the left as the other pitch-optimised airfoils showed, reaching the same lift as to AIR-CR00-XP00 and slightly more for negative angles of attack. The drag is really comparable with the AIR-CR20-XP25, which is the case for which the virtual airfoil transformations were applied. The result this has for the power is seen in Figure 8.16.

Up to a tip speed ratio of about 3.8 the AIR-CR00-XP00_VIRT airfoil performs better than the non-pitching optimised airfoil, but worse than the other two. Thereafter it shows to produce the least amount of power. For low tip speed ratios the lift it produces is slightly more than of the AIR-CR00-XP00, for both high positive as high negative angles of attack. The same reasoning as before could be applied to explain the differences in power.

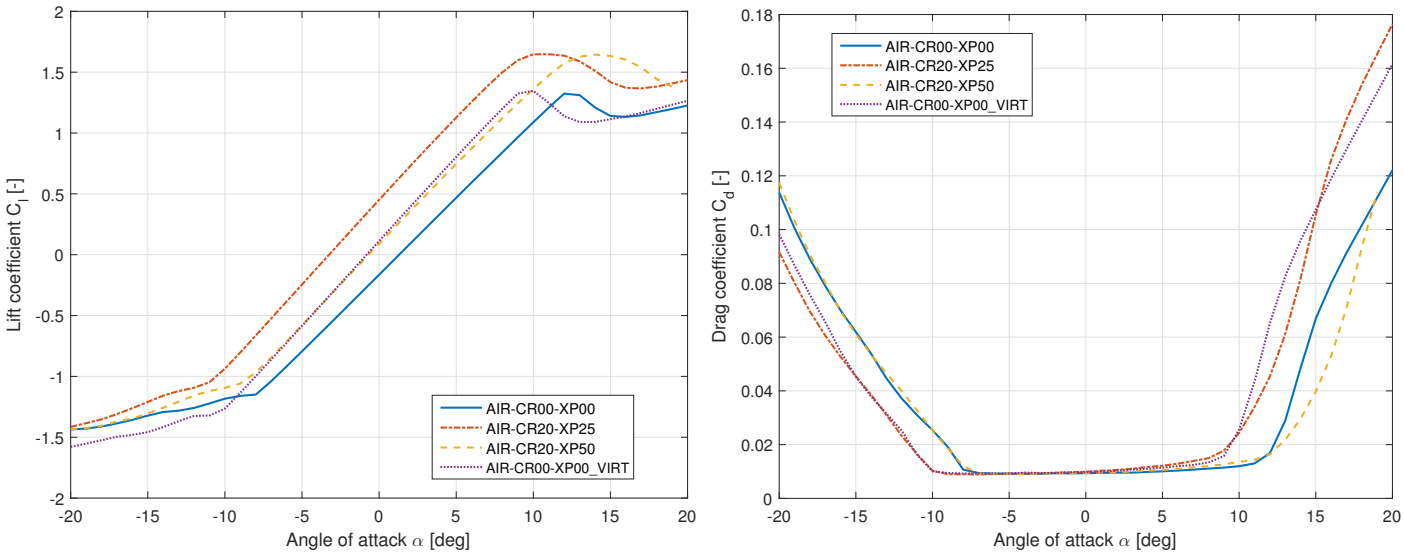

(a) Lift.

(b) Drag.

Figure 8.17: Lift and drag polars for the optimised airfoil and the AIR-CR00-XP00_VIRT airfoil.

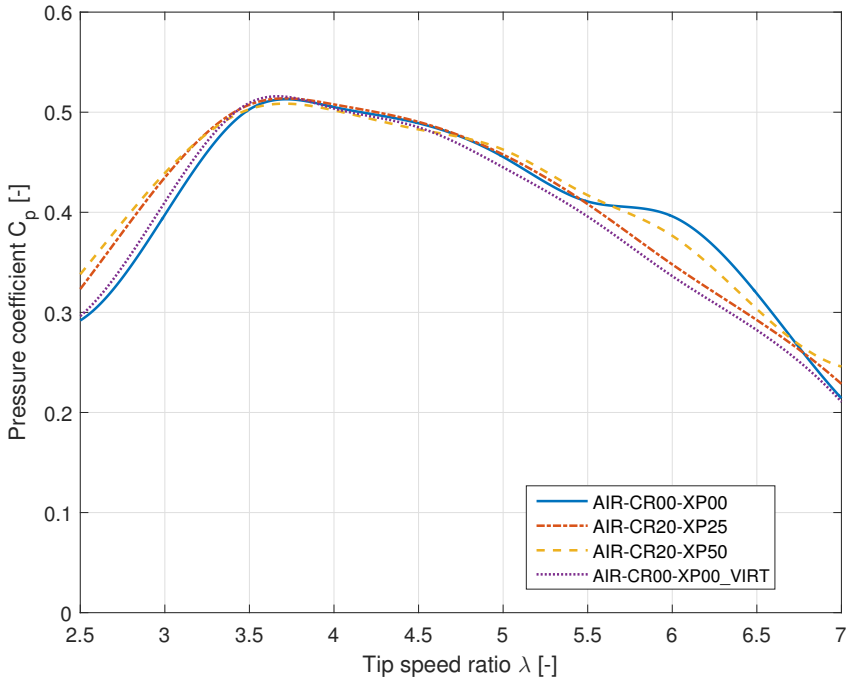

Figure 8.18: Power curve for the three optimised airfoils and the virtually transformed one.

8.3 Chapter Conclusions

- This chapter presented the results of an airfoil optimisation campaign, applying the Optiflow solver in various cases. This optimiser searches a set of optimised airfoils, weighing them on an aerodynamic and structural objective. The results showed reasonable aerodynamic best performing airfoils, and infeasible structural ones. However, all of them were scrutinised for a trend in their geometric variables when varying the pitch rate. With this analysis, the impact of flow curvature can be assessed on the design of the airfoils.
- Regression analysis showed that for the aerodynamic airfoils the maximum camber increased in magnitude and shifted forward. Due to extra lift due to flow curvature, more positively cambered airfoils will stall and therefore score bad on the aerodynamic objective. On top of that, aft camber will produce more drag, eventually leading to optimiser favouring more negatively cambered airfoils with forward camber.
- Thicker profiles with a forward position of their maximum have increased lift. When the pitch rate increases, these airfoils tend to stall, leading to not being optimal. Therefore, a trend is visible for thinner profiles, having their maximum thickness more aft, with increasing pitch rate.
- Furthermore, varying the pitch location showed that placing this more forward will decrease the lift coefficient. Together with the conclusions above, this will result in more positive, aft camber and more aft thickness.
- Finally, the turbine performance was checked by applying a two-dimensional inviscid panel method, including the wake, and coupled with viscous polars. For a high pitch rate of 0.2 rad/s, the optimised airfoils showed slight improvement over the non-pitching optimised airfoil. At low tip speed ratios an increase in produced power was obtained due to the improved stall behaviour of the pitch optimised airfoils. At higher ratios, the low drag of the AIR-CR00-XP00 airfoil resulted in better performance.
- When the AIR-CR00-XP00 was simulated with a pitch rate, slightly lower power was produced. This indicates that the pitch optimised airfoils actually worked as desired.
- The virtual airfoil transformation were applied on the AIR-CR00-XP00 airfoil to see if it could match the performance of the pitch optimised airfoil. As the transformation resulted in a more drastic airfoil, with increased camber, power increase was seen at low tip speed ratios. However, for most of the rest of the power plot it showed a little worse performance. It can therefore be said that it is a reasonable approximation, but not as well as optimising the airfoil.

Chapter 9

Conclusions and Recommendations

There still exists a large gap in maturity of technology and implementation between the vertical and the horizontal axis wind turbine today. The VAWT suffered from past presumed disadvantages, leading to it being underdeveloped. Better understanding of its aerodynamic behaviour and therefore airfoil design could stimulate research and development of this turbine. To that extent, this thesis investigated flow curvature effects. Possible mitigation of these could in the future lead to a larger proliferation of the VAWT.

This final chapter will present this thesis research' most important findings. As per chapter the largest conclusions are already discussed, the list below is merely a summary. These should provide a sufficient answer to these research question and goals posed in the introduction. Afterwards, recommendations for future research shall be presented, to stimulate research into this topic.

9.1 Conclusions

- **Flow Curvature** Flow curvature is the inherent phenomenon of an airfoil undergoing a rotation around the centre of a VAWT. In the airfoil reference frame, the encountered streamlines are curvilinear and will result in a variation of angle of attack over the chord.
  - The airfoil's rotation will add to its surface velocities, altering the pressure distribution. Centrifugal forces will alter the boundary layer.
  - Researchers have investigated airfoil sectional data and determined that the airfoil will behave as having added camber and angle of incidence due to flow curvature.
  - As a result, the azimuthal normal and tangential force distribution is altered, resulting in a change in torque and power. As the aerodynamic force distribution becomes more asymmetrical due to added virtual camber and incidence, the performance of the turbine decreases.

- **U2DIVA Panel Code** A source and doublet, inviscid, incompressible panel method has been applied and modified to accommodate a pitching airfoil.
  - Its steady solution is verified using an exact conformal mapping technique.
  - Its quasi-steady, pitching solution is verified using third party data. This data is not exact, but provides reasonable certainty.
  - It can be concluded that the U2DIVA panel code performs accurately.
- **Flow Curvature Models** Using a transformation to a virtual airfoil, having altered camber and angle of incidence, numerous authors have in the past tried to model flow curvature. This virtual airfoil for analysis purposes could be investigated in straight flow. Six methods have been applied and their results are compared.
  - All flow curvature models showed a reasonable correspondence to the solution of the U2DIVA panel code for the inviscid pressure distributions.
  - The viscous solutions showed a larger difference to the solution computed by the modified XFOIL. But as this solution is unverified, no conclusions can be drawn yet.
  - Also, no distinguishable differences between the models could be found when the chord-to-radius ratio and mounting location are kept with in practical bounds.
- **XFOIL** The XFOIL analysis software provides easy accessible tools to investigate airfoil behaviour. Its source code was modified to allow simulation of flow curvature.
  - By kinematically equation an airfoil in VAWT rotation and an airfoil rotating around its own axis, the chord-to-radius ratio could be varied in a pitching model by altering the pitch rate. This allows to investigate the impact of flow curvature.
  - The implementation required three modifications: a modification of the streamfunction formulation, to include the added velocities due to rotation; the computation of pressure is now based on induced velocities by an averaged linear vorticity distribution; and a change of reference frame is applied in the calculation of the pressure. A user defined pitch rate and -location can be accessed using the new PTCH-command.
  - These alterations ensured the pressure distribution to match very well with the U2DIVA panel code solution. The lift coefficient of both models differs below 10%.
  - The pitch rate, starting orientation of the airfoil, and geometry of the profile determine what effect the rotation has on the pressure distribution. Cambered profiles showed to be less influenced by flow curvature, as their pressure difference is already larger than of symmetrical profiles.
  - By changing the pitch location, the arm from the pitch axis to the surface is altered. When increasing the arm, the larger rotational velocities induce a larger pressure difference, so an increase in lift. However, it also results in an increased discrepancy between the benchmark solution.
- **Airfoil Optimisation** Using the Optiflow airfoil optimiser, a set of optimal airfoils has been investigated in their behaviour for varying pitch rate. This will show whether geometrical parameters such as camber and thickness are dependent on flow curvature.
  - The maximum camber of the optimised airfoils increases in magnitude and shifts forward with increasing pitch rate. During the optimisation process these airfoils did not stall sooner due to the increased lift of the pitching.

- Thinner profiles having their thickness more aft are also favoured by the optimiser due to the same reason.
- Shifting the pitch location forward will reduce the lift of the pitching airfoil, resulting in that the optimal ones show more positive camber, and placed more aft.
- By applying a two-dimensional VAWT analysis code the power output of the turbine could be computed. Little improvement was obtained by using the pitch optimised airfoils. Some power increase could be obtained at lower tip speed ratios, having to give in some power at higher ratios.
- The pitch optimised airfoil did show better results when they were compared to the non-pitching optimised airfoil with the same pitch rate. This shows that the inclusion of flow curvature effects in XFOIL has merit. This is consequently beneficial for the optimisation and therefore airfoil designfor vertical axis wind turbines.
- Lastly, the virtual airfoil transformations were applied to check whether they would result in the same airfoil as the pitch optimised one. The transformations turned out to be too drastic, modifying the camber too much. By simulating it with a pitch rate, slightly worse performance was found than the non-pitching optimised airfoil and both the pitch optimised airfoils. However, the difference is small and therefore the transformations show to be a reasonable approximation.

9.2 Recommendations

Finally, this last section will discuss some recommendations for continuation of this research. As has been shown, implementing correct modelling of flow curvature does have impact on airfoil design and likely beneficial results on the VAWT efficiency and performance. Therefore, it is essential that the results of this thesis are continued and applied in future research. The list of recommendations below, could kick-start and streamline future work.

- **Flow Curvature Models For Extreme Values** All six virtual airfoil transformations showed very good correspondence to the U2DIVA panel code results, when the free parameters are kept within their reasonable bounds. These include the chord-to-radius ratio, mounting location, and angle of attack. It has been chosen not to only perform an analysis when these variables have impractical values. However, it could be possible that for a specific application any of these variables is chosen outside of the applied bounds. As explained, the pressure distributions of the different methods will then start to vary and also become less accurate. In this case, a tailored analysis has to be performed to find the most suitable virtual airfoil transformation, as some of them might not produce accurate results.
- **XFOIL - Pressure Calculation** Currently, the XFOIL pressure calculation employs a change in the streamfunction formulation, a pressure calculation in the rotating reference frame, and the use of induced velocities near the surface. The linear vorticity distribution is averaged over a panel to obtain a constant one, in order to apply the latter. This could be improved, as there is a loss of accuracy when this is done. By applying the induced velocity equations of a linear vorticity distribution, the solution could be improved. One might even want to investigate if there is an easier way to compute the correct surface velocities, as this manner is more computationally expensive than the original method.

- **XFOIL - Own Code** The XFOIL source code is a maze of used or unused subroutines, commented lines, circuitous renaming of parameters, hundreds and hundreds of lines of code, and just general confusion. Next to that, XFOIL is almost like a black-box, as it is difficult to output or control variables. Also, the compilation of the source code and adaptability with the modern compiling methods and the airfoil optimiser were fairly difficult. And that while the necessary lines of code are only a couple hundred. This naturally does not include all the other splendid functions XFOIL provides, but those are not applicable in many researches.

  Therefore, the original XFOIL equations were already distilled and converted to Matlab, to provide easier viewing and controlling of the variables and manipulation and investigation of the outcomes. The results of this code were not a hundred percent identical to XFOIL's own results, but it sufficed well enough. It is therefore recommended to put in slightly more effort and do the same, reproduce the essential equations and functionalities in one's own preferred language. This makes the usage and production of results so much easier. In the end, modified equations could be translated to FORTRAN or the XFOIL software could just be neglected in total. One could recreate their own panel method, and have it be much more flexible and manageable.

- **XFOIL - Viscous Verification** The inviscid results of the modified version of XFOIL were shown to reasonably approximate the U2DIVA panel code. However, the viscous solution remains unverified and it can therefore not be assumed those results are completely accurate. It is unlikely, but the alteration of the inviscid solution might have had unwanted effects on the validity of the viscous equations. It is recommended to use an external, verified panel code or calculation method as CFD to determine the accuracy of XFOIL's viscous solutions.

- **Stability Airfoil Optimiser** The modified XFOIL software showed problems with converging to a viscous solution for airfoil shapes which are uncommon. This is the effect of changing the surface velocities as a result of the added rotation. It is unclear where this instability arises and therefore it could not have been alleviated. This meant that the optimiser had trouble producing results as soon as it tried an extreme airfoil shape. There was a mechanism implemented where it would neglect this airfoil and continue, but in practice this did not always work and the whole simulation and its results had to be cancelled.

  It is recommended that this work-around to neglect unconverged solutions is made more stable and robust. This will provide the ability to safely try a large number of airfoil shapes, without the risk of the optimiser stalling. This would improve the analysis of the produced optimal airfoils. Then a higher number of generations can be used, which will result in a higher diversity of the airfoils.

  Also running the optimiser for cases of soiled airfoil by simulating roughness would improve the analysis. In this manner, a more realistic optimal airfoil could have been found.

- **Conformal Mapping** The conformal mapping technique by Benson [46] was thought to provide the excellent opportunity to verify the XFOIL results with. It should compute the analytical solution for steady and unsteady pressure distributions and aerodynamic coefficients. However, the equations turned out not to work accurately for unsteady situations. Therefore, it could not be applied to its full extent. Instead it could only serve as a verification for a method which could produce solutions in all desired cases, the U2DIVA panel code. However, as this is a numerical method, it can still contain small errors.

  It is recommended to implement the mentioned conformal transformation technique or a similar one. This will result in that the pressure distribution from the modified XFOIL can be compared with theoretical results.

Bibliography

[1] World Wind Energy Association, "2014 Half-year Report," 2014.

[2] J. Moccia, "European Wind Energy Association: Wind energy scenarios for 2020," 2014.

[3] J. Paquette and M. Barone, "Innovative Offshore Vertical-Axis Wind Turbine Rotor Project," Sandia National Laboratories, Tech. Rep., 2012.

[4] H. Akimoto, K. Tanaka, and K. Uzawa, "Floating axis wind turbines for offshore power generation - a conceptual study," *Environmental Research Letters*, vol. 044017, no. 6, p. 6, 2011.

[5] H. J. Sutherland, D. E. Berg, and T. D. Ashwill, "A Retrospective of VAWT Technology," *Security*, no. January, 2012.

[6] P. Migliore and W. Wolfe, "Some Effects of Flow Curvature on the Performance of Darrieus Wind Turbines," Department of Aerospace Engineering West Virginia University, New Orleans, Tech. Rep., 1979.

[7] A. Zervos, "Aerodynamic Evaluation of Blade Profiles for Vertical Axis Wind Turbines," in *European Community Wind Energy Conference*, Herning, Denmark, 1988, pp. 611–616.

[8] M. Drela, "XFOIL: An Analysis and Design System for Low Reynolds Number Airfoils," *Lecture Notes in Engineering*, vol. 54, pp. 1–12, 1989.

[9] D. R. Hill, "Mechanical Engineering in the Medieval Near East," *Scientific American*, vol. 264, no. 5, pp. 100–105, 1991.

[10] Shikha, T. Bhatti, and D. Kothari, "Early development of modern vertical and horizontal axis wind turbines: A review," *Wind Engineering*, vol. 29, no. 3, pp. 287–300, 2005. [Online]. Available: http://dx.doi.org/10.1260/030952405774354859

[11] B. K. Kirke, "Evaluation of Self-Starting Vertical Axis Wind Turbines for Stand-Alone Applications," Ph.D. dissertation, Griffith University Gold Coast Campus, 1998.

[12] S. Savonius, "Rotor Adapted to Be Driven by Wind or Flowing Water," 1929.

[13] M. Islam, D. S. K. Ting, and A. Fartaj, "Aerodynamic models for Darrieus-type straight-bladed vertical axis wind turbines," *Renewable and Sustainable Energy Reviews*, vol. 12, no. 4, pp. 1087–1109, 2008.

[14] G. J. M. Darrieus, "Turbine Having Its Rotating Shaft Transverse to the Flow of the Current," 1931.

[15] T. D. Ashwill and T. M. Leonard, "Developments in Blade Shape Design for a Darrieus Vertical Axis Wind Turbine," no. September, p. 94550, 1986.

[16] M. Benedict, V. Lakshminarayan, J. Pino, and I. Chopra, "Fundamental Understanding of the Physics of a Small-Scale Vertical Axis Wind Turbine with Dynamic Blade Pitching: An Experimental and Computational Approach," in *54th AIAA/ASME/ASCE/AHS/ASC Structures, Structural Dynamics, and Materials Conference*, Boston, Massachusetts, 2013, pp. 1–21. [Online]. Available: http://arc.aiaa.org/doi/pdf/10.2514/6.2013-1553

[17] S. Mertens, G. van Kuik, and G. van Bussel, "Performance of an H-Darrieus in the Skewed Flow on a Roof," *Journal of Solar Energy Engineering*, vol. 125, no. 4, pp. 433–440, 2003. [Online]. Available: http://solarenergyengineering.asmedigitalcollection.asme.org/article.aspx?articleid=1456881

[18] M. Kinzel, Q. Mulligan, and J. O. Dabiri, "Energy exchange in an array of vertical-axis wind turbines," *Journal of Turbulence*, vol. 13, no. 38, pp. 1–13, 2012. [Online]. Available: http://www.tandfonline.com/doi/abs/10.1080/14685248.2012.712698

[19] C. J. Simão Ferreira, G. J. W. van Bussel, and G. a. M. van Kuik, "Wind Tunnel hotwire measurements, flow visualization and thrust measurement of a VAWT in skew," in *44th AIAA Aerospace Sciences Meeting and Exhibit*, Reno, Nevada, 2006.

[20] P. Deglaire, "Analytical Aerodynamic Simulation Tool for Vertical Axis Wind Turbines," Ph.D. dissertation, Uppsala University, 2010. [Online]. Available: http://urn.kb.se/resolve?urn=urn:nbn:se:uu:diva-132073

[21] S. Eriksson, H. Bernhoff, and M. Leijon, "Evaluation of different turbine concepts for wind power," *Renewable and Sustainable Energy Reviews*, vol. 12, no. 5, pp. 1419–1434, 2008.

[22] C. Simão Ferreira, G. Kuik, G. Bussel, and F. Scarano, "Visualization by PIV of dynamic stall on a vertical axis wind turbine," *Experiments in Fluids*, vol. 46, no. 1, pp. 97–108, 2009.

[23] H. Beri and Y. Yao, "Effect of Camber Airfoil on Self Starting of Vertical Axis Wind Turbine," pp. 302–312, 2011.

[24] P. G. Migliore, W. P. Wolfe, and J. B. Fanucci, "Flow Curvature Effects on Darrieus Turbine Blade Aerodynamics," *Journal of Energy*, vol. 4, no. 2, pp. 49–55, 1980.

[25] A. Goude, "Fluid Mechanics of Vertical Axis Turbines - Simulations and Model Development," Ph.D. dissertation, Uppsala University, 2012.

[26] J. D. J. Anderson, *Fundamentals of Aerodynamics*, 5th ed. New York: McGraw-Hill, 2011.

[27] M. C. Claessens, "The Design and Testing of Airfoils for Application in Small Vertical Axis Wind Turbines," Ph.D. dissertation, Technical University Delft, 2006.

[28] N. Fujisawa and S. Shibuya, "Observations of dynamic stall on Darrieus wind turbine blades," *Journal of Wind Engineering and Industrial Aerodynamics*, vol. 89, no. 2, pp. 201–214, 2001.

[29] M. Islam, R. Carriveau, and A. Fartaj, "Performance analyses of a fixed-pitch straight-bladed VAWT with selected low Reynolds number airfoils," *International Journal of Environmental Studies*, vol. 69, no. 2, pp. 289–298, 2012.

[30] P. Migliore and W. Wolfe, "The Effects of Flow Curvature on the Aerodynamics of Darrieus Wind Turbines," Department of Aerospace Engineering, Morgantown, West Virginia, Tech. Rep., 1980. [Online]. Available: http://adsabs.harvard.edu/abs/1980STIN...8115542M

[31] R. E. Sheldahl and P. C. Klimas, "Aerodynamic Characteristics of Seven Symmetrical Airfoil Sections Through 180-Degree Angle of Attack for Use in Aerodynamic Analysis of Vertical Axis Wind Turbines," Sandia National Laboratories, Albuquerque, New Mexico, Tech. Rep., 1981. [Online]. Available: http://onlinelibrary.wiley.com/doi/10.1002/cbdv.200490137/abstract$\delimiter"026E30F$nhttp://www.osti.gov/energycitations/product.biblio.jsp?osti{_}id=6548367

[32] M. Islam, D. S.-K. Ting, and A. Fartaj, "Desirable Airfoil Features for Smaller-Capacity Straight-Bladed VAWT," *Wind Engineering*, vol. 31, no. 3, pp. 165–196, 2009.

[33] M. Islam, M. R. Amin, R. Carriveau, and A. Fartaj, "Investigation of Low Reynolds Number Airfoils for Fixed- Pitch Straight-Bladed VAWT," no. January, pp. 1–9, 2009.

[34] T. J. Carrigan, B. H. Dennis, Z. X. Han, and B. P. Wang, "Aerodynamic Shape Optimization of a Vertical-Axis Wind Turbine Using Differential Evolution," *ISRN Renewable Energy*, vol. 2012, pp. 1–16, 2012.

[35] P. Migliore, "Comparison of NACA 6-Series and 4-Digit Airfoils for Darrieus Wind Turbine," *Journal of Energy*, vol. 7, no. 4, pp. 291–292, 1983.

[36] P. C. Klimas, "Tailored Airfoils for Vertical Axis Wind Turbines," Sandia National Laboratories, Albuquerque, New Mexico, Tech. Rep., 1992. [Online]. Available: http://cat.inist.fr/?aModele=afficheN{&}cpsidt=9090536

[37] C. Simão Ferreira and B. Geurts, "Aerofoil optimization for vertical-axis wind turbines," *Wind Energy*, vol. 18, pp. 1371–1385, 2015. [Online]. Available: http://onlinelibrary.wiley.com/doi/10.1002/we.1608/full

[38] J. Qu, Y. Mei, and M. Xu, "Investigation on Performance Influence of Maximum Thickness Position on Vertical Axis Wind Turbine Airfoil," *Asia-Pacific Power and Energy Engineering Conference, APPEEC*, 2011.

[39] J. Butbul, D. MacPhee, and A. Beyene, "The impact of inertial forces on morphing wind turbine blade in vertical axis configuration," *Energy Conversion and Management*, vol. 91, pp. 54–62, 2015. [Online]. Available: http://linkinghub.elsevier.com/retrieve/pii/S019689041400987X

[40] R. J. Muraca, M. V. Stephens, and J. R. Dagenhart, "Theorical Performance of Cross-Wind Axis Turbines With Results for a Catenary Vertical Axis Configuration," National Aeronautics and Space Administration, Hampton, Virginia, Tech. Rep. NASA TM-X-72662, 1975. [Online]. Available: http://ntrs.nasa.gov/archive/nasa/casi.ntrs.nasa.gov/19760003944{_}1976003944.pdf

[41] A. Zervos and R. Roucous, "Flow Curvature Effects on a Rotating Airfoil," *Journal of Applied Mathematics and Mechanics*, vol. 68, no. 5, pp. 365–368, 1988.

[42] A. Mandal and J. Burton, "The Effects Of Dynamic Stall and Flow Curvature on the Aerodynamics of Darrieus Turbines Applying the Cascade Model," *Wind Engineering*, vol. 18, no. 6, pp. 267–282, 1994.

[43] C. Hirsch and A. Mandal, "Flow Curvature Effect on Vertical Axis Darrieus Wind Turbine Having High Chord-Radius Ratio," in *European Wind Energy Conference*, Hamburg, 1984, pp. 405–410.

[44] A. C. Mandal and M. Q. Islam, "Flow Curvature Effect on Darrieus Wind Turbine with Blade Pitching," *RERIC International Energy Journal*, vol. 10, no. 2, pp. 61–73, 1988.

[45] C. J. Simão Ferreira, "The near wake of the VAWT 2D and 3D views of the VAWT aerodynamics," Ph.D. dissertation, Delft University of Technology, 2009.

[46] H. A. Benson, "Apparent-mass and on-board circulation of Joukowski airfoils and cascades in severe unsteady motion," Ph.D. dissertation, Massachusetts Institue of Technology, 1989.

[47] N. Ghodoosian, "Calculation of the Pressure Distribution on a Pitching Airfoil with Application to the Darrieus Rotor," Ph.D. dissertation, Oregon State University, 1983.

[48] H. Hirsch and A. Mandal, "A Cascade Theory for the Aerodynamic Performance of Darrieus Wind Turbines," *Wind Engineering*, vol. 11, no. 3, p. 12, 1987.

[49] P. Gregory, P. Joubert, and M. Chong, "Flow Over a Body of Revolution in a Steady Turn," DSTO Platforms Sciences Laboratory, Victoria, Australia, Tech. Rep., 2004.

[50] H. Akimoto, Y. Hara, T. Kawamura, T. Nakamura, and Y.-S. Lee, "A conformal mapping technique to correlate the rotating flow around a wing section of vertical axis wind turbine and an equivalent linear flow around a static wing," *Environmental Research Letters*, vol. 044040, no. 8, pp. 1–10, 2013. [Online]. Available: stacks.iop.org/ERL/8/044040

[51] G. de Oliveira, "Wind Turbine Airfoils with Boundary Layer Suction, a Novel Design Approach," Ph.D. dissertation, Delft University of Technology, 2011.

[52] J. Katz and A. Plotkin, *Low-Speed Aerodynamics*, 10th ed. Cambridge: Cambridge University Press, 2010.

[53] J. G. Leishman, *Principles of Helicopter Aerodynamics*, 1st ed. Cambridge: Cambridge University Press, 2000.

[54] B. M. Kulfan, "A Universal Parametric Geometry Representation Method - "CST"," in *45th AIAA Aerospace Sciences Meeting and Exhibit*, Reno, Nevada, 2007.

[55] D. Ragni, C. Simão Ferreira, and M. Barone, "Experimental and numerical investigation of an optimized airfoil for vertical axis wind turbines," no. January, pp. 1–10, 2014.

[56] J. van de Wiel, "Global and Aerodynamic Optimization of a High Solidity Mid-Size VAWT," Ph.D. dissertation, Delft University of Technology, 2015.

[57] C.-M. G. Lam, "Nonlinear Wake Evolution of Joukowski Aerofoils in Severe Maneuver," Ph.D. dissertation, Massachusetts Institute of Technology, 1989.

[58] S. a. Ansari, R. Å»bikowski, and K. Knowles, "Non-linear unsteady aerodynamic model for insect-like flapping wings in the hover. Part 1: methodology and analysis," *Proceedings of the Institution of Mechanical Engineers, Part G: Journal of Aerospace Engineering*, vol. 220, no. 2, pp. 61–83, 2006. [Online]. Available: http://pig.sagepub.com/lookup/doi/10.1243/09544100JAERO49

[59] L. Milne-Thomson, *Theoretical Aerodynamics*, 4th ed. New York: Dover Publications, Inc., 1958.

Appendices

Appendix A

Joukowski Conformal Transformation

This section will concern a special case of conformal mapping, the Joukowski transformation. This method, described by Benson [46], will provide an analytical solution to an airfoil's performance, which is perfect for verification purposes. The transformation will map a circle in the domain space to an airfoil in the image space, and has the useful feature that the potential flow is transformed with it. This means that solving for the complex potential flow problem for the airfoil is turned in to a far easier one for the circle. In this manner, an exact solution for the surface velocities, pressure distribution, and vorticity of the airfoil can be found.

A.1 Conformal Mapping

A conformal transformation transforms coordinates in the 'domain' to the 'image', as such that the local angles are preserved. An example is shown in Figure A.1. The transformation is conformal if and only if it is holomorphic and its derivative is non-zero everywhere on the to be transformed curve. Holomorphic means that complex functions are infinitely complex differentiable, and can therefore be exactly retrieved by their Taylor series expansion.

Regular points are those where the transformation is holomorphic, *singular* points are those where it is not. Regular points where the derivative of the transformation function is equal to zero are called *critical*, and at these points the local angle are not preserved through the mapping.

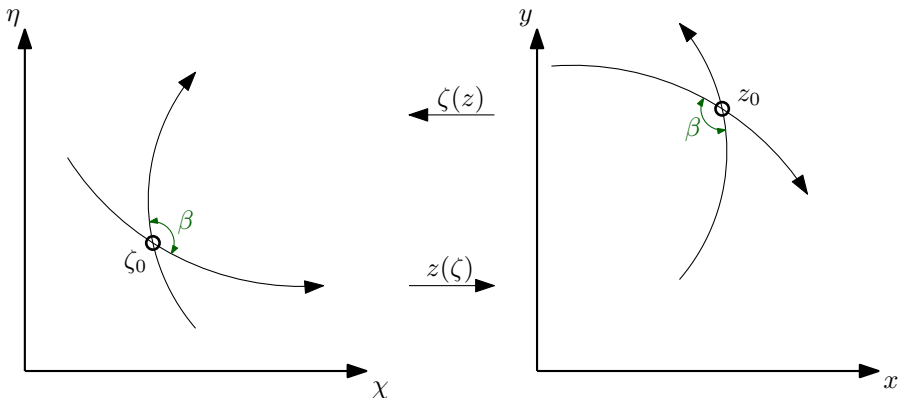

Figure A.1: Example of a conformal transformation, preserving angle β.

A.2 Potential Flow

Conformal mapping proves not only to be convenient to transform curves, but also has its applicability in potential flow. The following derivation, as found in Katz and Plotkin [52], will show why. A function of the complex variable $z = x + iy$ can be written in its real and imaginary parts, as in Equation A.1. For the function to be holomorphic this function must be differentiable in any direction, so Equation A.3 and Equation A.4 are both valid. As the derivatives must be independent of direction, they can be equated as in Equation A.5 and Equation A.6. These last two equations are called the Cauchy-Riemann conditions, and proves that a holomorphic function, such as the conformal transformation, satisfies the Laplace equation.

$$f(z) = g(x, y) + ih(x, y) \tag{A.1}$$

$$\frac{df(z)}{dz} = \lim_{\Delta z \to 0} \frac{f(z + \Delta z) - f(z)}{\Delta z} \tag{A.2}$$

$$\lim_{\Delta x \to 0} = \frac{\Delta g + i\Delta h}{\Delta x} = \frac{\partial g}{\partial x} + i\frac{\partial h}{\partial x} \tag{A.3}$$

$$\lim_{\Delta y \to 0} = \frac{\Delta g + i\Delta h}{\Delta iy} = \frac{\partial h}{\partial y} - i\frac{\partial g}{\partial y} \tag{A.4}$$

$$\frac{\partial g}{\partial x} = \frac{\partial h}{\partial y} \tag{A.5}$$

$$\frac{\partial g}{\partial y} = -\frac{\partial h}{\partial x} \tag{A.6}$$

This last result is very valuable, as now it is possible to exactly relate the flow around a circle in the domain space to the flow around an airfoil in the image space. A conformal transformation gives the possibility to transform a complex problem in the airfoil space into a simpler problem in the circle space. In this manner, the impermeability boundary condition only has to be applied to the circle, which therefore results in that only the circumferential velocity needs to be transformed.

The Cauchy-Riemann conditions depict the relation between the velocity potential and the streamfunction for potential flow, if they are the real and imaginary parts of a holomorphic function of complex variable F. This is called the complex potential, as shown in Equation A.9, and its derivative the complex velocity, Equation A.10.

$$\frac{\partial \Phi}{\partial x} = \frac{\partial \Psi}{\partial y} \tag{A.7}$$

$$\frac{\partial \Phi}{\partial y} = -\frac{\partial \Psi}{\partial x} \tag{A.8}$$

$$F = \Phi + i\Psi \tag{A.9}$$

$$W(z) = F' = u - iw \tag{A.10}$$

A.3 Joukowski Transformation

The following transformation, developed by McCune and co-workers, is proposed in [46, 57, 58], and shown in Equation A.11. Here the circle surface z is defined in polar coordinates by its radius R and azimuth angle θ. The airfoil surface ζ is adjusted using τ and σ, which are related to the thickness ratio and camber respectively.

$$\zeta(z) = z + \frac{A_1}{z} + \frac{A_2}{z^2}\ , \text{ where} \tag{A.11}$$
$$A_1 = R\left[R - (\tau - i\sigma)\right]$$
$$A_2 = \frac{1}{2}R^2(\tau - i\sigma)$$

An advantage to this transformation is that the same circle can be used to produce multiple Joukowski airfoils, keeping the centre at the origin of the coordinate system. The centre of the transformed airfoil will be at the origin of the image space. This also means that the trailing edge will always be at $z = R$, because, as mentioned, the derivative of the transformation is zero there, and therefore the angle will not be preserved. Another useful feature is that the freestream fields in both the spaces is kept equal in direction. Lastly, the necessity of having the centre at the origin will become clear later on, where the conjugate function theory is used to compute the airfoil velocities. It then will also be mentioned that the prerequisite is needed to uphold the Kutta condition at the trailing edge.

Before the transformation is applied, first its impact on the flow shall be shown. It can be imagined that an infinitesimal element of the airfoil surface is related through its derivative to an element on the circle surface, as in Equation A.12. Also, the Cauchy-Riemann relations show that the potential flow are also transformed, which results in a relation between the velocities on both bodies, in Equation A.13. Finally, through this relation, the airfoil normal and tangential velocity can be related to the radial and circumferential velocity on the circle, as shown in Equation A.14. This means that when the radial and tangential velocity of the surface are known, the airfoil velocities can easily be retrieved using the transformation derivative.

$$|\delta\zeta| = \left|\frac{d\zeta}{dz}\right| |\delta z| \tag{A.12}$$
$$\frac{F(\zeta)}{d\zeta} = \frac{df(z)}{dz}\frac{dz}{d\zeta} =$$
$$W(\zeta) = \omega(z)\frac{1}{\frac{d\zeta}{dz}} \tag{A.13}$$
$$v_n + iv_t = \frac{v_r - iv_\theta}{\left|\frac{d\zeta}{dz}\right|} \tag{A.14}$$

Now the problem of a pitching airfoil can be divided into two parts, the steady freestream solution, and the unsteady solution due to the rotation. The airfoil is represented by a continuous distribution of vortices on the surface. Due to the rules of potential flow these solutions can be add up to find the end results. There will be no shed vortices considered, as the wake of the airfoil is not taken into account.

A.3.1 Steady Solution

The steady freestream over a circle in two dimensions can be described by the potential in Equation A.15, as explained in section 3.11 of [52] or using the circle theorem in 5.2 of [59]. This equation differentiates to the complex velocity on the surface as in Equation A.16.

$$f(z) = U_\infty\left(ze^{-i\alpha} + \frac{R^2e^{i\alpha}}{z}\right) + \frac{\Gamma_0 \ln z}{2\pi i} \tag{A.15}$$
$$\omega(z) = \frac{d\Phi}{dz} = U_\infty\left(e^{-i\alpha} - \frac{R^2e^{i\alpha}}{z^2}\right) + \frac{\Gamma_0}{2\pi iz} \tag{A.16}$$

By applying polar coordinates, the tangential velocity in Equation A.18 can be found. The steady bound circulation can be found according to the Kutta condition. There are multiple ways of interpreting this condition, one is that it requires that the pressure difference at the trailing edge is zero. This means that for the circle, a stagnation point with a pressure coefficient of one is present. According to the steady Bernoulli equation in Equation A.19, this means that the tangential velocity has to be zero, as the radial velocity at the trailing edge is equal to zero over the entire surface. This can be confirmed by differentiating the potential. In the end, this results in a steady circulation as in Equation A.20. The same would have been achieved when the vorticity on the surface would have been integrated, which for inviscid flow is equal to the tangential velocity of the circle, as shown in Equation A.21.

$$v_r(\theta)|_{steady} = 0 \tag{A.17}$$

$$v_\theta|_{steady}(\theta) = -2U_\infty \sin(\theta - \alpha) + \frac{\Gamma_0}{2\pi R} \tag{A.18}$$

$$C_p = 1 - \frac{q^2}{U_\infty^2} = 1 - \frac{v_r^2 + v_\theta^2}{U_\infty^2} \tag{A.19}$$

$$\Gamma_0|_{steady} = -4\pi R U_\infty \sin\alpha \tag{A.20}$$

$$\gamma_0(\theta)|_{steady} = -2U_\infty[\sin(\theta - \alpha) + \sin(\alpha)] \tag{A.21}$$

The rules of the conformal transformation state that the circulation is directly transformed. This means that Γ_0 on the circle is also that on the airfoil. The negative sign results from the fact that a positive circulation is defined in the direction of increasing θ, and this circulation acts in clockwise manner.

A.3.2 Unsteady Solution

The unsteady motion is felt through an altered normal velocity on the airfoil. The surface vortices have to adapt their strength according to the movement, as to uphold the impermeability boundary condition. The result will always have to be that the normal velocity is zero, which is accomplished by equating the local fluid velocity to the local surface velocity. This results in Equation A.22 and Equation A.23. As the flow is inviscid, the no-slip boundary condition on the surface is not enforced.

$$u = \dot{l}\cos\alpha - \dot{h}\sin\alpha + \eta\dot{\alpha} \tag{A.22}$$

$$v = \dot{l}\sin\alpha + \dot{h}\cos\alpha - (\xi + a)\dot{\alpha} \tag{A.23}$$

To find the unsteady circulation, again the tangential velocity on the circle must be found, which will give the vorticity distribution. In order to find the imaginary component of the velocity, first the real part, the radial velocity, has to be found. This can be achieved by applying the transformation in Equation A.14 and a transformation from the polar coordinates to Cartesian ones. This results in Equation A.24, which can further be derived by using the substitution in Equation A.25. The zero-through-flow boundary condition only applies to the normal velocity, so only the real part of the final equation is considered, resulting finally in Equation A.27.

$$v_r - iv_\theta = (u - iv)e^{i\theta}\left|\frac{d\zeta}{dz}\right| \tag{A.24}$$

$$e^{i\theta}\left|\frac{d\zeta}{dz}\right| = A + iB \tag{A.25}$$

$$v_r = Au + Bv \text{ , where} \tag{A.26}$$

$$A = \frac{1}{R}[\tau(\cos\theta - \cos 2\theta) - \sigma(\sin\theta - \sin 2\theta)]$$

$$
\begin{aligned}
B &= \frac{1}{R}[2R\sin\theta - \tau(\sin\theta - \sin 2\theta) - \sigma(\cos\theta - \cos 2\theta)] \\
v_r(\theta)|_{unsteady} &= \frac{1}{R}(A_1\sin\theta + A_2\sin 2\theta + A_3\cos\theta + A_4\cos 2\theta \\
&\quad + A_5\sin^2\theta + A_6\cos^2\theta + A_7\sin\theta\cos\theta + A_8\sin\theta\sin 2\theta \\
&\quad + A_9\sin\theta\cos 2\theta + A_{10}\cos\theta\sin 2\theta + A_{11}\cos\theta\cos 2\theta)\ , \text{ where} \qquad \text{(A.27)} \\
A_1 &= -\sigma(\dot{l}\cos\alpha - \dot{h}\sin\alpha) + (2R-\tau)(\dot{l}\sin\alpha + \dot{h}\cos\alpha) + a(\tau - 2R)\dot{\alpha} \\
A_2 &= \sigma(\dot{l}\cos\alpha - \dot{h}\sin\alpha) + \tau(\dot{l}\sin\alpha + \dot{h}\cos\alpha) - a\tau\dot{\alpha} \\
A_3 &= \tau(\dot{l}\cos\alpha - \dot{h}\sin\alpha) - \sigma(\dot{l}\sin\alpha + \dot{h}\cos\alpha) + a\sigma\dot{\alpha} \\
A_4 &= -\tau(\dot{l}\cos\alpha - \dot{h}\sin\alpha) + \sigma(\dot{l}\sin\alpha + \dot{h}\cos\alpha) - a\sigma\dot{\alpha} \\
A_5 &= -2R\sigma\dot{\alpha} \\
A_6 &= 2R\sigma\dot{\alpha} \\
A_7 &= 4R(\tau - R)\dot{\alpha} \\
A_8 &= R\sigma\dot{\alpha} \\
A_9 &= -\frac{1}{2}(\tau^2 + \sigma^2 + 2R\tau)\dot{\alpha} \\
A_{10} &= \frac{1}{2}(\tau^2 + \sigma^2 - 4R\tau)\dot{\alpha} \\
A_{11} &= -2R\sigma\dot{\alpha} \qquad \text{(A.28)}
\end{aligned}
$$

Now that the radial velocity component is known, the tangential component can be found by applying the so called 'conjugate function theory' of Cauchy's third theorem. This will provide a relation between the two components, as shown in Equation A.29. A specific derivation of the equation can be found in Appendix A of [46]. Here $\hat{\tau} = \tau + \alpha$ is the thickness parameter offset with the angle of attack. The tangential velocity can be solved for using the Glauert integral, which for the interested reader can be found in Appendix B of the same reference [46]. This results in Equation A.30, where the coefficients are the same as in Equation A.28. Integrating the vorticity distribution, which is equal to the tangential velocity, will result in the unsteady circulation in Equation A.31.

$$
\begin{aligned}
v_\theta(\theta) &= -\frac{1}{2\pi}\oint_0^{2\pi} v_r(\hat{\tau})\cot\left(\frac{\hat{\tau}-\theta}{2}\right)d\hat{\tau} + \frac{\Gamma_0}{2\pi R} \qquad \text{(A.29)} \\
v_\theta(\theta)|_{unsteady} &= \frac{1}{R}\left[-A_1\cos\theta - \left(A_2 + \frac{1}{2}A_7\right)\cos 2\theta \right. \\
&\quad + A_3\sin\theta + \left(A_4 - \frac{1}{2}A_5 + \frac{1}{2}A_6\right)\sin 2\theta \\
&\quad - A_8\sin\theta\cos 2\theta + A_9\sin\theta\sin 2\theta \\
&\quad - A_{10}\cos\theta\cos 2\theta + A_{11}\cos\theta\sin 2\theta \\
&\quad \left. + \frac{\Gamma_0|_{unsteady}}{2\pi}\right] \qquad \text{(A.30)} \\
\Gamma_0|_{unsteady} &= 2\pi\left[2R(\dot{l}\sin\alpha + \dot{h}\cos\alpha) + \dot{\alpha}\left(\frac{1}{2}\tau^2 + \frac{1}{2}\sigma^2 - 2R(R+a)\right)\right] \qquad \text{(A.31)}
\end{aligned}
$$

A.3.3 Total Solution

Now that both the steady solution due to the freestream, and the unsteady solution due to the motion of the airfoil, have been found, their solution is simply found by adding the two components. The final equations are shown in Equation A.32. As an unsteady problem is investigated, it must be reminded that all of the above variables are in fact a function of time. This has been omitted for simplicity, but is included again in the final solution. As mentioned before, the derivative of the transformation can be used to find the airfoil surface velocities.

$$\begin{aligned} v_r(\theta,t) &= v_r(\theta,t)|_{steady} + v_r(\theta,t)|_{unsteady} \\ v_\theta(\theta,t) &= v_\theta(\theta,t)|_{steady} + v_\theta(\theta,t)|_{unsteady} \\ \Gamma_0(t) &= \Gamma_0(t)|_{steady} + \Gamma_0(t)|_{unsteady} \end{aligned} \tag{A.32}$$

A.3.4 Pressure Distribution, Forces, and Moments

The pressure distribution can be obtained using the unsteady Bernoulli equation, which includes an extra term to the steady version which takes into account the change in velocity potential over time, it is shown in Equation A.33. The total surface velocity can be found with the circle radial and circumferential velocity, as in Equation A.34. The last term in the equation is found by transforming the velocity potential to the translating and rotating reference frame and integrating this over the surface using the Leibnitz rule for integration. Its final form is shown in Equation A.35.

$$C_p = 1 - \frac{q^2}{U_\infty^2} - \frac{2}{U_\infty^2}\frac{\partial \phi}{\partial t} \tag{A.33}$$

$$q^2 = \frac{v_r^2 + v_\theta^2}{\left|\frac{d\zeta}{dz}\right|^2} \tag{A.34}$$

$$\frac{\partial \phi}{\partial t}(\theta,t) = -u^2 - v^2 + \frac{\partial}{\partial t}\int_0^{2\pi}\left(u\frac{dx}{d\theta} + v\frac{dy}{d\theta}\right)d\theta \tag{A.35}$$

By integrating the pressure distribution the force and moment coefficients can be obtained. These will consist of two separate parts, the circulatory terms and the apparent-mass terms. The former are induced by the bound circulation on the airfoil, resulting from the freestream. The latter are induced by the fact that the unsteadiness of the airfoil movement also results in unsteadiness of the flow. This leads to a change in momentum of the fluid, resulting in additional forces. An example is flow normal to a flat plate, which without bound circulation and symmetric streamlines around the body, should not produce any forces. However, due to a change in velocity potential in time, the last term in the unsteady Bernoulli equation, there is an 'added-' or 'apparent-mass' force, invoked by the acceleration of the surrounding fluid.

For the steady components, indicated with the subscript 0, the lift can be found according to the Kutta-Joukowski theorem, as shown in Equation A.36. The steady drag component can be found by integrating the pressure distribution, and can be shown for irrotational inviscid flow to be zero. Lastly, the pitching moment can be found using the forces and their working arms, as in Equation A.38.

$$L_0(t) = -\rho \overline{U}_\infty \Gamma_0(t) \tag{A.36}$$

$$D_0(t) = 0 \tag{A.37}$$

$$M_0(t) = \oint_S \rho \overline{U}_\infty \gamma_0(s,t)[y \sin\alpha - x\cos\alpha] ds \tag{A.38}$$

Now, by integrating the change in moment contribution of each vortex over the surface of the airfoil, the second component of the forces and moment can be found. This gives Equation A.39 to Equation A.41, where the subscript 1 indicates the unsteady terms. The moment is computed using the trailing edge coordinates. The total solution can again be found by adding the two components. The respective coefficients are found by non-dimensionalising as usual.

$$L_1(t) = \frac{\rho}{\cos\alpha} \frac{d}{dt} \oint_s \gamma_0 x \, ds \tag{A.39}$$

$$D_1(t) = \frac{\rho}{\cos\alpha} \frac{d}{dt} \oint \gamma_0 y \, ds \tag{A.40}$$

$$M_1(t) = \frac{1}{2}\rho \frac{d}{dt} \oint_S \gamma_0 \left[\left(x^2 - \frac{1}{2}x_{TE}^2 \right) - \left(y^2 - \frac{1}{2}y_{TE}^2 \right) \right] ds \tag{A.41}$$

A.4 Results

The following section will provide the computed results of the above mentioned algorithm. The transformation will be investigated in depth by looking into the effect of the variable parameters. As mentioned before, sadly not all equations perform as expected, and therefore only a steady solution can be computed. As shown in the U2DIVA Panel Code chapter 5, that solution is accurate and will therefore not be repeated here.

A.4.1 Airfoil Geometry

Three parameters control the shape of the airfoil, R_0, τ, and σ. Each of them is varied, keeping the others constant, and the result is shown in Figure A.2.

As can be seen in the first plot, changing the circle radius R_0 has the effect of moving the critical location, the intersection with the abscissa, and therefore increasing the chord. Keeping the thickness parameter τ equals, this also has an impact on the thickness distribution. With a longer chord, the thickness is more evenly distributed, and the airfoil is thinner.

The second plot shows a variation in τ, resulting in a change in thickness of the airfoil. For a value of zero, the airfoil becomes a flat plate. Increasing it makes the airfoil thicker. Lastly, the camber parameters σ changes the maximum camber.

A few things must be noted on this airfoil transformation. The first is that, as can be seen when changing the camber, the airfoil will obtain a geometrical angle of attack. Attention must be paid when computing the results for the forces.

Also, the transformation has some inherent limits. The first is that the trailing edge will always be cusped. There exists another, more general transformation, called the Kármán-Trefftz transform, where a trailing edge angle can be specified. This transform, which can be found in [59], has been investigated through an analysis, and has shown to produce similar results as the Joukowski transformation. Therefore it will not be further explained. Another characteristic is that the maximum thickness location is quite forward, and there is no influence on this. This limits the shapes the airfoil can take.

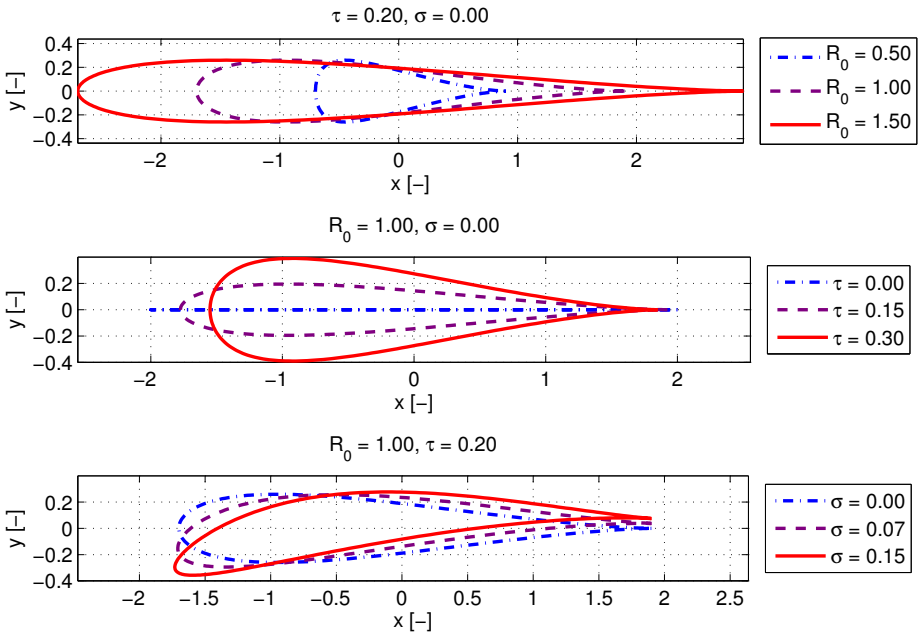

Figure A.2: Variation of the airfoil parameters.